

63-3-5

1

404748

AD No. \_\_\_\_\_  
ASTIA FILE COPY

404 748

ORDNANCE RESEARCH LABORATORY  
The Pennsylvania State University  
University Park, Pennsylvania

NAVY DEPARTMENT BUREAU OF NAVAL WEAPONS (15) CONTRACT NO. 16597

RECEIVED  
MAY 28 1968  
RECEIVED  
JPA D

\$12.50

(4) 812.50

(5) - 671300

(6) REAL FLOW OVER A BODY OF REVOLUTION  
AT ANGLE OF ATTACK,

(10) By E. J. Rodgers.

(14) Technical Memorandum  
File No. TM 5/2420/13

(11) March 28, 1963  
Copy No. 9

(1) NA

(8) NA

(9) NA

(12) 1644p

(13) NA

(15) See cover

(16) NA

(17) NA

(18) NA

(19) NA

(20) U

(21) NA

### ACKNOWLEDGEMENTS

The author wishes to acknowledge, with deepest appreciation, the guidance and helpful comments of his advisor, Dr. G. F. Wislicenus, during the course of this investigation. Thanks are also expressed to other members of his committee for their constructive criticisms: Drs. T. C. Benton, W. Jaunzemis, O. E. Lancaster, and G. U. Oppel.

The investigation was performed at the Garfield Thomas Water Tunnel of the Ordnance Research Laboratory under U. S. Navy Contract NOrd 16597. Appreciation is offered collectively to many members of the laboratory who contributed in many ways; to Dr. J. L. Lumley for many enlightening discussions and comments; to Messrs. H. D. Cannon and J. M. Long for carrying out the bulk of the experimental measurements and calculations; to Mr. M. W. McBride and his tunnel crew for their help in setting up the experimental apparatus; and to others who participated in discussions, calculations, plotting of the data, and reproduction of the manuscript.

## TABLE OF CONTENTS

ACKNOWLEDGEMENTS . . . . .	Page 11
TABLE OF CONTENTS. . . . .	iii
LIST OF FIGURES. . . . .	vi
LIST OF SYMBOLS. . . . .	ix

## Chapter

## I. INTRODUCTION

Origin of Problem . . . . .	1
Statement of Problem. . . . .	3
Scope and Limitations . . . . .	4

## II. HISTORICAL BACKGROUND

Period of Mathematical Interest . . . . .	6
Airship Period. . . . .	6
Missile Period. . . . .	9

## III. METHODS AND PROCEDURES OF THE INVESTIGATION

Theoretical Solutions . . . . .	19
Experimental Approach . . . . .	20
Description of the Model. . . . .	22
Test Conditions . . . . .	26
Pressure Distribution . . . . .	27
Surface Flow Study. . . . .	30
Velocity Direction Measurements . . . . .	32
Velocity Magnitude Measurements . . . . .	39

Chapter	Page
Velocity Components . . . . .	42
Equivalent Tuft Pictures . . . . .	43
Vorticity Distribution . . . . .	47
IV. EXPERIMENTAL RESULTS	
Pressure Distribution . . . . .	51
Surface Flows . . . . .	53
Equivalent Tuft Pictures . . . . .	54
Total Vorticity Distribution . . . . .	57
Circumferential Component of the Vorticity . . . . .	59
Radial Component of the Vorticity . . .	60
Axial Component of the Vorticity . . . .	62
V. ANALYSIS AND DISCUSSION	
Relationships Among the Data . . . . .	65
Generation and Distribution of Vorticity	70
Comparison With Other Studies . . . . .	71
VI. SUMMARY AND CONCLUSIONS	
Origin and Importance of the Problem . .	73
Statement of the Problem . . . . .	73
The Potential Solution . . . . .	74
Procedure of the Investigation . . . . .	74
Results. . . . .	75
Conclusions . . . . .	77
Recommendations for Further Studies . .	81

	Page
REFERENCES . . . . .	83
APPENDIX A: THE POTENTIAL SOLUTION . . . . .	86
APPENDIX B: EXPERIMENTAL ERRORS . . . . .	95
APPENDIX C: DATA REDUCTION. . . . .	107

## LIST OF FIGURES

Figure	Page
1. NACA, Spiral Vortex Sheet-Concentrated Vortices, Model. . . . .	113
2. Maskell's Possible Surface Flows . . . . .	114
3. Main Components of Test Model . . . . .	115
4. Wire Mounting Arrangement . . . . .	116
5. Pressure Tubing Arrangement Along Rear Support Wires . . . . .	117
6. Axial Pressure Distribution Uncorrected for Wind Tunnel Interference, Zero Degrees Angle of Attack . . . . .	118
7. Axial Pressure Distribution Corrected for Wind Tunnel Interference. Zero Degrees Angle of Attack . . . . .	119
8. Sighting Scope . . . . .	120
9. Scope Mounting Brackets and Arrangement on Tunnel. . . . .	121
10. Tuft Probe . . . . .	122
11. Probe Traversing Mechanism . . . . .	123
12. Typical Plots of Velocity Ratio, Downwash Angle, and Sidewash Angle at a Forward Location. . . . .	124
13. Velocity Rake . . . . .	125
14. Typical Plots of the Velocity Components at a Forward Location. . . . .	126
15. Interpretation of the Equivalent Tuft Pictures	127
16. Equivalent Tuft Picture for the Total Flow. 59 Inches From the Nose of the Model. . . . .	128
17. Equivalent Tuft Picture for the Viscous Part of the Flow. 59 Inches From the Nose of the Model . . . . .	129

Figure	Page
18. Vorticity Components . . . . .	130
19a. Pressure Distribution Along the Top Meridian . . . . .	131
19b. Pressure Distribution Along the 15 Degree Meridian . . . . .	132
19c. Pressure Distribution Along the 30 Degree Meridian . . . . .	133
19d. Pressure Distribution Along the 45 Degree Meridian . . . . .	134
19e. Pressure Distribution Along the 60 Degree Meridian . . . . .	135
19f. Pressure Distribution Along the 75 Degree Meridian . . . . .	136
19g. Pressure Distribution Along the 90 Degree Meridian . . . . .	137
19h. Pressure Distribution Along the 105 Degree Meridian . . . . .	138
19i. Pressure Distribution Along the 120 Degree Meridian . . . . .	139
19j. Pressure Distribution Along the 135 Degree Meridian . . . . .	140
19k. Pressure Distribution Along the 150 Degree Meridian . . . . .	141
19l. Pressure Distribution Along the 165 Degree Meridian . . . . .	142
19m. Pressure Distribution Along the Bottom Meridian . . . . .	143
20. Normal Force Distribution . . . . .	144
21a. Surface Flow. Side View. . . . .	145
21b. Surface Flow. Top View . . . . .	146
21c. Surface Flow. Bottom View . . . . .	147



Figure	Page
22. Equivalent Tuft Pictures, for Viscous Part of Flow, at Various Axial Positions. .	148
23. Total Vorticity at Various Axial Positions.	149
24. Circumferential Component of Vorticity at Various Axial Positions . . . . .	150
25. Radial Component of Vorticity at Various Axial Positions . . . . .	151
26. Axial Component of Vorticity at Various Axial Positions . . . . .	152
27. Potential Flow Surface Streamlines . . . .	153
28. Actual Surface Streamlines. . . . .	154
29. Circumferential Pressure Distributions at Various Axial Positions . . . . .	155
30. Minimum Pressure Line and Separation Line .	156
31a. Semi-Elliptic Coordinate System for Potential Flow Calculations . . . . .	157
31b. Rectangular Coordinate System of Tests . .	158
32. Tunnel Static Pressure Gradient. No Model.	159
33. Tunnel Static Pressure Gradient, Model at 0 Degrees . . . . .	160
34. Tunnel Static Pressure Gradient, Model at 6 Degrees . . . . .	161
35. Tuft Calibration Set up . . . . .	162
36. Tuft Calibration Curves . . . . .	163
37. Rake Calibration Curves . . . . .	164

## LIST OF SYMBOLS

$C_n$	normal force coefficient per unit body length
$C_p$	pressure coefficient
$p$	local static pressure
$p_o$	free stream static pressure
$p_i$	static pressure at station i on the wind tunnel wall
$p_T$	total pressure
$q_c$	velocity component in a plane perpendicular to the longitudinal axis of the model due to the viscous part of the flow
$r_{max}$	maximum body radius
$T_c$	projection of the equivalent tuft onto the cross flow plane
$U$	axial component of the free stream velocity
$u$	axial component of the local velocity
$u_p$	potential solution value of the axial component of the local velocity
$V$	cross flow component of the free stream velocity
$V_o$	free stream velocity
$v$	cross flow component of the local velocity
$v_p$	potential solution value of the cross flow component of the local velocity
$w$	lateral component of the local velocity
$w_p$	potential solution value of the cross flow component of the local velocity
$x, y, z$	rectangular coordinate system

x

$\alpha$	angle of attack
$\gamma_x$	axial component of vorticity
$\gamma_y$	cross flow component of vorticity
$\gamma_z$	lateral component of vorticity
$ \zeta $	total non-dimensional vorticity
$\zeta_c$	circumferential component of non-dimensional vorticity
$\zeta_R$	radial component of non-dimensional vorticity
$\zeta_x$	axial component of non-dimensional vorticity
$\zeta_y$	cross flow component of non-dimensional vorticity
$\zeta_z$	lateral component of non-dimensional vorticity
$\zeta, \mu, \omega$	semi-elliptic coordinate system
$\rho$	air density
$\sigma$	downwash angle
$\tau$	sidewash angle
$\phi$	velocity potential

## CHAPTER I

## INTRODUCTION

Origin of Problem

It is well known that the aerodynamic force system due to a body of revolution combined with lifting surfaces differ from the sum of the aerodynamic force system of the isolated components. The difference between the aerodynamic force system acting on the combination and the sum of the aerodynamic forces acting on the isolated components is known as the interference force, or the interference effect.

A large number of investigations have been conducted to determine the interference effects between components such as wings and tails on bodies of revolution,<sup>1,2,3</sup> in the subsonic and supersonic regimes of flight. Most of the investigations were concerned with a wing located on a constant diameter cylindrical portion of a body of revolution in regions where the viscosity effects could be considered negligible<sup>1</sup>.

Recently a number of investigations dealt with the case of a tail on a body of revolution<sup>2,3</sup>. The tails were located on the rear portion of a constant diameter afterbody where the viscous effects are important.

One of the results of the investigations was the indication that the interference of the body on the tail could be calculated quite accurately if the flow field

about the body was known. The calculation consisted of an application of existing finite wing theories to the isolated tail surfaces considered to be operating in the flow field of the body <sup>3</sup>.

Another result of the cited investigations was the behavior of the flow field at various angles of attack of the body. At small to moderate angles of attack of less than 15 degrees, a rather strong pair of concentrated vortices was evident over the body. At larger angles of attack, between 15 and 28 degrees, a steady asymmetric configuration of two or more vortices was observed. For angles of attack greater than this, the pattern of two or more asymmetric vortices became unsteady.

It was also demonstrated that the trajectory of the symmetrical pair of vortices could be calculated if their strength and position is known at some point along the body <sup>4</sup>. The origin of the body vortices and how they emanate from the origin was considered to be a major unsolved problem as late as 1962 <sup>4,5</sup>.

It was concluded in the past studies that the concentrated vortices, trailing downstream and located over the lee side of the body, were fed by a vortex sheet emanating from the body. The origin of the vortices is defined as the most forward location where the trailing vortex pair attaches itself to the body.

Although it has been demonstrated that the interference of the body on the tail can be calculated knowing the flow field of the body, a sizable interference on the body due to the tail can also exist. Tests on the Airship Akron showed that the lift on the body due to the presence of the tail was increased substantially <sup>6</sup>.

Investigations of body-tail interference problems of airships, guided missiles, and torpedo configurations always seem to be limited by the lack of knowledge regarding the real flow over a body of revolution at an angle of attack. The present investigation originated as an investigation of tail-body interference stemming from problems experienced by torpedoes. Attempts at attacking the problem involved the flow over the bare body. It was soon found that a better understanding of the flow over the body was needed in order to proceed further with the interference problem.

#### Statement of Problem

The purpose of this investigation is to determine the difference between the actual flow over a body of revolution and that predicted by potential theory. Since this difference is primarily manifested in terms of vorticity in the flow field about the body, it is desired to determine, (1) how the vorticity is generated along the body, (2) how it is distributed and (3) what are its

most important components. If the axial component of vorticity is the largest component and concentrates into a pair of symmetrical vortices it is also desired to investigate the forward attachment point of the concentrated vortices onto the body.

The results of the investigations will contribute to the understanding of the real flow over a three-dimensional body of revolution. The real flow over a three-dimensional body of revolution is a major unsolved problem in the field of Fluid Mechanics.

#### Scope and Limitations

The approach taken in obtaining a physical understanding of the real flow involves a contrast of an experimental investigation and the potential theory. A mathematical solution of the real flow would involve a solution of the Navier Stokes equation or a simplified mathematical model. The Navier Stokes equation is difficult to solve other than for simple cases. No simplified mathematical model could be thought of, other than those already formulated based on the symmetrical vortex pair.

The experimental investigation is limited to one configuration at one angle of attack at one Reynolds number. The large number of measurements required precluded any variations in these quantities. However, the configuration, the angle of attack, and the Reynolds

number are representative of those of practical significance. The configuration is representative of a practical shape, the angle of attack is representative of the small to medium angles of attack of practical importance, and the large Reynolds number is representative of that experienced by full scale missiles at subsonic speeds.

The limitations on the experimental conditions should not however limit the understanding of the problem greatly. The physical mechanism is no doubt continuous although not necessarily linear. A clarification of the physical mechanism, even at one test condition, will aid in the understanding or prediction as to what will occur at other conditions. Other existing experiments cited, even if they do not go into as great detail as the present one, should also be helpful in extrapolating the results to other conditions.



## CHAPTER II

### HISTORICAL BACKGROUND

Studies regarding the flow over a body of revolution can be divided roughly into three periods, 1) Period of Mathematical Interest 2) the Airship Period and 3) the Missile Period. Only those investigations of prime interest will be covered in this chapter.

#### Period of Mathematical Interest

The flow over a body of revolution was studied, since at least the latter part of the 19th century, by mathematicians as a potential flow problem involving solutions of Laplace's equation. One of the earliest solutions obtained was that for the potential flow over an ellipse of revolution<sup>7,8</sup>.

Since the potential solution does not include viscosity, information of interest to this investigation is not obtained directly. The solutions are valuable, however, since they give good results over the front end of the body where viscous effects are negligible. They can also serve as a model with which to compare the actual flow.

#### Airship Period

In the late twenties and early thirties of this century, investigation of flows over bodies of revolution was stimulated by problems facing the airship designers. Potential theories did not predict the lift of these bodies.

However experiments showed the bodies did contribute a sizeable amount of the aerodynamic lift to the airship at angle of attack. The interference effects between the body and stabilizing surfaces were also found to be quite large <sup>6</sup>.

Much work was done during this period by such investigators as Von Kármán, Munk, and Fuhrmann on potential solutions of bodies of revolution. Also, many experiments were conducted dealing with the aerodynamic forces and moments. None of these, however, revealed how the lift developed on the body.

In 1935 Harrington carried out an investigation on a body of revolution to determine the origin of lift <sup>9</sup>. His investigation dealt with an ellipsoid of revolution having a length to diameter ratio of 6 to 1. Flow surveys were made at various planes (perpendicular to the free stream velocity) in the wake of the model. Pressure distributions on the model and surface flow studies, as well as force measurements, were also made.

The flow-direction and magnitude in the wake of the model was determined at various points in the wake using a National Physics Laboratory null type yawmeter. The yawmeter consisted of four 0.023 inch hypodermic tubes grouped in sets of two in planes 90 degrees apart. Each tube was inclined at 45 degrees to a common axis. A fifth tube, placed behind a hollow cone, was used to determine the

static pressure. The other four tubes projected through the hollow cone. After nulling, the flow angles were read by means of protractors fixed to the yawmeter. The magnitude of the velocity was obtained from calibration curves.

Values of the downwash and sidewash velocities were calculated from the wake measurements and plotted. The downstream component of the local vorticity was calculated from the downwash and sidewash velocities and plotted, at the various wake planes investigated, in terms of iso-vorticity lines.

Two vortex regions, with their maximum values located on the leeward side of the body, were observed from the iso-vorticity plots. In the closest plane to the body investigated (9.6 centimeters aft of the body), the vorticity generated on the ellipsoid had rolled up into what approximated two vortex cores. Data from the other planes indicated that the vortex cores moved down with increasing distance aft of the body.

Harrington's investigation seems to be the first to point out the existence of body vortices. Their existence was based primarily on the wake flow investigations. However, the origin of the vortices on the body and their growth along the body was not revealed. Harrington did attempt to compute the origin of the vortices. He did this by dividing the difference between the moment as given by potential theory and the measured pitching moment, by the

measured lift. This only indicated the lift to be due to the viscous effects on the aft end of the body.

#### Missile Period

Following Harrington's investigation, the problem of the real flow over a body of revolution was not given any significant consideration since the interest in airships had waned. The large lifting wings of airplanes, then in prominence, had reduced the problems associated with the bodies. The unknown body lift was small compared to the large lift of the wings.

The advent of the guided missiles and supersonic airplane incorporating very small aspect ratio wings again brought the body and interference effects into the problem areas. The lift of the body once more became a significant part of the total lift. The interference effects between the body and the small aspect ratio wings or tail surfaces also became significant.

Around 1950 Allen and Perkins presented an approximate method for allowing for the viscous effects on the force and moment characteristics of bodies <sup>10</sup>. The approximate method consisted of the addition of a cross flow drag term to the potential (or slender body) cross force distribution. This was based on the assumption that each circular element along the body would experience a cross force equal to the drag force of a section which is operating at a velocity

given by the cross flow component of the free stream velocity. The approximate method did give good comparison between calculated and measured lift and pitching moments. It did not however give the flow field about the body nor include the body vortices pointed out by Harrington.

The flow separation on bodies of revolution was also discussed by Allen and Perkins. They concluded that since separation can only occur in an adverse pressure gradient, the line of separation will roughly parallel the line of minimum pressures.

They also discussed the existence of body vortices in terms of an analogy between the cross flow at various stations along the body and the development with time of the flow over a cylinder starting from rest. Harrington's flow surveys were cited as well as some supersonic wind tunnel investigations conducted by the National Advisory Committee for Aeronautics (NACA). The body vortices were observed in the supersonic tests by means of Schlieren photographs and the new, but now familiar, "vapor screen" method developed by NACA.

In 1957, Stone and Polhamus summarized the work of NACA on the problem of shed vortices as well as their interaction with stabilizing tail surfaces<sup>3</sup>. The experimental visualizations of the vortices were conducted almost entirely in supersonic flow. A mathematical model consisting of the pair of vortices and their images at

each station along the body in a potential flow was used to calculate the trajectory of the vortex pair by means of a step, or timewise, integration. In order to start the calculation, the strength and position of the vortex at some axial location was required. The starting point of the calculation used was an experimentally measured position near the nose of the model. The vortex strength assumed was  $\Gamma = 4R\alpha V_0$  where  $R$  was the radius of the cylindrical part of the body,  $\alpha$  the angle of attack and  $V_0$  the free stream velocity. The calculated vortex trajectory agreed quite well with that obtained experimentally by means of pressure measurements and vapor screen pictures.

Investigations in the subsonic regime were conducted by Tinling and Allen in 1962<sup>5</sup> in order to extend the information obtained in the supersonic investigations previously conducted by NACA. The results of their investigation paralleled those obtained previously in the supersonic regime. In addition they found, "However, the circulation was found to be distributed over nearly the entire region of the survey rather than concentrated in the region of the vortex core. This result is to be expected since the vortex is in reality the rolled-up vortex sheet resulting from separation of the boundary layer over the body."

During the course of the visual flow studies of NACA it was concluded that the physical flow field for moderate

angles of attack is approximately that shown in Figure 1<sup>4</sup>. Two spiral vortex sheets are produced at the flow separation lines on the sides of the inclined body. The sheets then roll up forming two regions of concentrated vorticity.

Further studies indicated that the feeding vortex sheet was small in strength and could be neglected. The mathematical model then consisted of a trailing vortex pair over the lee side of the body. The attachment point, or "origin," of the trailing vortex pair on the forward part of the body was not known.

Only a few other studies have been conducted regarding the real flow over a body of revolution. One of these was conducted and reported by Mello in 1959<sup>11</sup>. It dealt with the wake vortex characteristics of a cone-cylinder body having a slenderness ratio of about 13, at supersonic speeds.

The purpose of Mello's investigation was also to provide a more basic understanding of the body vortex wake flow and its relation to the problem of wing-body interference. The theoretical model of a vortex sheet and its simplification to a pair of concentrated vortices was also concluded by Mello. As in the case of the work conducted by the other investigators discussed, only the trailing vortex system was investigated. Mello found that the circulation strengths of the concentrated vortices in the vortex wake flow could be estimated provided the

viscous normal force distributions and vortex core locations were known. He also found that the trajectory of the concentrated vortices was sensitive to the assumed location of the vortex at the start of the trajectory calculations but not to the vortex strength assumed.

Spence and Trebble of Great Britain studied the subsonic flow behind a high slenderness ratio body, having a tapered nose and tail portions, at subsonic speeds in 1955<sup>12</sup>. They also observed a concentrated pair of vortices aft of the body at small angles of attack. For their high slenderness ratio body the vortex system became asymmetric above 10 degrees angle of attack. As a result of their investigation they postulated that a spiral vortex sheet formed on the lee side of the body at all small angles of attack giving rise to the concentrated vortex pair aft of the body. Their data did not indicate how this vortex sheet built up on the body.

Because of the complexity of the three-dimensional flow, most of the work conducted had been of an experimental nature with attempts to correlate it to a simplified model of a pair of concentrated vortices. The attempts at correlation pointed out the need for additional knowledge regarding the vortices and their growth along the body.

A theoretical model taking into account the viscous build up, based on potential flow methods, was attempted



by Hill in 1954<sup>13</sup>. Hill replaced the body surface with a vortex sheet whose strength is everywhere proportional to the local velocity. Part of the vortex sheet was then allowed to separate on the lee side of the body and roll up into discrete vortices. The vortex sheet following separation was then adjusted, and the strength of the trailing vortices determined, to satisfy the boundary conditions at the top meridional line. The Helmholtz vortex laws were used in making these adjustments.

Hill applied his method to calculate the lift and moment of a body consisting of a short nose section followed by a constant diameter cylindrical section. Fair comparison with experimental data at a Mach number of 0.26 was obtained.

In the calculations Hill assumed that the vortex separated on the cylindrical part of the body at an angle of 50 degrees from the top center line (the separation point for a two dimensional cylinder). It is not clear whether the same separation location would be applicable in applying his method to a body having a varying, rather than constant, diameter.

Hill stated in his conclusions that experimental studies of the details of the flow patterns would be helpful in improving his "crude" theoretical model and in explaining how much the actual flow deviates from a potential flow.

Other studies of interest in attempting to explain the real flow over a body of revolution are those dealing with surface flows <sup>14,19</sup>. Most of these studies were concerned with laminar flow separation. The present investigation is concerned with turbulent flow.

Of particular interest are the investigations conducted by Eichelbrenner in 1957 <sup>16</sup>. The three-dimensional separation of the laminar boundary layer of an ellipsoid of revolution, having a 6 to 1 slenderness ratio and inclined at an angle of attack of 10 degrees, was calculated. The calculated lines of separation compared favorably with those obtained experimentally by means of a surface flow visualization technique used in a water tunnel. A photograph of the surface flows, as well as a description of the method of computations, can be found in Thwaites' recently published book on incompressible aerodynamics <sup>17</sup>.

In 1954 Eichelbrenner and Oudart defined separation in a manner different than that normally considered for two-dimensional separation <sup>18</sup>. In three-dimensional separation the flow does not necessarily leave the surface of the body but seeks a more favorable pressure gradient while remaining attached to the body. The line of separation is defined as the envelope of the converging wall streamlines seeking a favorable pressure gradient.

In 1955 Maskell presented a generalized concept of separation and deduced the flow conditions in the

neighborhood of the separation line<sup>19</sup>. He credited Eichelbrenner and Oudart's definition of three-dimensional separation with being a step in the understanding of three-dimensional flow problems. However, he felt that their treatment did not clearly define the precise nature of the flow in the neighborhood of the separation line nor the general meaning implied when speaking of separation.

Maskell points out that in two-dimensional flows, separation has been normally associated with the boundary layer leaving the surface of the body, for example, ahead of the trailing edge of an airfoil. He points out that the boundary layer also leaves the trailing edge in many cases. In the general case this is also separation. The difference between these two types of separation is determined by the local conditions at the separation points and the resulting types of exterior flow.

The viewpoint taken by Maskell is that separation is inevitable on a finite body, be it two or three-dimensional. He discussed the two types of separation points in three-dimensional flow, corresponding to the two-dimensional cases. The resulting flow of the viscous regions defined as the region in which viscous effects are important, is shown to be composed of two basic elements. The first of these is a free vortex layer while the second is the bubble.

The free vortex layer is considered to be composed

entirely of main flow fluid containing vorticity and as such adjoins the underlying boundary layer over a surface. The bubble is nothing more than a standing eddie in the flow. Over a body, say with reverse flow, the reversal would be in the form of a standing eddie, or a bubble. Maskell relates each of these to a particular form of the surface flow pattern.

Among the physical structures of possible three-dimensional flows inferred by Maskell in his analysis are those for a body of revolution shown in Figure 2.

This Figure shows various surface flow patterns possible, along with cross sectional views showing the corresponding surfaces of separation. The lines of attachment, according to his analysis, consists of points of attachment of the free stream streamlines. The streamline at each attachment point divides into two surface streamlines. These in turn recombine at a separation point. The separation line is composed of the separation points. The curved surfaces, shown in the cross sectional views, is the surface of separated streamlines leaving the separation line.

Regarding the concept of separation, Taylor also pointed out that separation is usually thought of as a condition to be avoided<sup>20</sup>. He defines separation, essentially in the same way as Maskell, as the condition of a limiting streamline leaving the wall. This then

includes the flow leaving the trailing edge of an airfoil uniformly, as well as the flow leaving at an undesirable location. Taylor suggests the use of the term "stall" rather than "separation" normally used when the separation of the flow occurs at an undesirable location.

## CHAPTER III

### METHODS AND PROCEDURES OF THE INVESTIGATION

#### Theoretical Solutions

As mentioned previously, the real flow over a body is described by the Navier Stokes equation. However it is very difficult to solve this equation even for much simpler geometries than a body of revolution. Difficulties are even experienced in trying to determine boundary layer transition by means of the Navier Stokes equation. It therefore seems that some other approach is necessary at this time.

In the solution of a complex problem, it is often necessary to use a simplified mathematical model which, it is hoped, includes the important physical aspects. In formulating the simplified mathematical model some knowledge of the important physical aspects is required. This knowledge can be based on experimental investigations of the problem or an extrapolation from a field of knowledge developed in related problems.

The mathematical model of a pair of concentrated vortices fed by a weak vortex sheet <sup>4,11</sup> is based on experimental investigation. The mathematical model of Hill, described in chapter II, is based on an extrapolation of related knowledge. These models still leave unanswered many questions related to the flow field and the manifestation of the viscous effects. They do however seem

to best fit the experimental data available at the time of their formulation.

Potential solutions, of course, do not give the viscous effects. They are however quite useful in many problems. In the problem of this investigation the potential flow is contrasted with that of an experimentally obtained real flow. This is quite helpful in revealing the viscous effects.

The potential solution for the body of revolution used in this investigation is discussed in Appendix A of this report.

#### Experimental Approach

All of the information necessary for the understanding of any flow, whether in a channel or over a body, is contained in the details of the velocity field. If there are regions in the flow where the effects of viscosity are small then the resulting flow field does not differ significantly from a potential solution.

Qualitative methods of determining the flow field, such as methods of flow visualization by means of smoke, only supply information in those regions where the viscosity effects start "showing through" the potential flow field. That is to say, the use of qualitative test procedures of determining the flow fields tends to supply information where the viscosity effects have already

become strong and does not furnish the information as to how they build up to this point. An example of this is the visualization of regions of separation by means of smoke or tufts.

This is not meant to imply that such testing is not of importance. Flow visualization techniques certainly are important but they cannot possibly furnish the type of data that shows the build up of viscosity effects in those regions where the viscosity of the medium has not affected the flow to any great extent. Even an eye trained in observing phenomena exposed by flow visualization techniques would have extreme difficulty in distinguishing the viscosity effects in these regions.

If it is desired to obtain a manifestation of the viscosity on the flow about a body of revolution, quantitative data of the flow field would contain the information necessary to expose the viscosity effects in those regions where the effects are still small. Plotting of streamlines calculated from this data would not give different information than that obtained by flow visualization techniques. However, if the potential solution is known, subtracting the potential solution from the measured data should reveal that part of the real flow due to viscous effects quite vividly and show how these effects build up.



Another way of bringing to light the viscosity effects is by calculating the vorticity in the field about the body. Since the vorticity has a direction and a magnitude it is important to determine these quantities. If only one component of the vorticity is determined, say that in the axial direction, then quite a bit of the information is lost. There may be regions where the vorticity vector has only a small component in the axial direction but a larger component in some other direction.

The primary data on which this investigation is based are the velocity field measurements. In order to supplement this data, pressure distributions on the body and visualization techniques to obtain the surface flows were also employed. A discussion of each of these methods and the techniques and apparatus used will be given following a description of the model.

#### Description of the Model

Since it was desired to have a body for which a potential solution was readily available an ellipse of revolution was chosen <sup>7,8</sup>. A length to diameter ratio of 8 to 1 was decided on since this slenderness ratio constitutes a body of practical importance to the Fluid Dynamicist.

In order to simplify obtaining of the test data, the model was made as large as possible consistent with the

wind tunnel in which the tests were conducted. The subsonic wind tunnel at the Garfield Thomas Water Tunnel of the Ordnance Research Laboratory was used for the tests. It has an octagonal test section measuring 48 inches across the flats <sup>21</sup>. A rule of thumb used, based on experience in testing at this facility, states that the model should not be larger than 8 inches in diameter in order to keep the interference effects between the model and the tunnel walls within acceptable limits. (The ratio of the tunnel diameter to the maximum diameter of the model should not be less than 6 to 1). The maximum allowable diameter of 8 inches, with the slenderness ratio of 8 to 1 that was chosen, thus gave a length of 64 inches.

The model was constructed from mahogany. It was made in two main parts, as shown in Figure 3, plus a removable rear fairing. It was planned to have another afterbody which would incorporate tail surfaces. This additional afterbody will be used to continue the study beyond that of the bare body.

Provisions were made for obtaining the pressure distributions on the model to supplement the flow field measurements. The removable rear fairing allows access to the pressure taps on the model. The static pressure taps were located on a meridional line of the body. The body was rotated to obtain circumferential pressure distributions.

The reason for constructing the main body in two sections was based on the planned tests incorporating tail surfaces. In the tail tests it is desired to hold the tail surfaces in a fixed position while rotating the forward part of the model to obtain the circumferential pressure distributions. Additional circumferential pressure taps were included on the afterbody having the tail surfaces.

The forward part of the body, Figure 3, extended from the nose of the model to about 54 inches. This was followed by a section extending to about 62.4 inches. The rear fairing completed the 64 inch length.

The rear fairing was spun from copper and split for easy removal. It was held in place by means of magnets.

The two main parts of the model were held together by metal plates between them. These plates were spring loaded so as to have them bear together while still allowing one section of the model to be rotated independently of the other. A cylindrical tie rod extended rearward from the plate fixed on the forward section of the model.

The wooden parts of the model were made in two half sections. The sections were then bolted and doweled together and turned on a lathe to the required dimensions. The two parts were then separated and one half of each of the sections were rabbetted. Slots were cut with a modeling knife perpendicular to the meridional line at

eighteen longitudinal positions along the body. The slots extended from the outer surface of the model to the rabbeted portion. Stainless steel hypodermic tubes were placed in the slots and glued and stapled in place. Plastic tubing was glued to each of the hypodermic tubes and led toward the rear of the model in the rabbetted portion. The two sections were again bolted and glued together and sanded to a proper finish. Several coats of varnish were applied to give a smooth protective finish. The plastic tubing extending from the aft end of the model was connected to a manifold located in the rear portion of the model. The manifold consisted of 40 sections of hypodermic tubing inserted through a steel plate.

In order to reduce the interference of the mounting system necessary for positioning the model within the wind tunnel, a wire mounting arrangement shown in Figure 4 was used. It was felt that this arrangement would offer less disturbance to the flow than a strut or sting mounting.

Piano wire was connected to fittings at the front and rear of the model. The fittings were constructed in a manner that would allow rotation of the model. The other ends of the wires extended through the tunnel walls and were connected to brackets through a turnbuckle.

Angle of attack settings were obtained by using different length wires to position the rear and front portions at a measured distance from the floor of the

tunnel. The center of the model was always kept at the centerline of the tunnel. Both the front and rear of the model were spaced an equal distance from each of the side walls of the tunnel so that no angle of yaw would be present.

#### Test Conditions

All of the tests were conducted at a tunnel velocity of about 100 feet per second. This gave a Reynolds number of about  $2.8 \times 10^6$  based on the model length.

Investigations made using a hot wire probe near the surface of the model indicated that the boundary layer was turbulent over almost the entire length of the body. The probe was placed very close to the surface and moved along the body length. It was concluded from the evidence present during the survey that the forward fitting acted as a tripping device.

Since a large number of measurements were to be taken, only three angles of attack in the low angle of attack region were to be investigated. The angles of attack chosen were 0, 6, and 12 degrees. However once the investigation was started, the time required to obtain the data for the 0 and 6 degrees case precluded any tests at 12 degrees. Since the 6 degree angle of attack condition is the important one for the body producing lift, it is the only one of the two angles of attack for

revolution, of the slenderness ratio used, shows small perturbations to the free stream velocity. For this reason, it was decided from the onset of the investigation to pay very close attention to the interference effects due to the tunnel walls and to the measuring apparatus. The first part of the investigation was therefore the determination of the pressure distributions on the body. On the forward part of the body, where viscous effects are unimportant, very good agreement between the measured pressure distribution and that obtained from the potential solution should be present <sup>10</sup>. Thus the data on the forward part of the body could be used to evaluate the interference effects present.

An investigation was carried out to determine the maximum number of plastic tubes, leading from the aft part of the model to a manometer board exterior to the tunnel, that could be used while keeping their effects on the model small. Tests were conducted varying the number of tubes and checking the effect on the pressure at a number of taps on the afterbody. It was found that a maximum of nine plastic tubes could be used. A noticeable change in the pressure distribution could be measured on the after-

body pressure taps when more tubes were used.

The nine plastic tubes were brought out of the tunnel in sets of three along each rear support wire, Figure 5. They were connected to nine of the manifold outlets at a time until the eighteen pressure taps on the body were included in the tests.

The nine plastic tubes were connected to a Meriam Instrument Company, Type W, 60 inch, 11 tube manometer bank inclined 10 degrees from the horizontal. The manometer bank had been calibrated previously and indicated some slight errors for the various tubes Appendix B. The errors, even though small, were taken into account in the reduction of the data.

A pitot static tube, located a short distance from the start of the tunnel test section, was used to measure the free stream dynamic pressure as well as the free stream static pressure. The pressure taps of the pitot static tube were also connected to the inclined manometer bank.

The pressure coefficient is defined as:

$$C_p = \frac{p - p_o}{\frac{1}{2} \rho V_o^2} = 1 - \left( \frac{V}{V_o} \right)^2 \quad (1)$$

where:  $p$  = the local static pressure  
 $p_o$  = the free stream static pressure  
 $V$  = the local velocity  
 $V_o$  = the free stream velocity  
 $\rho$  = the density of the air

The pressure difference between a pressure tap on the model and the static pressure in the free stream was read in inches of displacement of the ethyl alcohol between the two corresponding tubes of the manometer board corrected by the manometer board error.

The dynamic pressure  $1/2 \rho V_o^2$  was obtained as the difference in inches of ethyl alcohol between the static and dynamic tubes of the free stream pitot static tube corrected for the manometer board error.

The pressure coefficient was obtained by dividing the corrected static pressure displacement by the corrected dynamic pressure displacement.

An example of the data reduction and the corrections applied is given in Appendix C.

A plot of the pressure distribution along the longitudinal axis of the body, at an angle of attack of 0 degrees, showed quite a sizeable difference between the measured pressure coefficients and that given by potential flow, Figure 6. From this plot it was clear that there was quite a sizeable wind tunnel interference effect. Although the interference effect was small in magnitude it was large compared to the small values of the theoretical and measured pressure coefficients.

The reason for this interference was investigated since it was deemed necessary to have the measurements as accurate as possible in all of the tests because of the



low perturbation of this body to the free stream. It was found that the pressure coefficient error could be related to a pressure gradient that existed in the tunnel. The pressure gradient was due to the boundary layer growth along the walls as well as to the decrease in area at various cross sections because of the presence of the model, Appendix B. Although the pressures were affected it was reasoned that the flow direction would not be affected to any extent.

The wall static pressure gradient was measured along the tunnel. Corrections for the measured pressure gradient brought the test data into agreement with the theoretical pressure coefficients on the forward part of the body where good agreement is to be expected, Figure 7. The arguments leading to this method of correcting for the pressure coefficients as well as to the conclusion that the flow directions are not affected to any extent are presented in Appendix B.

#### Surface Flow Study

A surface flow visualization technique was employed to obtain the limiting streamline and the separation lines on the body <sup>22</sup>. This technique consists of painting the model with titanium oxide in a base of kerosene. A few drops of oleic acid is added to the mixture to obtain a better dispersal of the titanium oxide. The quantities of each of the materials was determined by trial and error in order

to obtain the proper proportions. This trial and error process seems to be required until a certain skill is obtained in knowing when the proper mixture has been achieved <sup>22</sup>. Tests using the same mixture, which had been recorded, were attempted a few months later. The results were not satisfactory. It did not require as many trials the second time in order to obtain a good paint.

The paint mixture was spread evenly in a thin layer on the entire surface of the model with a three inch paint brush. Spraying the paint on did not give good test results.

The tunnel was then run at about 100 ft. per. second. It was found that at slower speeds gravity caused the paint streaks to be displaced downward appreciably while at higher speeds the resulting flow lines were not as distinct. The tunnel was allowed to run long enough for the excess mixture to flow off of the model as well as to allow partial drying. This took about 45 minutes. If the tunnel flow was stopped soon after the pattern was formed, the excess fluid collected at the extreme rear portion of the model, flowed forward to a lower position, and ruined the traces on the bottom of the model.

After the tunnel flow was stopped photographs of the top, side, and bottom of the model were taken. These photographs were obtained from the outside of the tunnel looking from the aft end of the model slightly forward.

The model was rotated to obtain the different views. Attempts at taking the model out of the tunnel for photographs were abandoned since it was difficult not to smear the patterns even with the most careful handling procedures.

The tunnel window supports prevented a single photograph to be taken from the side of the model perpendicular to the body axis. Attempts were made in photographing the model through three of the tunnel windows and matching the photographs. Even though extreme care was taken in locating the cameras and in enlarging the prints, it was impossible to make a composite picture due to the parallax of the camera

#### Velocity Direction Measurements

A number of methods for measuring the velocity field about the body can be used <sup>23</sup>. These include the use of an x arrangement of hot wires, yaw probes, and vanes.

A very simple method employing tufts of yarn was used successfully by Smith in investigating secondary flows in turbine cascades <sup>24</sup>. Because of the simplicity and accuracy of the method of this investigation, it was decided to adapt it to the flow measurements of this investigation. The directions of the tuft in the flow were obtained with a simple sighting scope consisting of a brass tube mounted on a bracket which allowed rotation of the tube. A single cross hair was placed across the

diameter of the far end of the tube. The cross hair was aligned with the tuft and the angle from a reference direction was read from a protractor mounted on the bracket. The scope could also be pitched and another protractor was used to measure the angle of pitch.

Smith's scope was modified for the present investigation by placing an eyepiece, consisting of a cup with a small hole drilled in the center, onto the sighting scope and by adding rods perpendicular to the axis of the scope. It was found that the eyepiece made it easier to align the cross hair with the tuft and the rods aided in the rotation of the scope when aligning the cross hair and tuft. Figure 8 shows the modified scope that was used.

It was found that an individual using this scope could measure a given direction to within  $\pm 1$  degree without any difficulty. Lengths of yarn were mounted at various known angles on one of the windows of the test section of the wind tunnel. The scope was mounted on an opposing window, sighting through the test section at the yarn. Various individuals then read the known angles. Except for very few scattered instances, the measurements were confined to a spread of  $\pm 1$  degree from the actual angles. With a little practice it was not difficult to reduce this spread to  $\pm 1/2$  degrees. Smith reported the accuracy at  $\pm 1$  degree.

Two scopes were used for the present investigation.

One of these was mounted at the side window of the tunnel for measuring the downwash angle,  $\sigma$ . Plastic windows were placed in the bottom and top walls of the wind tunnel for the test. The other scope was mounted on the top, or bottom, window for measurements of the sidewash angles,  $\tau$ . The scope was used at the bottom windows for those regions below the body not visible from the top. Both scopes were mounted on brackets as shown in Figure 9. They were positioned to look directly at the tuft thus directly measuring the downwash and sidewash angles. The top (or bottom scope) was tilted at the same angle as the body angle of attack so as to measure the sidewash angle directly.

Figure 31b shows the downwash angle,  $\sigma$ , and the sidewash angle,  $\tau$ , as defined for the investigation. The downwash angle at a point is defined as the angle between the longitudinal axis, and the projection of the local velocity at the point onto a vertical plane containing the longitudinal axis of the body (the x-y plane). The sidewash angle at a point is defined as the angle between the longitudinal axis and the projection of the local velocity at the point onto a plane at the same angle of attack from the horizontal as the body and containing the longitudinal axis (the x-z plane).

The tuft used was a piece of three strand wool baby yarn. It was mounted to a probe consisting of 0.028 inch

diameter steel wire mounted in a tapered brass rod, as indicated in figure 10, so as to allow free rotation of the tuft about its mounting point.

A mounting loop of 0.017 inch wire was soldered near the tip of the wire portion of the probe. Another loop of 0.011 inch wire was passed through the mounting loop and cemented to the sides of the tuft with a drop of fly tying cement. Extreme care was exercised in trying to position the ends of the loop of wire so as to be diametrically opposed on the tuft and aligned with the tuft axis.

It was found that the tuft-probe arrangement was subject to two important errors. The first of these was the weight of the tuft and the second was a tip effect of the wire portion of the probe. Investigations prior to actual measurements over the body were made with the probe mounted in the center of the empty tunnel. The tunnel velocity was set at about 100 ft. per. second. A tuft of about 1 1/2 inches in length indicated quite a sizeable downward angle from the horizontal. The tuft was then cut to a smaller length and the angle measured again. The error between the horizontal direction of the tunnel flow and the tuft direction decreased showing the presence of the effect of the weight of the tuft.

As the tuft length was decreased it was found that the tuft assumed an upward inclination. Flow surveys of the tests section, conducted by another investigator using

hot wire methods, had indicated very little flow angularity. Another effect than the weight thus seemed to be acting.

A 3/4 inch tuft was then mounted to a wire stretched vertically across the test section of the tunnel, in the same manner as used on the probe. Measurements showed this arrangement brought the tuft direction and flow direction into agreement. This indicated that the flow about the tip of the needle affected the tuft direction.

In order to confirm this hypothesis of the probe tip effect, the probe-tuft arrangement was mounted in a jet of a hot wire calibration tunnel mentioned in Appendix B. The tuft assumed an upward inclination with respect to the axis of the jet. A wire of the same diameter as the needle was brought into contact with the tip of the probe, aligned with the axis of the tip portion. As the wire approached the needle the tuft moved downward until it assumed the same direction as the jet flow.

Since the weight and tip effects were important, the tufts used in the tests were calibrated in the manner described in Appendix B. It is obvious that the weight effect would be most important at lower velocities, therefore most important in the regions near the body where the viscous effects are present. The calibration was therefore made at various velocities. It was found that the calibration was affected by slight differences in the mounting of new tufts, as they had to be replaced.

Therefore, each time a new tuft was made it was calibrated prior to making flow measurements over the body. The calibration of each of the first few tufts used was repeated after a period of use. It was found to hold true to the initial calibration. Subsequently, each new tuft was only calibrated prior to being used in the tests.

In order to position the tuft at various points in the field around the body, the tuft probe was mounted in the simple traversing device shown in Figure 11.

The probe was mounted in a probe holder attached to a platform. The platform was made in two parts so that it could be extended in a horizontal direction perpendicular to the tunnel axis. The adjustment had to be made from inside the tunnel while the tunnel was not operating. The platform in turn was mounted to a vertical plate arrangement for movements in a vertical direction. It could be moved up and down from outside the tunnel, while the tunnel was operating, by means of a cable attached through bevel gears rotating a lead screw.

Movements in the longitudinal direction were accomplished, with the tunnel shut down, by sliding the vertical plate along top and bottom rails placed along two of the octagonal walls of the tunnel.

The vertical plate-rail attachment was constructed in a manner allowing the vertical plate and platform to be tilted so that the up and down motions of the platform



could be made perpendicular to the axis of the body at an angle of attack.

The body was mounted in the tunnel using the same wire suspension system used in the pressure measurements. Tests were conducted at a tunnel velocity of about 100 ft. per. second.

The probe positioning mechanism was set along the rails at given stations along the body axis. Eleven stations were covered during the investigation. These were located at distances of 8, 16, 32, 40, 48, 56, 57.5, 59, 60.5, 62, and 64 inches from the nose of the model. The platform was positioned so the tuft would be located at the centerline of the model, at each of the planes. The probe was then traversed vertically.

Measurements of the sidewash and downwash angles were made at various increments in the vertical distance from the body. If the measured angles did not appear to change significantly, the increments used were 1/2 of an inch. If it appeared that there was a strong gradient in the direction of the velocity, then smaller increments were used.

The platform was then moved at 1/2 inch increments away from the center line of the body and the probe traversed vertically at each of these lateral locations.

The top scope was moved to the bottom window when covering the regions below the model.

Because of the size limitations of the top, bottom, and side windows, as well as the limitations in the travel of the traversing mechanism, the field that could be mapped at each location was restricted to 4 inches on each side of the centerline of the model in the lateral direction and a total of 12 inches in the vertical direction.

A typical plot of the downwash and sidewash angles, measured at a distance of 8 inches from the nose, is shown in Figure 12. The downwash and sidewash angles as calculated from potential flow are also shown.

One expects the potential flow to give good results at this location on the forward part of the body. However, the Figure shows an error in the measured downwash angles. When the calibration data is applied to the measured data (once the velocities at the points are also known), the potential flow and corrected measured data agree quite well.

#### Velocity Magnitude Measurements

The magnitude of the velocity in the field about the body was obtained by means of the three prong rake shown in Figure 13.

The rake consisted of two total head tubes and a static tube mounted in a tapered brass rod similar to that of the tuft probe. The three tubes, made of 0.049 inch diameter hypodermic tubing, were arranged so that they

would all lie in a vertical plane with one total head tube 0.35 inches above and the other 0.35 inches below the static head tube. The four holes of the static tube lay in the same line as the opening of the total head tubes. These holes were drilled in the hypodermic tube with a number 79 drill.

Two total head tubes were used since it was desired to have the total head tube approach the body as closely as possible. The top tube was intended for measurements of the total pressure in the regions below the body while the bottom one was intended for measurements in the regions above the body. Since both of the total head tubes were always connected to the manometer, the pressures of both of the tubes were recorded during the tests.

The rake probe was mounted in the traversing mechanism. Nylon tubing was attached to the three tubes coming out of the base of the probe and brought out of the tunnel along the platform of the traversing mechanism, the rails, then through the tunnel wall. The three tubes were connected to the same inclined manometer board used in the pressure measurement tests. The pitot static tube located in the forward part of the test section, used to measure the tunnel velocity, was also connected to the manometer board.

Measurements of the rake pressures were obtained in the same regions about the body as in the tuft direction

measurements. The total head and static readings of the free-stream pitot static tube were also recorded each time a rake reading was taken.

The rake measurements were taken with the three tubes of the rake lying in a vertical plane. Their axes were parallel to the tunnel axis. The local flow at each of the tubes could therefore be at an angle to the axis of that tube. This local flow angle could cause an error in the pressure reading. For this reason, each of the tubes of the rake was calibrated in a jet of known velocity with the rake oriented at various pitch and yaw angles as discussed in Appendix B.

The magnitude of the ratio of the local to free-stream velocity,  $V/V_0$ , was obtained from the measured pressure readings in the manner discussed in Appendix C. The application of the calibration data to the measured data is also discussed in the appendix.

A typical plot of the velocity ratio, at various points in the field about the body, is also shown in Figure 12 at a station 8 inches aft of the nose of the model. The application of the calibration data brings the measured data into agreement with the potential flow results at this forward station where good agreement is expected.

### Velocity Components

With the velocity known in magnitude (in terms of the ratio of the local velocity to the free stream velocity) and in direction (in terms of the downwash and sidewash angles) the components of the velocity in any desired direction could be determined. For purpose of convenience, the velocity components calculated were those in the directions of the axis system used in obtaining the wind tunnel data; namely, the x, y, z system of Figure 31b. The corresponding velocity components in this axes system are designated as u, v, and w.

The nondimensional ratios of the local velocity component to the free stream velocity are obtained from the magnitude and direction measurements by the following relationships:

$$\begin{aligned}\frac{u}{V_0} &= \frac{V/V_0}{\left[1 + \tan^2 \sigma + \tan^2 \tau\right]^{1/2}} \\ \frac{v}{V_0} &= \frac{V/V_0 \tan \sigma}{\left[1 + \tan^2 \sigma + \tan^2 \tau\right]^{1/2}} = \frac{u}{V_0} \tan \sigma \\ \frac{w}{V_0} &= \frac{V/V_0 \tan \tau}{\left[1 + \tan^2 \sigma + \tan^2 \tau\right]^{1/2}} = \frac{u}{V_0} \tan \tau\end{aligned}\quad (2)$$

The calculations were carried out on an IBM 1620 computer using the values of the magnitude of the velocity ratios and the angles, corrected for the known errors in

the measured data.

A typical plot of the components of the velocity ratios is shown in Figure 14, at a forward location where the potential flow is expected to give good results. The plot shows that when the known experimental measurement errors are taken into account, good agreement is achieved. The errors were found to influence the shape of the curves at the more aft locations and thus would also affect the calculation of the vorticity, discussed in a later section of this report.

#### Equivalent Tuft Pictures

A technique used to visualize flows in the cross flow planes, along or behind an object in a flow, is the use of a tuft grid<sup>24</sup>. The tuft grid consists of a network of uniformly spaced vertical and horizontal wires with a tuft attached at each intersection. The assembly is located in a plane at which it is desired to obtain a visualization of the cross flow. Normally a photograph of the resulting tuft pattern formed is obtained from a downstream direction while the tunnel is operating.

A tuft grid was constructed and placed behind the model at various positions. Since the perturbations to the flow are rather small for the angle of attack of 6 degrees, the results were not satisfactory and are not reported herein.

In order to obtain a visual picture of the cross flow over the body an equivalent tuft picture was plotted from the test data. This equivalent tuft picture is a plot of the ratio of the cross flow component of the velocity at a point divided by the total velocity at the point, plotted for various discrete points about the body. The discrete points chosen were a rectangular network spaced a half inch vertically and horizontally from the longitudinal axis at various axial stations.

The equivalent tuft picture is interpreted by Figure 15, along with the following discussion.

The ratio of the local velocity to the free stream velocity, in terms of the velocity components of equation (2), is:

$$\frac{V}{V_o} = \left[ \left( \frac{u}{V_o} \right)^2 + \left( \frac{v}{V_o} \right)^2 + \left( \frac{w}{V_o} \right)^2 \right]^{1/2} \quad (3)$$

The ratio of the cross flow component of the local velocity to the free stream velocity is:

$$\frac{V_c}{V_o} = \left[ \left( \frac{v}{V_o} \right)^2 + \left( \frac{w}{V_o} \right)^2 \right]^{1/2} \quad (4)$$

Thus the magnitude of the ratio of the cross flow component of the local velocity to the total local velocity, or the projection of the equivalent constant length tuft

on the cross flow plane, is obtained as:

$$T_c = \frac{V_c/V_o}{V/V_o} = \frac{V_c}{V} \quad (5)$$

and its direction, measured from the z axis as:

$$\psi = \arctan \frac{v/V_o}{w/V_o} \quad (6)$$

In the regions about the body where the magnitude of the local velocity does not differ significantly from the magnitude of the free stream velocity,

$$T_c = \frac{V_c}{V} \simeq \frac{V_c}{V_o} \quad (7)$$

and the tuft picture is the same as a plot of the projection of the local velocity to free stream velocity onto a plane normal to the body longitudinal axis. However, in regions where there is a significant difference between the magnitudes of the total local and free stream velocities, a plot of  $V_c/V_o$  would have the same direction as the equivalent projected tuft but a different magnitude.

A cross flow equivalent tuft picture at a station located 59 inches from the nose of the model is shown in Figure 16. A tuft having a length of 2 inches was assumed. Also shown on this plot is the projection of the local velocity vector divided by the free stream velocity onto the plane,  $V_c/V_o$ , by means of the short lines inter-



secting the vectors. The tuft length in this case is  $V/V_0$ . For  $V_0$  greater than  $V$ , the tuft length would be less than 2 inches.

At this location, the body is decreasing in diameter and the components of the flow due to the changing diameter are quite evident. The potential part of the flow is predominant and tends to hide the information regarding the viscous effects that is being sought. This is especially true in the regions away from the body where the viscous effects are small.

If the potential solution is subtracted from the measured flow field, then the remaining flow is that primarily due to the effect of viscosity. For the equivalent tuft pictures, let:

$$\frac{q_c}{V_0} = \left[ \left( \frac{v}{V_0} - \frac{v_p}{V_0} \right)^2 + \left( \frac{w}{V_0} - \frac{w_p}{V_0} \right)^2 \right]^{1/2} \quad (8)$$

where the subscript  $p$  indicates the potential solution value.

Then:

$$T_c = \frac{q_c/V_0}{V/V_0} = \frac{q_c}{V} \quad (9)$$

is the ratio of the magnitude of the cross flow velocity due to the viscous effects divided by the magnitude of the total local velocity. In the same way:

$$\begin{aligned}\psi &= \arctan \frac{v/v_o - v_p/v_o}{w/v_o - w_p/v_o} \\ &= \arctan \frac{v - v_p}{w - w_p}\end{aligned}\quad (10)$$

The potential velocity components are derived in Appendix A.

A plot of the equivalent tuft picture for the viscous part of the cross flow is shown in Figure 17 at the same location as that of Figure 16. A total tuft length of 2 inches is also assumed for this plot. It can be seen that the viscous part of the flow has been more clearly exposed.

The short lines intersecting the vectors are now the magnitudes of  $q_c/v_o$ .

#### Vorticity Distribution

The components of the vorticity were also calculated from the measured velocity field data corrected for the known experimental errors. For the sake of convenience, the vorticity was initially calculated in the x, y, z directions of Figure 31b.

The components of the vorticity at a point in the x, y, z directions are written for the left handed coordinate system used as:

$$\begin{aligned}
 \gamma_x &= - \frac{\partial w}{\partial y} + \frac{\partial v}{\partial z} \\
 \gamma_y &= \frac{\partial u}{\partial z} + \frac{\partial w}{\partial x} \\
 \gamma_z &= - \frac{\partial v}{\partial x} - \frac{\partial u}{\partial y}
 \end{aligned}
 \tag{11}$$

Dividing by  $V_o$  and multiplying by the maximum radius of the body would give a nondimensional vorticity component. Equation (5) can then be written in terms of non-dimensional vorticity components as:

$$\begin{aligned}
 \zeta_x &= - \frac{\partial w/V_o}{\partial y/r_{\max}} + \frac{\partial v/V_o}{\partial z/r_{\max}} \\
 \zeta_y &= \frac{\partial u/V_o}{\partial z/r_{\max}} + \frac{\partial w/V_o}{\partial x/r_{\max}} \\
 \zeta_z &= - \frac{\partial v/V_o}{\partial x/r_{\max}} - \frac{\partial u/V_o}{\partial y/r_{\max}}
 \end{aligned}
 \tag{12}$$

Plots of the variation of  $v/V_o$  and  $w/V_o$  were made as a function of  $x/r_{\max}$  for fixed values of  $y/r_{\max}$  and  $z/r_{\max}$ . These indicated that the quantities

$$\frac{\partial v/V_o}{\partial x/r_{\max}}$$

and:

$$\frac{\partial w/V_o}{\partial x/r_{\max}}$$

could be neglected at all of the stations investigated except the last one at 64 inches from the nose, the extreme aft end of the body. The slopes of the variations were measured from the curves and used in the calculations at the extreme aft station. At all other stations these quantities were not included in the calculation since they were extremely small.

It was felt that for the present investigation, involved with the determination of a better physical understanding of the flow, it would be more helpful to have the vorticity components in a radial and circumferential direction than in the lateral and cross flow directions. This was easily accomplished by resolving the y and z components of vorticity into the radial and circumferential directions, Figure 18. Assuming the positive directions of the radial and circumferential vorticity components in the outward and counterclockwise direction, as viewed from the downstream direction respectively, then:

$$\begin{aligned}\zeta_r &= \zeta_z \sin \omega + \zeta_y \cos \omega \\ \zeta_c &= \zeta_y \sin \omega - \zeta_z \cos \omega\end{aligned}\tag{13}$$

where:

$$\omega = \arctan \frac{z/r_{\max}}{y/r_{\max}}$$

The total non-dimensional vorticity at a point is given by:

$$|\zeta| = \left[ \zeta_x^2 + \zeta_r^2 + \zeta_c^2 \right]^{1/2} \quad (14)$$

The calculations were performed on an IBM 1620 computer using the slope midpoint between two measured points as that given by a straight line joining the two points. This method was checked against the slopes actually measured from plots of the velocity components and gave acceptable results.

## CHAPTER IV

### EXPERIMENTAL RESULTS

#### Pressure Distribution

Plots of the pressure coefficient on the body, corrected for wind tunnel interference effects as previously discussed, are shown in Figure 19 as a function of the axial position at a constant angular position. Also shown is the pressure coefficient distribution as predicted by potential theory, Appendix A.

Neglecting the second point from the nose of the model, which always gave too high a pressure coefficient, one sees that the potential theory predicts the pressure distribution over most of the body quite well. It is only at the tail end of the model that the experimental pressure coefficients show a significant difference from that given by potential theory.

One also sees from the plots that at the tail end of the body, the actual pressure coefficients do not differ significantly from the potential flow up to angles of 30 degrees measured from the top meridional line of the body. At angular positions from 45 to 180 degrees, the latter being the bottom meridian, the pressure coefficients on the aft end of the body show a definite increase from that predicted by potential theory.

It is also of interest to note the pressure coefficients on the front end of the body. Although the difference between the measured and potential pressure

coefficients are not as great as on the aft end of the body, it does appear that the actual pressure coefficients are somewhat lower on the top part of the body than predicted by potential theory. At angular positions greater than 60 degrees from the top meridian, the agreement between the actual and potential coefficients becomes very good.

Figure 20 shows the normal force coefficient distribution,  $C_n$ , along the body. The points shown were obtained by integrating the pressure component in the cross flow direction along the circumference of the cross sections at each axial station where test data was obtained. If  $a$  is the radius at a particular station and  $\omega$  the angular position from the top of the body then:

$$C_n = -2 \int_0^\pi C_p \cos \omega \, d\omega \quad (15)$$

The normal force coefficient distribution agrees quite well with that given by potential theory except on the aft end of the body. The viscous effects thus give a resultant normal force in the actual flow whereas the potential theory only predicts a moment for the case of a body at an angle of attack. Partly for this reason, it has been customary to say that the lift develops on the aft end of the body.

As a matter of comparison, the normal force dis-

tribution as predicted by Munk's Airship Theory <sup>10</sup> is also plotted.

#### Surface Flows

Surface flow patterns, for the body at an angle of attack of 6 degrees, are shown in Figure 21. The wall streamlines are easily seen. The separation line, as defined by Maskell, is also seen fairly well except near the nose of the model. At the nose, the separation line becomes rather indistinct since the wall streamlines approach each other very gradually. They still form the characteristic cusp at the separation line, at the forward locations. Unfortunately, the flow pattern at the extreme aft end, over the removable fairing, is distorted. Information on the rearward termination point of the separation line is thus not available.

In the handling of the model between runs, and in developing the proper paint mixture, a number of finger prints became imbedded in the model finish near the front end of the model. Attempts made at washing them off were unsuccessful. A piece of cloth dampened in kerosene was used to wipe the model between applications of paint. This may have caused the kerosene and paint mixture to become imbedded in the model surface. It is believed that wiping the model with a detergent soaked cloth, rather than the kerosene soaked cloth, may have prevented the fingerprints



from becoming fixed in the model surface.

#### Equivalent Tuft Pictures

The equivalent tuft pictures, or that part of the cross flow differing from the potential solution divided by the magnitude of the total local velocity is shown in Figure 22 at the various indicated longitudinal locations along the body. As stated previously, the potential solution has been subtracted from the measured cross flow field so that the equivalent tuft pictures only show the viscous contribution of the flow.

The center station of the body, along with four other stations about the center station, is shown in the top row. The bottom row shows the stations at closer spacings on the tail of the model.

A constant "tuft" length of 2 inches was assumed at all of the points of the grid. The grid network is spaced at  $1/2$  of an inch both vertically and horizontally, as measured from the origin of the cross section; namely, the longitudinal axis. The origin of a tuft is located at a grid intersection. Half inch spacings are indicated on the ordinate and abscissa. The length of the tuft drawn, is the projection of the 2 inch tuft onto the plane. The trace of the body is shown at each longitudinal location by a semi-circle.

The short lines cutting the vectors have been drawn

at the locations where the ratio of the magnitudes of the total local to free stream velocities differ significantly from unity. The length of the vector to the line is the ratio  $q_c/V_o$  whereas the vector to the arrow head is  $q_c/V$ . Thus there are four pieces of information contained in the plots. These are,

- (1) the direction of the viscous part of the cross flow,
- (2) the ratio of the viscous part of the cross flow to the total local velocity,  $q_c/V$ , indicated by the arrow head,
- (3) the ratio of the viscous part of the cross flow to the free stream velocity  $q_c/V_o$ , indicated by the short line, and
- (4) the ratio of the total local velocity to the free stream velocity obtained by dividing  $q_c/V_o$  by  $q_c/V$ .

As an example, consider the point located 1 inch to the right of and 1/2 inch below the origin, in the plane 64 inches from the nose of the model. The direction of the viscous part of the cross flow is at an angle of about 145 degrees from the zenith. Taking into account the reduction of the figure, the ratio  $q_c/V$  is measured as about 0.90 inches while  $q_c/V_o$  is measured as about 0.41 inches. Since the unit vector assumed was 2 inches, the ratios of the velocities are then one half of the

measured lengths. The viscous cross flow is therefore about 0.45 of the total velocity and 0.20 of the free stream velocity. The total local velocity is therefore about 0.44 of the free stream velocity.

From the model symmetry and test conditions, the flow should be symmetrical about the vertical axis. The direction of the flow on the vertical center line should not be inclined to the vertical axis. Very slight errors in positioning the tuft at the centerline of the model resulted in the errors at these locations. This was observed during the tests. It was extremely difficult to set the tuft exactly over the centerline of the model. A slight tap on the probe positioning mechanism, prior to tightening the set screws, would result in an observable sidewash angle. One observes from the equivalent tuft pictures that the flow exterior to the body is not significantly affected by viscosity well beyond the mid-body position. At 40 inches from the nose, not shown in this figure, no definite pattern of the secondary flow had developed. The viscous components of the velocity were still small compared to the total local velocities. At about 48 inches from the nose ( $3/4$  of the body length), the viscous part of the flow starts to constitute a greater percentage of the local velocities near the body and a definite pattern begins to form. This pattern intensifies along the body until it leaves the model at 64 inches from the

nose as a downward flow from the origin, turning upward to a swirling motion at the top part of the body.

The increase of the viscous part of the cross flow can also be seen to be moving into more of the flow in the regions away from the upper part of the body. The decrease in the local velocity is also evident in the same regions.

The cross flow on the aft end of the body somewhat resembles that for a pair of vortices in the presence of a cylinder.

#### Total Vorticity Distribution

Lines of constant non-dimensional total vorticity in the region about the body at various axial locations, are shown in Figure 23 viewed from downstream. The different magnitudes are denoted by the symbols shown.

The total vorticity expresses the rotation of a fluid particle arising from the presence and action of viscous shearing stresses. The axis of rotation is not given in these plots. The circumferential, radial, and axial components can be used to determine the axis of rotation of the particles at any point in the field. The components of the rotation are those associated with the right hand rule. For example, the axial component of vorticity, pointing in the downstream direction, is associated with a counterclockwise rotation of the particle about the

x-axis, as viewed from the downstream direction, that is, along the negative x direction.

For the non-dimensional vorticity plots given, a value of the non-dimensional vorticity is associated with a rate of change of the velocity with distance, at a point, differing from that of the potential flow. As an example, let:

$$2.5 |\zeta| = 1.0$$

from the plots. Then the dimensional vorticity would be:

$$|\gamma| = \frac{\zeta V_o}{r_{\max}} = 0.4 \frac{V_o}{r_{\max}}$$

or at that particular point, the velocity change in a distance of one maximum radius of the body would be four tenths of the free stream velocity.

Lines connecting the points are only drawn for every other set of symbols. As in the equivalent tuft pictures, the trace of the body in each of the planes perpendicular to the axis is shown.

The growth and extent of the viscous region is clearly presented by these plots. They show that the vorticity is strongest near the body and decreases till it is negligible at some distance away from the body. At the nose of the model very little vorticity is evident. As the distance from the nose is increased the vorticity moves into the field away from the body. The vorticity on the top part of the body, even at the forward part of

the model, penetrates further into the flow than at the side or bottom.

These vorticity plots show evidence that a very complicated real flow exists. The model of a vortex sheet, rolling up into a pair of concentrated vortices, is a high simplification of the actual flow.

The components of the vorticity in the circumferential radial and axial directions are covered in the next sections.

#### Circumferential Component of the Vorticity

The distribution of the circumferential component of the vorticity in the field about the body, at the various longitudinal positions, is shown in Figure 24. The strength associated with each symbol is shown in the key on the figure. The data is plotted in the same manner as described in the previous section on the total vorticity. Since the positive direction was assumed to be in the counterclockwise direction as viewed from the downstream direction, in the calculations of this component, Figure 18, the flagged points on the curve indicate the opposite or negative direction from that assumed.

The circumferential component of vorticity is similar to that normally associated with axial flow boundary layers.

Comparison of the iso-vorticity lines of the circumferential component of the vorticity with those for

the total vorticity indicate both to have somewhat similar patterns. At the forward locations on the body the iso-vorticity lines for the total and the circumferential component having the same strength are almost at the same locations. At distances further aft, an iso-vorticity line for the circumferential component of vorticity is located, in general, at a lesser distance away from the body than a total vorticity line of the same strength. This seems to be especially true over the top and side portions of the body, away from the vertical centerline. One sees this most clearly at the rearmost plane. The vorticity appears to be primarily in the circumferential direction although other components exist. This, along with the primarily clockwise direction, indicates the axial flow component of the boundary layer to be prevailing.

#### Radial Component of the Vorticity

The distribution of the radial component of vorticity in the various planes along the axis of the body, is shown in Figure 25. The magnitude associated with each of the symbols is shown in the key on the figure. In the computation of the radial component, the positive direction was assumed to be directed along the outward radial direction, Figure 18. The flagged points indicate a negative direction of the component whereas the un-

flagged symbol indicates the radial component to be in the positive direction.

The axial component of vorticity is associated with rotations of the particles of fluid about the line normal to the surface of the body, the rotation being that of a right hand screw.

There is hardly any radial component on the front part of the body. The amount shown at the top and bottom of the body is very small in magnitude and is also located very close to the body. There is also a region on the top of the body where the radial vorticity component is directed outward and a region where it is directed inward.

At the mid-longitudinal position, a slightly stronger radial component is present near the very top of the body. On the sides and bottom, the radial components are very small and close to the body.

Progressing aft, a region of inwardly directed radial component is seen to develop on the top and bottom of the body. On the sides, the radial component is directed outward and appears to move further away from the body at each station. However, as the body cross section decreases the lateral position seems to remain constant.

Based on the last two aft locations, one surmises that the region of outwardly directed radial component overlaps a very weak inwardly directed component very



close to the body. Further away from the body, and especially on the sides, there is a region of outwardly directed component. But, it too, is not very strong.

The iso-vorticity plots of the rearmost plane of the body indicates that the radial component of vorticity is confined to a rather small area on leaving the body. The regions of maximum strength appear, in comparison to the previous station, to be moving inward as well as downward.

#### Axial Component of the Vorticity

The axial component of vorticity, in the planes at the various longitudinal stations, is shown in Figure 26. The strength of the vorticity associated with each of the symbols is shown in the key on the figure.

The axial component of vorticity is approximately the same as the trailing component of vorticity found behind lifting wings.

At 8 inches from the nose of the model, the effect of the support wires and forward mounting fitting was evident in the lateral and vertical velocity components. Plots of these velocity components showed a decrease in the velocity at locations behind the support wires. Thus a relatively smooth curve of the velocity component would have a dip in the curve at these points. This is reflected in the x-component of the vorticity at 8 inches

from the nose. The data at 8 inches from the nose will therefore not be relied on to any extent.

Observing all of the data first, it can be seen that at all of the axial stations the axial component of vorticity is zero at the body surface. It then increases to a maximum value at some point away from the body and decreases again further from the body.

On the forward part of the body, up to the mid-longitudinal position, the axial component of vorticity is primarily limited to the upper part of the body. The maximum value is located at an angle of about 45 degrees from the top meridian of the body. From the data at the rearward stations and the fact that the vorticity at the body surface is developed primarily due to the boundary layer, and is therefore almost entirely in the circumferential direction at the body, one expects that the iso-vorticity lines do not terminate at the body. Instead they form closed curves very close to the body, in those regions where measurements were not made. A very small amount of axial vorticity is observed very close to the body on the lower portions of the forward axial stations.

Beyond the mid-point of the body, the iso-vorticity lines of the axial component of vorticity extend from the bottom portion of the body around to the top. The maximum iso-vorticity line is still seen to be close to

the body, being located in the regions near the body where measurements were not made.

At 56 inches from the nose, the region of maximum axial vorticity starts moving away from the body. As the distance is increased further aft, the region of maximum vorticity not only moves farther away from the body but also the magnitude of the maximum value increases.

At the extreme aft end of the body, 64 inches from the nose, a vortex mound similar to that reported by Harrington <sup>9</sup> is seen. The axial vorticity is seen to be concentrating in a region on the leeward side of the body.

## CHAPTER V

### ANALYSIS AND DISCUSSION

The experimental data in terms of the pressure distribution, the surface flow, the cross flow streamlines and the vorticity distribution are certainly related, one to the other. If their relationship is understood, then it can be said that the flow over a body of revolution is somewhat better understood. This does not mean that with this understanding analytical solutions are now possible. The analytical solutions are based on the Navier Stokes equation. For this rather complicated shape, the mathematical difficulties are such precluding any exact analytical solution, even with a better understanding of the mechanism of the flow. At best it is hoped that an understanding of the mechanism of the flow will help in formulating simplified mathematical models including the more important aspects and to evaluate or apply existing mathematical models <sup>4,12</sup>. An attempt will now be made in relating the various experimental data.

#### Relationships Among the Data

First consider the surface traces, or the wall streamlines, of Figure 21. According to Maskell the line of convergence of the wall streamlines, seen extending from the top fore part of the body along the flanks then to the rear aft part of the body, is a separation line <sup>8</sup>. Maskell's analysis, as shown in Figure 2,

implies that the wall streamlines join in pairs of two at the separation line then leave the body. The sheets shown in cross section in Figure 2 are thus made up of the separating streamlines. The top and bottom meridional lines are considered to be attachment lines. That this is the case is not evident. The wall streamlines must either originate at an infinite distance forward of the body and continue to an infinite distance aft of the body or form closed curves on the body. The questions can be asked as to what are the so called attachment lines and how are they formed as continuation of the exterior streamlines? Does the attachment line consist of the locus of the exterior streamlines and the separation line a locus of these streamlines leaving the body?

The potential solution shows the surface streamlines for a body at an angle of attack of 6 degrees to be of the form shown in Figure 27, which looks like the upper left hand sketch of Figure 2. A single streamline at the forward stagnation point would divide into the various surface streamlines. These in turn recombine at the rear stagnation point and trail off as a single streamline. In the case of a two dimensional body, such as an airfoil or cylinder, the stagnation streamline divides into two parts forming the upper and lower surface. In the three dimensional body of revolution it divides into an infinite number of surface streamlines forming the body.

Any other streamline, such as the ones in the vertical plane of symmetry above and below the stagnation streamline, would not join the body. This can further be seen by imagining the body to be rotated slightly. A streamline slightly displaced from the vertical plane of symmetry would also remain away from the body even though it may be very close to the surface.

The same argument applies to the actual surface streamlines of Figure 28. The so called attachment lines and separation line of Figure 2 are not the loci of free streamlines attaching and separating from the body. They are in reality the lines where the stagnation streamline separates forming the surface streamlines and the line where the surface streamlines recombine into a single streamline leaving at the rear stagnation point.

The surface streamlines can be explained in terms of the pressure distribution and the flow about the body. From the total vorticity plots of Figure 23, one can see that the vorticity region on the forward part of the body is very small and confined close to the body. The underlying boundary layer region may be still smaller than the vorticity region. The pressure distribution over a great portion of the body does not differ significantly from that for a potential flow, as seen in Figure 19. Thus the pressure, as hypothesized by Prandtl, is essentially constant across the boundary layer for the

large radii of curvature of the body.

At the surface of the body the velocity is zero. Very close to the surface of the body, say within the size of the particle of titanium oxide or the film of oil, the velocities are very low and therefore the inertia forces would also be small. A particle of the titanium oxide will be acted on by both shearing stresses and the pressure forces, the latter being essentially constant across the boundary layer over most of the body. The motion of the particle will be determined by the action of this force system.

In those regions of the body where the pressure gradients are quite large, the pressure forces would strongly affect the motions of the particle. Neglecting the shearing forces, the particle would then move toward the minimum pressure line.

In the regions where the pressure gradients are quite weak, the shearing stresses would largely dictate the motion of the near surface particle. Neglecting the pressure forces, the particle would then move in the direction of the potential streamlines.

The circumferential pressure coefficients were cross plotted, from Figure 19, at various axial stations. Representative plots are shown in Figure 29, along with the values of the potential solution. These show the good agreement with potential flow over most of the body.

Because of the development of the secondary flows on the aft end of the body, Figure 22, the pressures differ significantly from the potential values at the rear stations. The pressure coefficients on the extreme lee side do not differ from potential theory as much as they do on the windward side. On the windward side they are somewhat greater than predicted by potential theory.

The minimum pressure points at the various axial stations were estimated from Figure 29 and plotted in Figure 30. Also shown is the minimum pressure line as given by potential theory. The line of convergence of the surface streamlines (the separation line) of Figure 21 was approximately at the location indicated on Figure 30. Its location on the front end of the body was not very distinct in the surface trace tests. However, since the boundary layer is quite thin at the forward end of the body and a pressure gradient exists, as shown in Figure 29, the separation line and minimum pressure line should be very close together.

On the aft end of the body the existence of the secondary flow, Figure 22, and the pressure gradient, Figure 29, again result in the minimum pressure line and separation line being close together.

However, in the mid portion of the body a difference between the minimum pressure line and the separation line is evident. The pressure gradient in this mid region is



rather gradual. The shearing stresses in this region primarily determine the motion of the surface particles. As noted on Figure 30, the separation line is on the leeward side of the minimum pressure line.

Thus, the separation line does parallel, although not completely, the minimum pressure line as suggested by Allen and Perkins<sup>10</sup>. The shearing stresses acting affect the location, primarily in the mid-portion of the body where the pressure gradient is small.

#### Generation and Distribution of Vorticity

As the distance from the body increases, the streamlines approach those given by potential flow. Since the surface flow differs greatly from the potential direction on the top part of the body, the boundary layer would be highly skewed there. Some skewness would be present on the bottom surface as well, but not as great as that on the top surface. This is apparent in the vorticity plots where, even from the most forward positions, the greatest amount of vorticity exists on the leeward side of the body. The vorticity plots also show the circumferential component of vorticity to be quite strong over the entire body. On the forward part of the model, the vorticity is almost completely in the circumferential direction. In fact the vorticity originating near the body along its length is primarily in the circumferential direction, indicating the strong axial boundary layer flow.

Because of the skewness, and also since the vorticity is convected with the exterior flow and diffuses through the fluid, the vorticity starts to orient itself in the axial direction.

The radial component remains rather weak over most of the field compared to the axial and circumferential components, as would be expected.

#### Comparison With Other Studies

Studies concerned only with the axial component of vorticity or the cross flow, such as that of Harrington<sup>9</sup>, or NACA<sup>4,5</sup>, give plots similar to the equivalent tuft pictures of Figure 22 and the axial vorticity plots of Figure 26.\* Based on these alone, one might conclude that the vorticity rolls up into a pair of concentrated axial vortices fed by a vortex sheet. However, if this were so then the areas of concentrated vorticity would also show up as areas of concentrated vorticity in the total vorticity plots of Figure 23. Instead there is no noticeable change in the pattern. The plots of the circumferential vorticity, Figure 24, however, indicate a decreased amount of circumferential vorticity in the regions of strongest axial component. There are regions

---

\* Mr. Jorgensen<sup>4</sup>, in a telephone conversation with the author, said he was not aware of any studies considering the other components of vorticity. The model of the concentrated pair of vortices was deduced from the visual flow observations using the vapor screen technique.

of circumferential components of vorticity in the field about the body which are just as strong, if not stronger, than the maximum axial components.

It appears from the vorticity plots that the vorticity does not bundle together strongly, or concentrate, over the body. Rather, the dynamics of the flow causes the vorticity to start tipping more in the axial direction in the region above the body. Far enough in the wake of the body, the regions of vorticity more than likely do form into an axially oriented pair of concentrated vortices, similar to what occurs in the flow behind a finite wing.

Thus, the answer to the question of the origin, or forward located attachment point of the concentrated vortex pair, is that an origin does not exist on the body. In fact, the concentrated vortex pair fed by a weak vortex sheet does not exist over the body. When viewed from the aft end of the body a strong axial component gives the appearance of a vortex pair. The greatly simplified models of a pair of concentrated vortices do give cross flows which resemble those of Figure 16. The strong circumferential components must also have some effect, probably more in the axial than cross flow direction.

## CHAPTER VI

### SUMMARY AND CONCLUSIONS

#### Origin and Importance of the Problem

Previous studies indicated that further investigations pointed at the understanding of the flow over a body of revolution at an angle of attack were needed <sup>4,5</sup>. These studies had concluded that a pair of axially oriented concentrated vortices, increasing in strength along the body and fed by a vortex sheet, formed over the top of the body. The forward location of the attachment point of the vortex pair was not determined.

The understanding of the flow over a three-dimensional body of revolution is important in the field of Fluid Mechanics. This understanding is necessary in order to deal with problems concerned with the interference effects between a body and its aft located stabilizing surface.

#### Statement of the Problem

In order to obtain a better understanding of the mechanism of the flow, the present study was undertaken. The study was directed toward determining the difference between the actual flow over a body of revolution and that predicted by potential theory. Since this difference is manifested in terms of vorticity in the flow field about the body, the study was specifically pointed at determining, 1) how the vorticity is generated along the body, 2) how it is distributed and 3) what are its most

important components. It was also desired to investigate the forward attachment point on the body of a pair of concentrated vortices mentioned by other investigators.

#### The Potential Solution

The potential solution of the problem is discussed in Appendix A. It was used to obtain the surface streamlines for comparison with the actual surface streamlines. The potential solution was also used to help reveal the real effects of the flow in the cross flow planes.

#### Procedure of the Investigation

An ellipse of revolution having a slenderness ratio of 8:1 was chosen as the body to be investigated. Tests were conducted in a wind tunnel with the body at an angle of attack of 6 degrees. The Reynolds number was about  $2.8 \times 10^6$  based on the body length. The flow was turbulent over most of the body.

The velocity field was measured about the body at various axial positions along the body. A tuft of baby yarn was used, along with a pair of simple sighting scopes, to determine the direction of the velocity at various points in the field surrounding the body. The magnitude of the velocity at the same points were measured by means of a three prong rake consisting of two total head tubes and a static tube. Corrections to both sets of measurements were applied from calibration curves

obtained for the tufts and for the rake in a jet of known velocity and direction.

The velocity field data was used to obtain plots of the cross flow due to the viscous effects, at various axial stations along the body. In these plots, the velocity as given by a potential solution was subtracted from the measured cross flow components of the velocity field. The resulting cross flow indicated a pattern similar to that for a vortex pair in the presence of a cylinder.

The vorticity field about the body was also calculated from the experimental velocity field. Iso-vorticity lines of the axial, radial, and circumferential components, as well as of the total magnitude of the vorticity, were plotted in planes perpendicular to the longitudinal axis at various longitudinal positions.

Surface streamlines were made visible by painting the body with a mixture of titanium oxide in kerosene, with a slight amount of oleic acid added to disperse the particles of titanium oxide more uniformly, and exposing the model to the flow in the wind tunnel.

Pressure distributions over the body were also obtained.

### Results

Plots of the vorticity in the field about the body showed that the vorticity near the body was primarily in the circumferential direction. As the vorticity was

carried with the flow it started to deflect in the axial direction, especially in a region above the body. At the end of the body, the greatest amount of vorticity was still strongly oriented in the circumferential direction. The radial component of the vorticity was quite small compared to the other two components.

Pressure distributions over the body showed that potential theory predicted the pressures quite well over most of the body, except near the aft end. At the aft end of the body, the pressure coefficients for a short distance measured circumferentially from the top center line of the body became increasingly larger than that predicted by potential theory.

The surface streamlines indicated a different pattern than the potential streamlines. The streamlines from the top and bottom of the body converged at a line that extended from the upper fore part of the body to the rear aft part of the body. The line at which the upper and lower surface streamlines converged was approximately at the minimum pressure line at the forward and aft end of the body. However, on the mid-portion it was somewhat higher on the lee side of the body than the minimum pressure line.

Near the surface of the body the velocities are lower because of the boundary layer growth along the body. In the very low velocity regions of the boundary layer

the particles of fluid are influenced by the pressure distribution on the body and the shearing stresses and as a result flow toward a common line called the separation line. This results in a highly skewed boundary layer on the top of the body where the surface flow direction is quite different from that at a distance from the surface. It is this highly skewed boundary layer that generates the vorticity in the manner previously indicated.

#### Conclusions

The surface flows, the external flow, the vorticity and the pressures on the body all exist at the same time. In reality it cannot be said that one causes the other. However, for analysis purposes this is often done. Taking this liberty, the mechanism of the flow can be stated to occur in the following manner:

1. The pressure distribution and shear stresses near the body causes the flow near the surface to be quite different in direction from the flow away from the body, especially on the upper part of the body. This results in a highly skewed boundary layer.

2. The vorticity generated by the skewed boundary has the strongest component in the circumferential direction in agreement with axial boundary layer flow. As the vorticity is transported with the flow away from the body it starts to tip resulting in an axial component. The greatest amount of turning occurs in a region on the



leeward side of the body. The radial component is small.

3. The presence of the vorticity affects the pressure distribution of the body. This effect is quite small except near the aft end of the body where a great amount of secondary flow occurs.

Certain conclusions can now be made regarding the ~~items posed in the statement of the problem.~~

1. The vorticity is generated by a skewness of the boundary layer resulting from the low velocity regions near the body being influenced by the pressure forces and viscous forces. This results in the flow on the lee side of the body ~~to~~ deviate appreciably from the potential flow.

2. The vorticity increases in strength along the body length. It is transported with, and diffuses through, the flow thus covering a larger region on the top part of the body than on the bottom. As the vorticity is transported with the flow it starts to assume more of an axial direction.

3. The strongest component of vorticity is that in the circumferential direction and is associated with the axial component of the boundary layer flow. The axial component of vorticity is also an important component. It is associated with the secondary motions in the cross flow planes. The radial component, associated with secondary motions in a plane normal to the body surface, is very weak.

4. A symmetrical concentrated vortex pair, fed by a weak vortex sheet, does not exist. The axial component of the vorticity gives the impression of the existence of this vortex pair. Actually, a much stronger circumferential component of vorticity is present. Thus, the attachment point of the vortex pair onto the body, sought by various investigators, also does not exist.

It can be concluded that:

1. The mechanism of the flow has been made clearer by considering the total vorticity rather than the axial component alone.\* Although the mechanism has been made clearer, much work has to be done in formulating mathematical models for purposes of analytical predictions. The results of this study will be of value in these formulations.

2. The flow is very complex including skewed boundary layers, vorticity generation and vorticity transport. Much work needs to be done concerning these items in order to obtain a clarification of the problem beyond that of this report. Studies of these items are still being made. It is hoped that someday they will be applied to explaining the results of this investigation in more detail.

---

\* Mr. Jorgensen<sup>4</sup>, in a telephone conversation with the author, said he was not aware of any studies considering the other components of vorticity. The model of the concentrated pair of vortices was deduced from the visual flow observations using the vapor screen technique.

3. A mathematical model of a pair of concentrated vortices on the leeward side of the body is a high simplification of the actual flow. As in all simplifications, the adequacy of the model depends on what is being sought. A model of a pair of concentrated vortices with finite cores seems to predict the downwash and side-wash angles to a reasonable accuracy except in the region between the vortices and through the vortex cores <sup>4</sup>.

A model describing the actual flow more accurately would include ring vortices about the longitudinal axis. Of course, this would make calculations more difficult.

4. Another possible additional boundary condition for obtaining an analytical solution is the line of convergence of the surface streamlines at the minimum pressure points. The work of Eichelbrenner is aimed at predicting this line <sup>15</sup>. Since the minimum pressure line does not differ greatly over most of the body from that of the potential flow, it is possible that the potential flow minimum pressure line could serve as a first approximation for determining the skewness of the boundary layer and the generation of the vorticity.

The direction of the surface streamlines appear to be parallel to the separation line on the lee side of the separation line. At some distance away from the body the flow should approach that given by potential theory. Assuming this to be at the edge of the boundary layer, then

the flow direction and magnitude is known at two points on a line normal to the body surface. Taylor's work on skewed boundary layers <sup>20</sup> points out a triangular relationship between velocity components perpendicular to the normal line drawn to the surface. This fact, applied between the two points, could serve as an approximation to the skewness.

#### Recommendations for Further Studies

As a result of this investigation certain recommendations can also be made.

1. Attempts should be made at formulating a mathematical model including the circumferential components of vorticity. Hill's work <sup>12</sup> should serve as a good starting point.

2. Various methods that have been investigated regarding skewed boundary layers, vorticity generation, and vorticity transport should be applied to the data obtained in order to explain the results of the present investigation in more detail.

3. The data on this investigation could be used by those studying problems of skewed boundary layers, vorticity generation and vorticity transport as data for their investigations.

It is planned to tabulate the data of this investigation and make it available to other investigators

for such studies.

Data has also been obtained, in the manner reported, for the case of the body with a horizontal stabilizing surface attached to the aft end. It is presently being reduced and plotted in the same manner as for the bare body. It is expected that the results will contribute to the understanding of the tail body interference problem mentioned in the introduction.

## REFERENCES

1. Lawrence, E. R. and Flax, A. H. "Wing Body Interference at Subsonic and Supersonic Speeds - Survey and New Developments," Journal of the Aeronautical Sciences, 21:289-324, 1954.
2. Mead, M. H. Observation of Unsteady Flow Phenomena for an Inclined Body Fitted with Stabilizing Fins. National Advisory Committee for Aeronautics RM A51K05. January, 1952. Declassified April, 1957.
3. Stone, R. W., Jr. and Polhamus, E. C. Some Effects of Shed Vortices on the Flow Fields Around Stabilizing Tail Surfaces. Advisory Group for Aeronautical Research and Development Report 108. April - May, 1957.
4. Jorgensen, L. H. and Perkins, E. W. Investigation of Some Wake Vortex Characteristics of an Inclined Ogive - Cylinder Body at Mach Number 2. National Advisory Committee for Aeronautics Report 1371. 1958.
5. Tinling, B. E. and Allen, C. Q. An Investigation of the Normal - Force and Vortex - Wake Characteristics of an Ogive - Cylinder Body at Subsonic Speeds. National Aeronautics and Space Administration Technical Note D-1297. April, 1962.
6. Freeman, H. B. Pressure - Distribution Measurements on the Hull and Fins of a 1/40-Scale Model of the U. S. Airship "Akron." National Aeronautics and Space Administration Report 443, 1932.
7. Lamb, Sir Horace. Hydrodynamics. New York: Dover Publications, Inc.
8. Milne-Thomson, L. M. Theoretical Hydrodynamics. New York: The Macmillan Company, 1957.
9. Harrington, R. P. An Attack on the Origin of Lift of an Elongated Body. PhD. Thesis University of Michigan, 1935.
10. Allen, H. J. and Perkins, E. W. A Study of Effects of Viscosity on Flow Over Slender Inclined Bodies of Revolution. National Advisory Committee for Aeronautics Report 1048, 1951.

11. Mello, J. F. "Investigation of Normal Force Distributions and Wake Vortex Characteristics of Bodies of Revolution at Supersonic Speeds," Journal of Aero/Space Sciences, 26:155-168, 1959.
12. Spence, A. and Trebble, W. J. G. Low Speed Tunnel Tests on the Flow Structure Behind a Body of Revolution of Fineness Ratio 16 2/3:1. Royal Aircraft Establishment Technical Note No: Aero. 2406, October, 1955.
13. Hill, J. A. F. A Non-Linear Theory of Lift on Slender Bodies of Revolution. Proceedings U. S. Navy Symposium on Aeroballistics, NavOrd Report 5338, 1954.
14. Timman, R. "The Theory of Three-Dimensional Laminar Boundary Layers," published in Boundary Layer Effects in Aerodynamics. New York: Philosophical Library, Inc., 1957.
15. Eichelbrenner, E. A. and Oudart, A. Méthode de Calcul de la Couche-Limite Tridimensionnelle. Office National d'Etudes et de Recherches Aeronautiques Publication No. 76, 1955.
16. Eichelbrenner, E. A. Décollement Laminaire en Trois Dimensions Sur un Obstacle Fini. Office National d'Etudes et de Recherches Aeronautiques Publication No. 89, 1957.
17. Thwaites, Bryan (ed.). Incompressible Aerodynamics. London: Oxford University Press, 1950.
18. Eichelbrenner, E. A. and Oudart, A. "Observations sur un Critere de Decollement Laminaire dans la Couche-Limite Tridimensionnelle, La Recherche Aeronautique No. 40, 1954.
19. Maskell, E. C. Flow Separation in Three Dimensions. Royal Aircraft Establishment Report No. Aero 2565, November, 1955.
20. Taylor, E. S. "The Skewed Boundary Layer," Transactions of the ASME Journal of Basic Engineering, 81:297-304, 1959.
21. Lehman, A. F. The Garfield Thomas Water Tunnel. Ordnance Research Laboratory Report NORD 16597-56, September, 1959

22. Maltby, R. L. and Keating, R. F. A. Flow Visualization in Low-Speed Wind Tunnels. Royal Aircraft Establishment Technical Note No. Aero 2715, August, 1960.
23. Pankhurst, R. C. and Holder, D. W. Wind-Tunnel Technique. London: Sir Isaac Pitman & Sons, Ltd., 1952.
24. Smith, Leroy H. Jr., Three-Dimensional Flow in Axial-Flow Turbomachinery. Wright Air Development Center Report 55-348, Volume I, August, 1955.
25. Bird, J. D. and Riley, D. R. Some Experiments on Visualization of Flow Fields Behind Low-Aspect-Ratio Wings by Means of a Tuft Grid. National Advisory Committee for Aeronautics Technical Note 2674, 1952.
26. Glauert, H. Wind Tunnel Interference on Wings, Bodies, and Airscrews. Aeronautical Research Committee R&M 1566, 1933.



## APPENDIX A

### THE POTENTIAL SOLUTION

The potential flow field is governed by Laplace's Equation in terms of the velocity potential,

$$\nabla^2 \phi = 0 \quad (\text{A-1})$$

along with the boundary conditions (1) that there is no flow through the body (that is, the flow is parallel to the body) and (2) that the velocity at a great distance from the body is that of the free stream.

#### Coordinate System

As in any boundary value problem the proper choice of coordinate system greatly simplifies the solution of the problem. For the case of an ellipse of revolution an Ovary semi-elliptic orthogonal coordinate system is chosen <sup>7,8</sup>. This coordinate system consists of a family of ellipse with foci at  $x_1 = \pm 1$ ,  $y_1 = 0$  given by:

$$\frac{x_1^2}{\zeta^2} + \frac{\bar{y}_1^2}{\zeta^2 - 1} = 1 \quad (\text{A-2})$$

A family of hyperboloids of revolution of two sheets confocal with the ellipsoids, that is with foci at  $x_1 = \pm 1$ ,  $y_1 = 0$ , given by:

$$\frac{x_1^2}{\mu^2} - \frac{\bar{y}_1^2}{1 - \mu^2} = 1 \quad (\text{A-3})$$

and planes given by:

$$\omega = \text{constant} \quad (\text{A-4})$$

$\zeta$  and  $\mu$  define the family of ellipsoids and hyperboloids respectively and  $x, y, \omega$ , a cylindrical coordinate system. The left handed rectangular coordinate system,  $x_1, y_1, z_1$ , with its origin at the mid point, the  $x_1$  axis pointed downstream and the  $y_1$  axis in the crossflow direction, is related to the  $\zeta, \mu, \omega$  coordinate system by the relations:

$$\begin{aligned} x_1 &= \mu \zeta \\ y_1 &= \left[ (1-\mu^2) (\zeta^2-1) \right]^{1/2} \cos \omega \\ z_1 &= \left[ (1-\mu^2) (\zeta^2-1) \right]^{1/2} \sin \omega \end{aligned} \quad (\text{A-5})$$

Figure 31a is a sketch of the coordinate systems. One should note that the coordinate systems are based on a unit length between the foci of the family of ellipses and confocal hyperboloids.

The ellipsoid of this investigation has a length of 64 inches and a maximum diameter of 8 inches. Designating the radial distance as  $\bar{y}_2$  its equation can be written as:

$$\frac{x_2^2}{L^2} + \frac{\bar{y}_2^2}{R^2} = 1 \quad (\text{A-6})$$

where:

$L = 32$  inches,  $1/2$  of the length of the body.

$R = 4$  inches, the maximum radius of the body.

The distance to the foci of the ellipse is:

$$f = [L^2 - R^2]^{1/2} \quad (A-7)$$

so that the dimensional coordinate system  $x_2, y_2, z_2$  can be related to the non-dimensional system  $x_1, y_1, z_1$  as follows:

$$\begin{aligned} x_2 &= f x_1 \\ y_2 &= f y_1 \\ z_2 &= f z_1 \end{aligned} \quad (A-8)$$

The body can then be shown to be represented by the value of  $\zeta = \zeta_0$  in the non-dimensional coordinate system as:

$$\zeta_0 = \frac{L}{f} \quad (A-9)$$

The data plotted in the main part of the text is with respect to a distance  $x$  measured from the nose, Figure 31b. Thus:

$$\begin{aligned} x &= x_2 + 32 \\ y &= y_2 \\ z &= z_2 \end{aligned} \quad (A-10)$$

The rest of the discussion of this appendix will consider the non-dimensional system. For sake of convenience the subscript 1 will be dropped.

### Solutions of Laplace's Equation

Since Laplace's equation is linear, the solution for an ellipse of revolution can be considered as a sum of the solutions for an axial and transverse motion. These are readily available in terms of the perturbation velocity potential <sup>7,8</sup>.

For axial motion of the ellipse:

$$\phi_A = a_{10} \mu^{1/2} \left[ \zeta \log \frac{\zeta + 1}{\zeta - 1} - 1 \right] \quad (A-11)$$

where:

$$a_{10} = \frac{U}{\frac{\zeta_0^2}{\zeta_0^2 - 1} - 1/2 \log \frac{\zeta_0 + 1}{\zeta_0 - 1}} = K_1 U \quad (A-12)$$

U being the axial component of the velocity.

For lateral motion of the ellipse:

$$\begin{aligned} \phi_L = a_{11} \left[ (1 - \mu^2) (\zeta^2 - 1) \right]^{1/2} \left[ 1/2 \log \frac{\zeta + 1}{\zeta - 1} \right. \\ \left. - \frac{\zeta}{\zeta^2 - 1} \right] \cos \omega \end{aligned} \quad (A-13)$$

where:

$$a_{11} = - \frac{V}{1/2 \log \frac{\zeta_0 + 1}{\zeta_0 - 1} - \frac{\zeta_0^2 - 2}{\zeta_0 (\zeta_0^2 - 1)}} = K_2 V \quad (A-14)$$

V being the lateral component of the velocity.

### Velocity Components

Differentiating the velocity potential in a particular direction gives the velocity in that direction. In terms of the elliptic, hyperbolic coordinate systems, the perturbation velocities can be obtained in the  $x, y, z$  direction as:

$$\begin{aligned}
 u_x &= \frac{\partial \phi}{\partial x} = \zeta \left[ \frac{1-\mu^2}{\zeta^2-\mu^2} \right] \frac{\partial \phi}{\partial \mu} + \mu \left[ \frac{\zeta^2-1}{\zeta^2-\mu^2} \right] \frac{\partial \phi}{\partial \zeta} \\
 u_y &= \frac{\partial \phi}{\partial y} = \frac{[(\zeta^2-1)(1-\mu^2)]^{1/2}}{\zeta^2-\mu^2} \left[ \zeta \frac{\partial \phi}{\partial \zeta} - \mu \frac{\partial \phi}{\partial \mu} \right] \cos \omega \\
 &\quad - \frac{\sin \omega}{[(\zeta^2-1)(1-\mu^2)]^{1/2}} \frac{\partial \phi}{\partial \omega} \\
 u_z &= \frac{\partial \phi}{\partial z} = \frac{[(\zeta^2-1)(1-\mu^2)]^{1/2}}{\zeta^2-\mu^2} \left[ \zeta \frac{\partial \phi}{\partial \zeta} - \mu \frac{\partial \phi}{\partial \mu} \right] \sin \omega \\
 &\quad - \frac{\cos \omega}{[(\zeta^2-1)(1-\mu^2)]^{1/2}} \frac{\partial \phi}{\partial \omega}
 \end{aligned} \tag{A-15}$$

The perturbation velocity components for the axial motion are obtained by substituting the perturbation velocity potential into these equations as:

$$\begin{aligned}
 u_x &= K_1 U \left[ \frac{1}{2} \log \frac{\zeta + 1}{\zeta - 1} - \frac{\zeta}{\zeta^2 - \mu^2} \right] \\
 u_y &= -K_1 U \left\{ \frac{\mu}{\zeta^2 - \mu^2} \left[ \frac{1 - \mu^2}{\zeta^2 - 1} \right]^{1/2} \right\} \cos \omega \\
 u_z &= -K_1 U \left\{ \frac{\mu}{\zeta^2 - \mu^2} \left[ \frac{1 - \mu^2}{\zeta^2 - 1} \right]^{1/2} \right\} \sin \omega
 \end{aligned} \tag{A-16}$$

The total velocity at a point due to the axial motion is:

$$\bar{V}_A = \bar{U} + \bar{u} \tag{A-17}$$

or in terms of the components, and nondimensionalizing by  $U$ :

$$\begin{aligned}
 \frac{v_x}{U} &= 1 + \frac{u_x}{U} \\
 \frac{v_y}{U} &= \frac{u_y}{U} \\
 \frac{v_z}{U} &= \frac{u_z}{U}
 \end{aligned} \tag{A-18}$$

The perturbation velocity components for the lateral motion are obtained, by substituting the axial perturbation velocity potential into equations (A-15), as:

$$\begin{aligned}
 u_x &= K_2 V \left\{ \frac{2\mu}{\zeta^2 - \mu^2} \left[ \frac{1 - \mu^2}{\zeta^2 - 1} \right]^{1/2} \right\} \cos \omega \\
 u_y &= K_2 V \left\{ 1/2 \log \frac{\zeta+1}{\zeta-1} + \left[ \frac{\zeta}{\zeta^2 - 1} - \frac{2\zeta}{\zeta^2 - \mu^2} \right] \cos^2 \omega \right. \\
 &\quad \left. - \frac{\zeta}{\zeta^2 - 1} \sin^2 \omega \right\} \\
 u_z &= K_2 V \left\{ 2 \left[ \frac{\zeta}{\zeta^2 - 1} - \frac{\zeta}{\zeta^2 - \mu^2} \right] \right\} \sin \omega \cos \omega
 \end{aligned} \tag{A-19}$$

The total velocity at a point due to the lateral motion is:

$$\bar{V}_L = \bar{V} + \bar{u} \tag{A-20}$$

or in terms of the components, and nondimensionalizing by  $V$ :

$$\begin{aligned}
 \frac{V_x}{V} &= \frac{u_x}{V} \\
 \frac{V_y}{V} &= 1 + \frac{u_y}{V} \\
 \frac{V_z}{V} &= \frac{u_z}{V}
 \end{aligned} \tag{A-21}$$

For the body at an angle of attack  $\alpha$  in a free stream velocity,  $V_o$ :

$$U = V_0 \cos \alpha$$

$$V = V_0 \sin \alpha$$

Therefore, the components of the total velocity are:

$$\frac{u_p}{V_0} = \frac{V_x}{V_0} - (1 + \frac{u_x}{U}) \cos \alpha + \frac{u_x}{V} \sin \alpha$$

$$\frac{v_p}{V_0} = \frac{V_y}{V_0} - \frac{u_y}{U} \cos \alpha + (1 + \frac{u_y}{V}) \sin \alpha \quad (A-23)$$

$$\frac{w_p}{V_0} = \frac{V_z}{V_0} - \frac{u_z}{U} \cos \alpha + \frac{u_z}{V} \sin \alpha$$

The ratios of perturbation to either the axial or lateral components of velocity are those given by equations (A-16) and (A-19), and cannot be treated as an algebraic ratio in equations (A-23).

#### Pressure Distribution

The pressure coefficient on the body is determined in terms of the local velocity at a point on the body as:

$$C_p = 1 - \left( \frac{V}{V_0} \right)^2 \quad \zeta = \zeta_0$$

where the subscript indicates the velocity ratio  $V/V_0$  evaluated at  $\zeta = \zeta_0$ , that is at the body surface.



The ratio of the square of the total local to free stream velocity is obtained from the total velocity components, equation (A-23).

## APPENDIX B

### EXPERIMENTAL ERRORS

The experimental data obtained dealt with the pressure distribution on the body and measurements of the velocity field about the body in both magnitude and direction.

Certain experimental errors were observed. Some of these were due to interference effects of the tunnel while others were due to the measuring equipment. Various techniques were applied in an attempt to correct for the errors. The purpose of this appendix is to discuss the techniques used to correct the measured data for experimental errors.

#### Pressure Distribution

As indicated in the text on page 28, a precision manometer bank was used to measure pressures for the pressure distribution tests. The same board was also used in the determination of the magnitude of the velocity in the velocity field measurements. Since it was known that the pressure differences would be small for the body used, the board was tipped to about 10 degrees from the horizontal in order to increase its sensitivity. On tipping of the board, the menisci of the tubes were observed to be at different levels. Some of the tubes had their menisci a noticable distance lower than the others. In order to determine the cause of this, as well

as the effect on the measured data, the manometer board was calibrated.

The calibration of the inclined manometer bank consisted of applying a pressure difference across two tubes of the bank at a time. The pressure difference was varied so as to cover the range of levels expected in the tests. One of the tubes was always connected to the tube to which the static pressure tap of the pitot static tube would be connected. The levels of the other tubes were referred to this reference tube in the actual tests. A micro-manometer was connected in parallel with the applied pressure differential in order to determine the applied pressure difference.

The change in level along a tube, as measured from the reference tube, was plotted against the pressure difference determined by the micro-manometer. The plot showed the points for a given tube fell along a straight line. The slopes of the data for the different tubes were essentially the same. Although the tubes were parallel, they did not lie in the same plane. This would result in their menisci, when viewed perpendicular to the face of the board, to be at different heights along the board. Thus, the correction applied to the measured data was the difference in level of a given tube with respect to the reference tube, obtained with the tunnel inoperative. The corrections were very small

and could have been neglected. However, since they were obtained in trying to resolve the fact that the menisci between the tubes did not line up, they were available and were applied to the measured data in the reduction of the data to pressure coefficient form.

Another error entering into the pressure coefficients was the wind tunnel interference. In any wind tunnel testing interference exists between the model, its mounting supports, and the wind tunnel walls. In some cases this interference can be shown to be small. For the pressure distributions of this body it was found that at some points along the body the interference was of the same order of magnitude as the pressure readings.

Neglecting the interference due to the wire mounting system (which should be small), the interference is due to the following <sup>26</sup>: 1) The direct constraint of the boundary of the air stream on the flow past the body,, 2) the additional constraint arising from the existence of a wake of reduced velocity behind the body and 3) the effect of a gradient of pressure along the axis of the wind tunnel.

The direct constraint arises because the rigid walls of the wind tunnel prevent the free lateral expansion of the flow past the body. This type of constraint should be calculable, under the assumptions of a perfect fluid, using potential methods with an appropriate system of

images. Since this problem is the subject of a current investigation at the Water Tunnel, it was not pursued to any extent here. The case of a Rankine Ovoid in a circular tunnel has been calculated by Glauert<sup>26</sup>. He obtained a single interference value to be applied over the entire body. This value is comparable to the interference obtained in the present tests, as explained later, at the maximum cross sectional location of the body.

The constraint due to the wake of the body is deemed to be small for good streamlined bodies. One can formulate an expression for this constraint theoretically, containing an empirical factor which must be obtained for different bodies<sup>26</sup>.

The constraint due to the existence of a pressure gradient in the wind tunnel is caused by the growth of the boundary layer along the test section giving an accelerating flow downstream. This correction is most important for good streamline bodies whose drag is low and relatively unimportant for bluff bodies<sup>26</sup>.

In order to obtain the pressure gradient in the wind tunnel, pressure taps were located at various longitudinal positions in the test section on four of the walls of the octagonal section. The difference between the static pressures at these positions and the static pressure as measured by the pitot static tubes in the forward part of the test section was measured on the inclined

manometer bank with no model in the tunnel. Figure 32 is a plot of the difference in pressure coefficient along the test section as referred to the static pressure of the pitot static tube. Also plotted on this figure is the change in static pressure coefficient as determined by assuming a change in cross sectional area of the tunnel in the downstream direction based on the displacement thickness of the boundary layer.

Since the body tested is slender, and since the ratio of the tunnel cross section to the model diameter is 6:1, one can assume that the change in curvature of the streamlines from that in an infinite fluid does not affect the static pressure distribution in the wind tunnel to as great an extent as does the reduction in cross sectional area due to the presence of the model in the tunnel. If the wake of the model is considered as effectively a continuation of the body, then the same argument would also apply to the wake.

Consider the change in static pressure to be constant across the tunnel, at a given cross section. The corrections to be applied to the static pressure coefficient distribution on the model is then determined by measuring the difference in pressure coefficient at the various taps along the test section of the tunnel as referred to the static pressure of the pitot static tube in the upstream section. Figure 33 is a plot of this

difference in static pressure coefficient along the test section for the model at zero angle of attack. Also shown on this figure is a plot of the change in static pressure coefficient, as determined from continuity considerations considering a reduction of cross sectional area along the tunnel due to a displacement boundary layer thickness and the presence of the model. The wake of the model is not taken into account. Since the static pressure at the pitot static tube and at the wall position at the location of the pitot static tube did not agree, the entire theoretical curve was shifted by the difference at that point. Also shown on the curve is the correction as given by the method of Glauert considering a Rankine Ovoid <sup>26</sup>.

Figure 34 shows the difference in static pressure coefficient along the tunnel as referred to the static pressure of the pitot static tube for the model at an angle of attack of six degrees. Also shown is the case of the model at zero degrees. Since the difference between these two conditions appears to be very small, the corrections to the static pressure coefficients on the model applied to the experimental pressure distribution of the model at zero and six degrees were those of Figure 34. The use of this correction is illustrated in Appendix C.

### Velocity Field

Tests showed that the tuft probe used for determining the sidewash and downwash angles was subject to two effects resulting in an error in the downwash angle as discussed in the text of this report. These effects were a tip effect due to the flow around the tip of the wire supporting the tuft and a weight effect due to the weight of the tuft. The sidewash angle was not affected.

In order to account for the error in the downwash angle, the tuft probe was calibrated in a jet of air inclined at a known angle from the horizontal. A small hot wire calibration tunnel was used as the jet supply. A photograph of the calibration set up is shown in Figure 35.

The calibration tunnel is a small low turbulence wind tunnel used to calibrate hot wires. It is driven by a blower from a commercial vacuum sweeper. The speed of the blower and thus the velocity of the jet is controlled by means of a Variac. The jet velocity is measured by the inclined manometer shown in the foreground.

The tuft probe was positioned in the jet and the tuft angle measured using the sighting tubes described in the text and shown in Figure 8.



If:

$\sigma_T$  = the known jet direction measured from the horizontal,

$\sigma_m$  = the measured tuft angle measured from the horizontal,

and

$\sigma_c$  = the correction angle,

then

$$\sigma_c = \sigma_T - \sigma_m \quad (B-1)$$

The correction angle,  $\sigma_c$ , was obtained over a range of velocities for a given jet direction. The tunnel was then tipped to give a different jet direction, and the velocity varied once more.

Figure 36 shows the calibration curve for a given tuft. One can see that this particular tuft could be in error as high as  $\pm 5$  degrees, depending on its position in the field about the body. In regions where the magnitude of the velocity would be smaller than tested, the error could be larger.

Tests showed that different curves were obtained each time a new tuft was used. This was believed to result from slight differences in the way the tuft was attached to the probe. Even though extreme care was exercised in attaching a new tuft to the probe, as described in the text, it was not possible to align the small wire, passing through the mounting loop and glued to the tuft, in the same direction along the tuft at all

times.

However, tests showed that the calibration curve for a given tuft held for the life of the tuft. Recalibrations during the use of a tuft indicated the same errors. After a period of time the tuft started to fray at the loose end and would start to flutter. The calibration still was repeatable in this condition. Because of the flutter, the tuft was discarded and a new one used after calibration.

Since the rake of Figure 13, used to measure the total and static pressure in the field about the body, was always aligned in the direction of the longitudinal axis of the tunnel, an error could exist at each tube of the rake due to its misalignment with the local velocity direction at the tube.

Each of the tubes of the rake was located, in turn, in the center of the calibration jet discussed previously. The test set up was similar to that of Figure 35. The rake probe was oriented at different yaw and pitch angles.

If a total head tube was being calibrated, the tip of the tube was maintained at a point at the exit (throat) of the tunnel while yawed or pitched. Letting

$P_{T_T}$  - the true total pressure, assumed to be that for the total head tube aligned with the flow,

$P_{T_m}$  - the measured total pressure with the total head tube at either a yaw or pitch angle,

$P_o$  = the static pressure at the exit,  
 $q_o = 1/2 \rho V_o^2$ , the dynamic pressure at the exit,  
 then the error in the total pressure, divided by the  
 dynamic pressure, was defined as:

$$\Delta C_{P_T} = \frac{\Delta P_T}{q_o} = \frac{(P_{T_T} - P_o) - (P_{T_m} - P_o)}{q_o} \quad (B-2)$$

$$= \frac{P_{T_T} - P_{T_m}}{q_o}$$

The difference between the total pressure and the static pressure was measured using a micro-manometer. The dynamic pressure was obtained from the inclined manometer of the calibration tunnel.

The error in the total pressure coefficient defined by equation (B-2) was plotted against the yaw and pitch angle for both total pressure tubes. A single curve, fitting both the yaw and pitch conditions, was drawn through the points. This curve is shown in Figure 37 plotted against  $\psi$ , the included angle between the axis of a total pressure tube and the velocity at the tube.

In calibrating the static head tube, the static holes were maintained at a point in the exit of the calibration tunnel while yawing and pitching the probe. Letting:

$P_{o_T}$  = the true static pressure, measured by a tap  
 on the exit of the tunnel,

$P_{o_m}$  - the static pressure as measured by the tube, then the error in the measured static pressure, divided by the dynamic pressure, was defined as:

$$\Delta C_{Po} = \frac{P_{oT} - P_{om}}{q_o} \quad (B-3)$$

The error in the static pressure coefficient defined by equation (B-3) was plotted against the yaw and pitch angle. A single curve, fitting both the yaw and pitch conditions, was drawn through the points. This curve is also shown in Figure 37 plotted against  $\psi$ , the included angle between the axis of the static pressure tube and the velocity at the static holes of the tube.

Knowing the sidewash and downwash angles at a point from the tuft measurements, these could be combined to obtain the angle  $\psi$  at a point. A plot of the total pressure, obtained from the two total pressure tubes, versus the distance traversed could be used to determine the total pressure at the location of the static pressure tube. (This was actually performed using a three point interpolation on an IBM 1620 computer, Appendix C). The corrected velocity at a point is then given as:

$$\left(\frac{V}{V_o}\right)_T = \left[\left(\frac{V}{V_o}\right)_M^2 + \Delta C_{PT} - \Delta C_{Po}\right]^{1/2} \quad (B-4)$$

In the discussion of the wind tunnel interference on the pressure measurements it was mentioned that, for this slender body and ratio of model to tunnel diameter, it was believed the presence of the tunnel walls did not affect the curvature of the streamlines to any extent. If this is the case, the local flow directions would not be affected by the presence of the wall. In any case, the wall effects on the flow directions were not accounted for.

## APPENDIX C

### DATA REDUCTION

#### Pressure Coefficients

Let  $P_i$  be a pressure reading and  $h_i$  the corresponding reading of the manometer board in inches. The subscripts  $i$  denote a particular pressure reading.

$i = 0$  : the pressure or manometer reading of the static orifice of the pitot-static tube located in the tunnel test section well forward and above the model. All pressure levels of the manometer board were referred to this level.

$i = T$  : the pressure or manometer reading of the total pressure of the pitot-static tube located in the tunnel test section well forward and above the model.

$i = 1, 2, 3, \dots, n, \dots, 18$ : the body static pressure taps at the locations along the body.

The measured pressure coefficient at a location on the body at tap  $n$  is then:

$$C_{PM} = \frac{P_M - P_0}{1/2 \rho V_0^2} \quad (C-1)$$

where  $M$  indicates the measured (uncorrected) value.

In terms of the manometer board readings, since the density of the manometer fluid as well as the angle of inclination of the board cancel from the equation, the pressure coefficient can be written as:

$$C_{PM} = \frac{h_n - h_o}{h_t - h_o} \quad (C-2)$$

If  $\epsilon_n$  is the error in the difference between levels of tube  $n$  and  $i = 0$ ,  $\epsilon_T$  is the error between tube  $i = T$  and  $i = 0$ , then correcting for errors in the tube readings:

$$C_{PM} = \frac{h_n - h_o + \epsilon_n}{h_T - h_o + \epsilon_T} \quad (C-3)$$

The errors were found to be very small and could have been neglected. Since they were available, having been obtained in trying to resolve a peculiar behavior of the menisci of the tubes on inclining the board (Appendix B), they were taken into account in the calculations. At most the variation was about 0.05 inches along the manometer scale. This corresponds to an error of the pressure coefficient of about 0.003 which is hardly discernable on the pressure plots in the text.

Since a static pressure gradient existed along the length of the tunnel, the static pressure  $P_o$  of equation (C-1) was corrected at each tap  $n$  by the difference in static pressure at that point and at a point in the test section well ahead of the model. In terms of the pressure coefficient of the static pressure gradient, the corrected pressure coefficient at a tap  $n$  can be written as:

$$C_p = \frac{(P - P_o) + (P_o - P_{on})}{1/2 \rho v_o^2} \quad (C-4)$$

$$= C_{pm} + \Delta C_p$$

where  $P_{on}$  is the value of the static pressure on the wall at the axial location of the tap  $n$ , and  $\Delta C_p$  is the static pressure difference along the wall nondimensionalized by the dynamic pressure shown in Figure 34. This correction was sizeable compared to the measured values of the pressure coefficients.

#### Velocity Field

Let:

$P_o(y)$  be the static pressure measured at a point  $(x, y, z)$  by the static tube of the rake,

$P_T(y+.35)$  be the total pressure measured at a point  $(x, y + 0.35, z)$  by the total pressure tube of the rake 0.35 inches above the static tube,

$P_T(y-.35)$  be the total pressure measured at a point  $(x, y - .35, z)$  by the total pressure tube of the rake 0.35 inches below the static tube,

$P_o$  be the static pressure of the pitot-static tube located well forward and above the model,

$P_T$  be the total pressure of the same pitot-static tube.

Then at the point  $(x, y, z)$ , the measured local to free stream velocity ratio is:



$$\left| \frac{v}{v_o} \right|_m = \left[ \frac{P_T(y) - P_o(y)}{P_T - P_o} \right]^{1/2} \quad (C-5)$$

In terms of the manometer readings, with  $h_o$  the free stream static pressure reading as the reference level:

$$\left| \frac{v}{v_o} \right|_m = \left[ \frac{(h_T(y) - h_o) - (h_o(y) - h_o)}{h_T - h_o} \right]^{1/2} \quad (C-6)$$

Since the total pressure tubes of the rake were located at 0.35 inches above and below the static pressure tube, it was necessary to interpolate to get the total pressure at the same location as the static pressure tube. This was done by fitting a second degree curve through the total head readings at three points. Two of the points were those of the top and bottom tube. The third point was the total head reading of the bottom tube obtained with the rake moved a distance  $\Delta y$  upward. In other words, the static pressure was measured at a point  $(x, y, z)$ . In order to obtain the total pressure at this point, a least square fit of a second degree polynomial through the data at the points  $(x, y + .35, z)$ ,  $(x, y - .35, z)$  and  $(x, y - .35 + \Delta y, z)$  was used for interpolation. The actual data reduction and interpolation was performed on an IBM 1620 computer.

The measured velocity ratio was corrected for flow inclination at the same time that the correction to the

downwash angle was being made.

Assuming that the downwash angle  $\sigma$  has been corrected, then  $\sigma$  and the sidewash angle  $\tau$ , can be combined to obtain the total angle,  $\psi$ , included between the rake tube axis (same as the tunnel longitudinal axis) and the local velocity at the point. The corrected velocity ratio is then:

$$\left| \frac{v}{V_o} \right| = \left[ \left| \frac{v}{V_o} \right|_M^2 + \Delta C_{PT} - \Delta C_{Po} \right]^{1/2} \quad (C-7)$$

where  $\Delta C_{PT}$  and  $\Delta C_{Po}$  are the errors due to the total and static pressure tubes being inclined to the flow, Figure 37.

The downwash angle  $\sigma$  and the sidewash angle  $\tau$  were read directly from the scope. Since there was no correction to the sidewash angle:

$$\tau = \tau_M \quad (C-8)$$

where again the subscript M indicates measured values.

The tuft calibration plot, Figure 36, was used to correct for the error in the measured downwash angles,  $\sigma_M$ . The velocity at the point where the downwash angle was measured was taken to be the measured velocity ratio multiplied by the tunnel velocity of 100 ft. per. sec. The error in the downwash angle was then obtained, for this velocity and downwash angle, from Figure 36. The corrected downwash angle is then:

$$\sigma = \sigma_M + \text{correction angle} \quad (\text{C-9})$$

As mentioned previously, the corrected downwash angle and sidewash angle were then used to correct the velocity ratio. Repeating the procedure with the corrected velocity ratio and the new value of the downwash angle did not significantly affect the corrections to any extent. Thus, unless the first correction was extremely large, which occurred at low velocity ratios, a reiteration was not made. Where the corrections were large, a reiteration was made. The second correction was all that was needed in these cases.

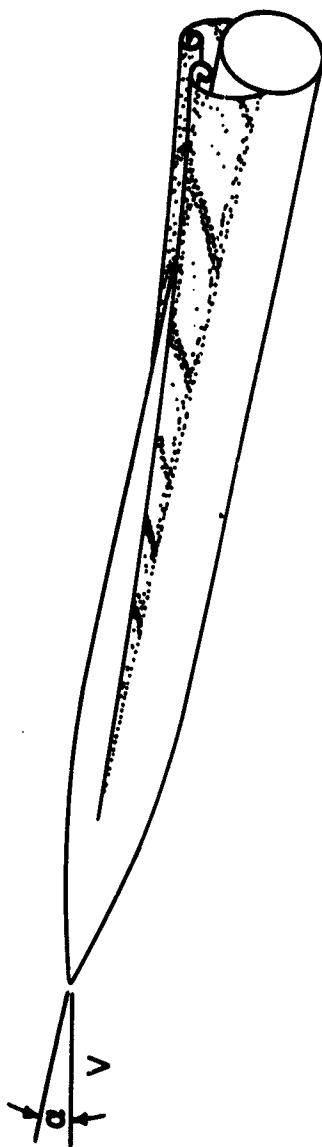


Figure 1. NACA, Spiral Vortex Sheet-Concentrated Vortices, Model.

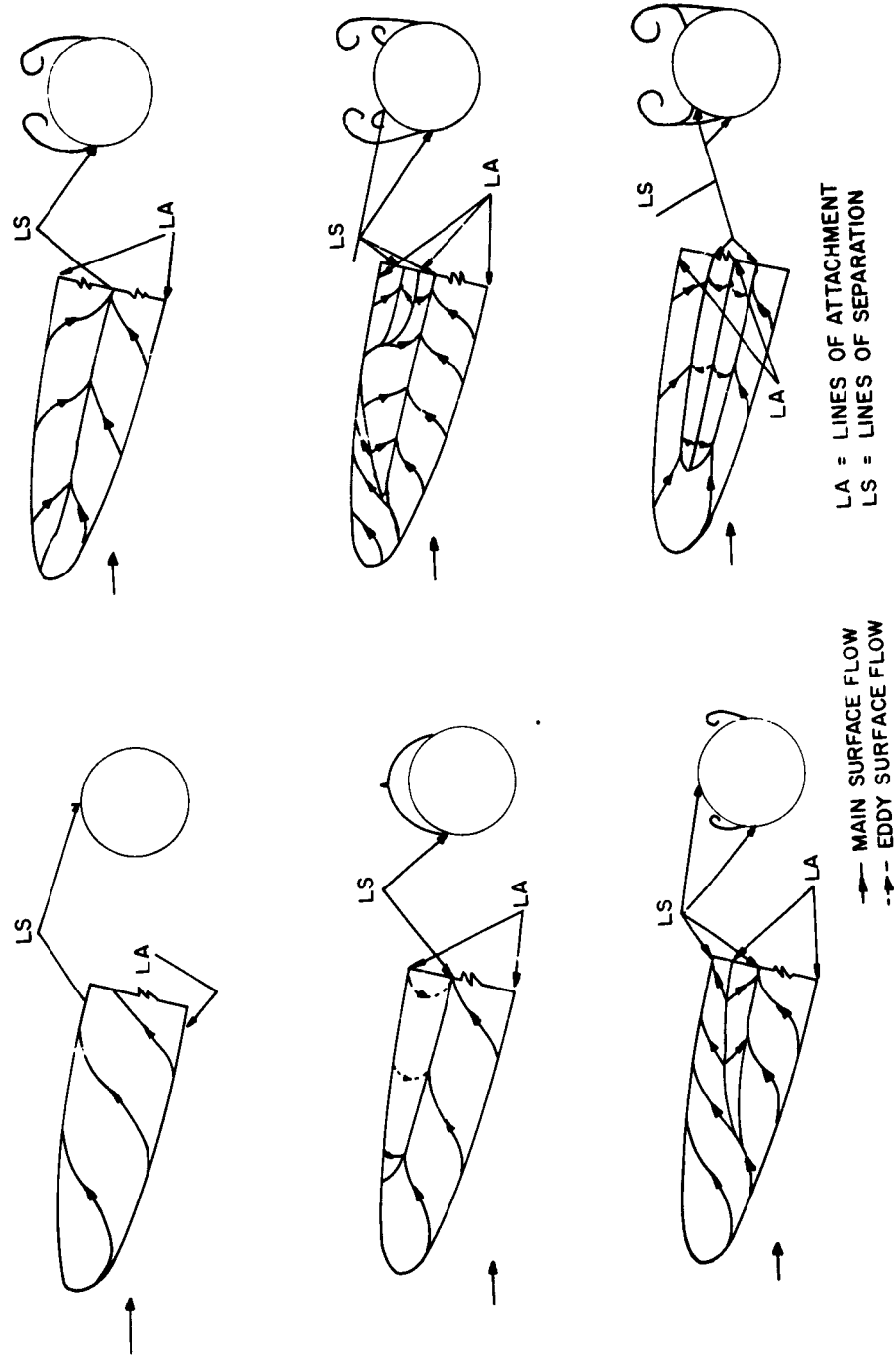


Figure 2. Maskell's Possible Surface Flows.

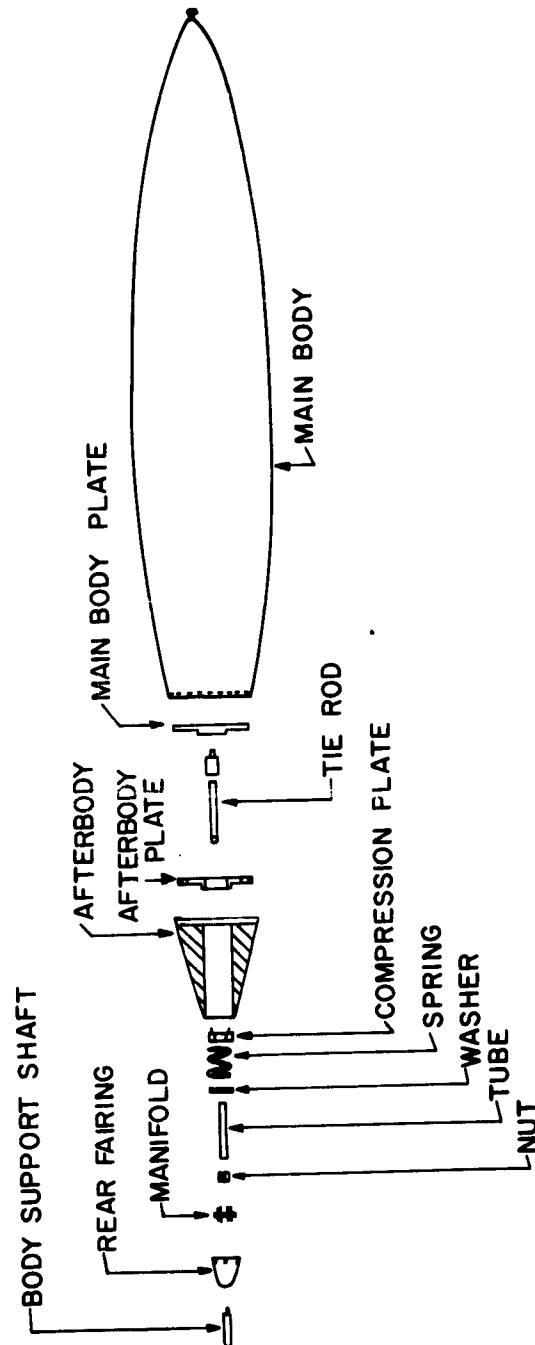


Figure 3. Main Components of Test Model.

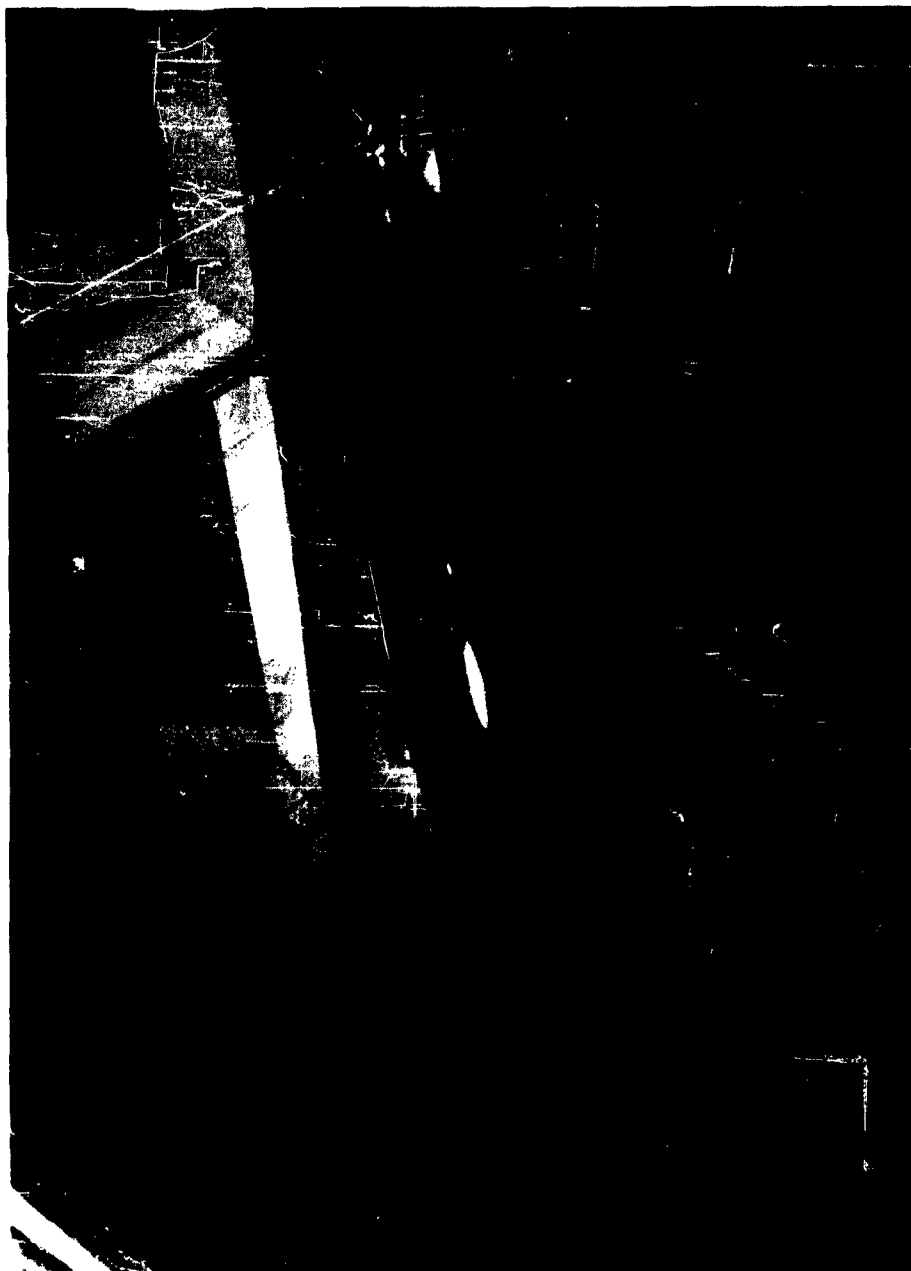


Figure 4. Wire Mounting Arrangement.

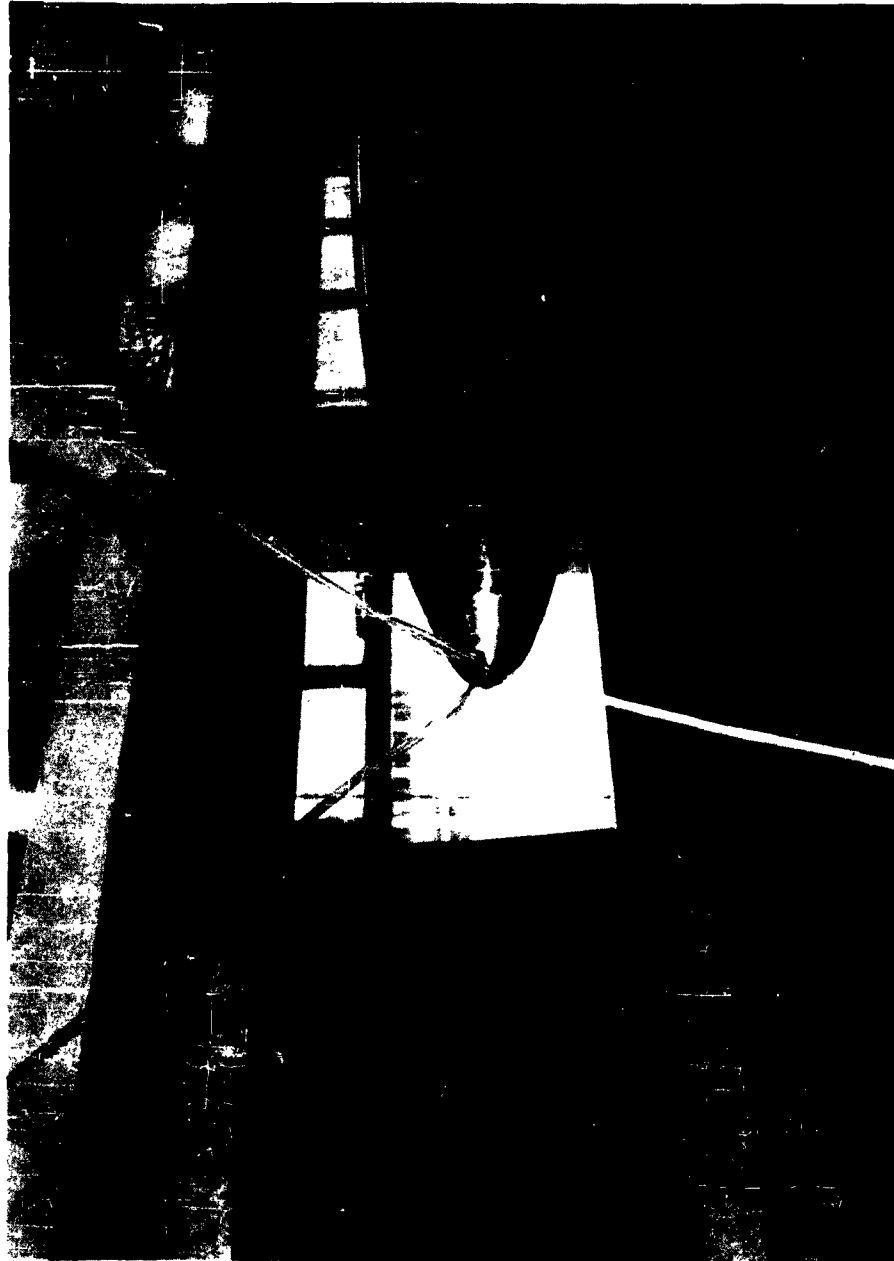


Figure 5. Pressure Tubing Arrangement Along  
Rear Support Wires.



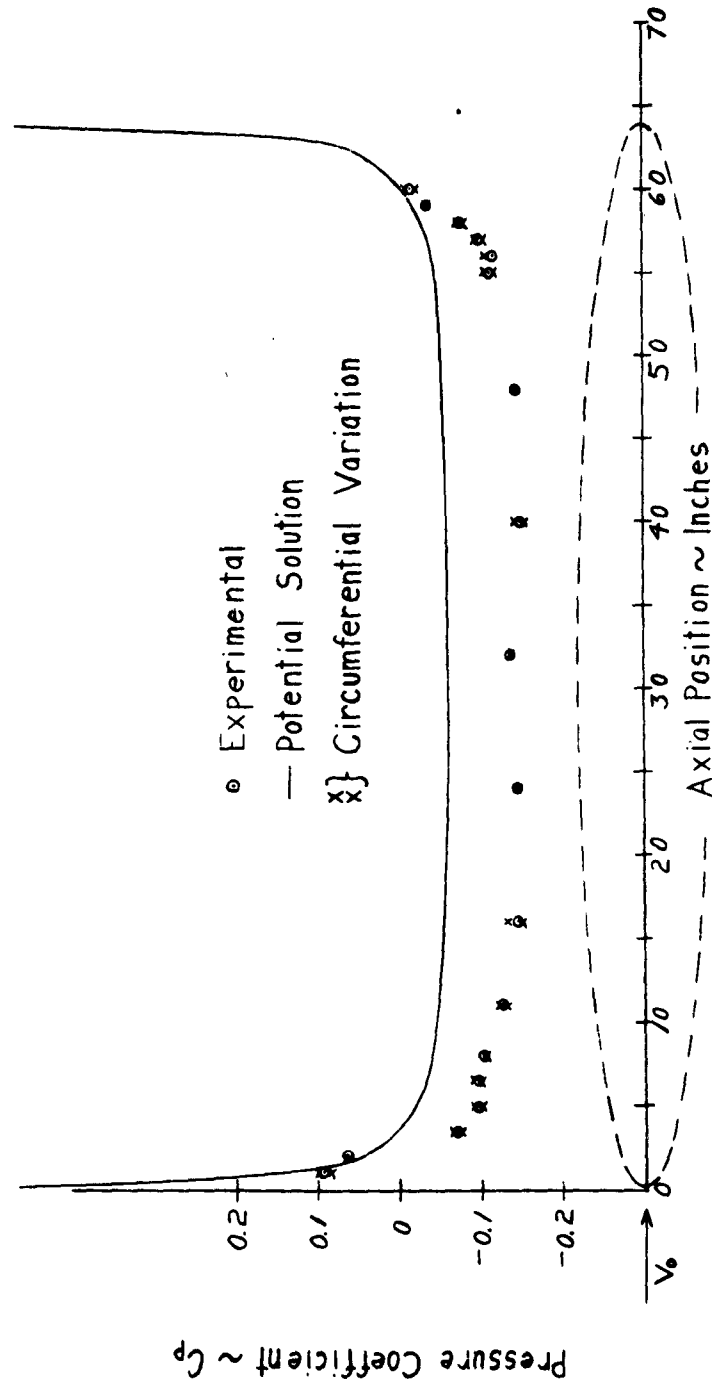


Figure 6. Axial Pressure Distribution Uncorrected for Wind Tunnel Interference. Zero Degrees Angle of Attack.

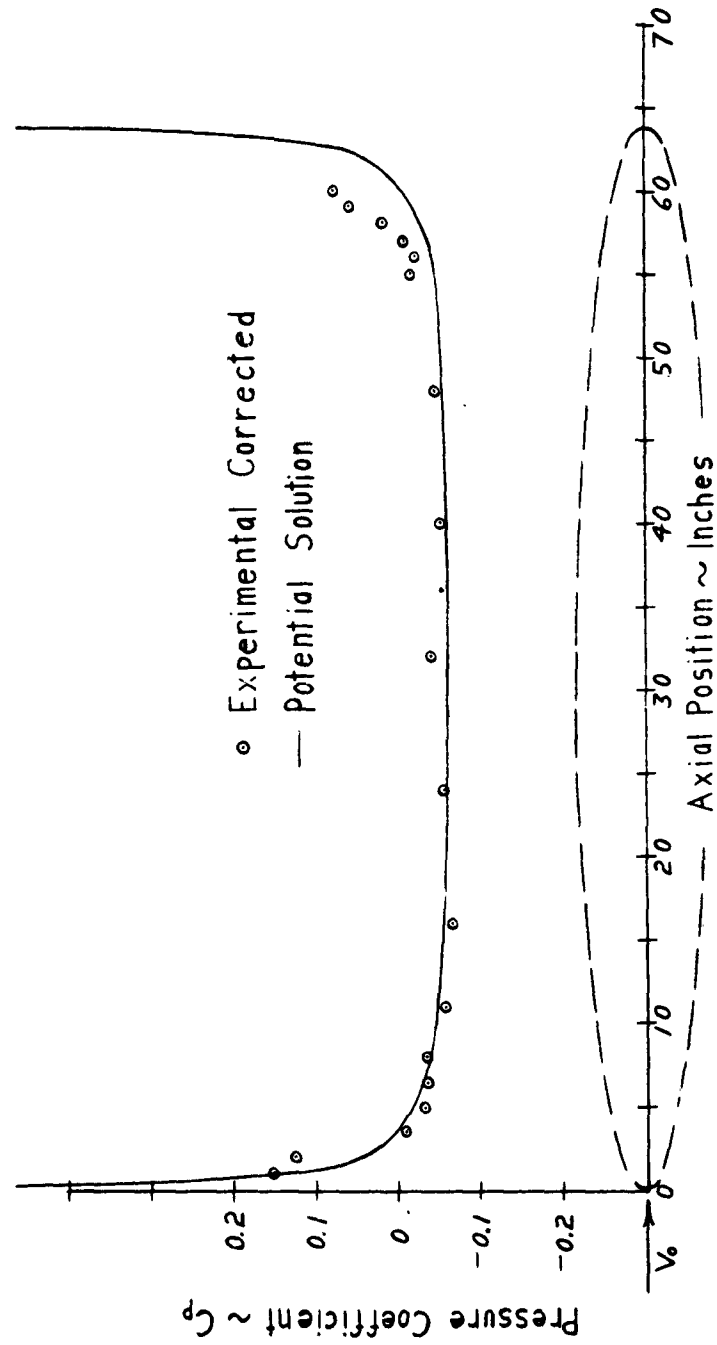


Figure 7. Axial Pressure Distribution Corrected for Wind Tunnel Interference. Zero Degrees Angle of Attack.

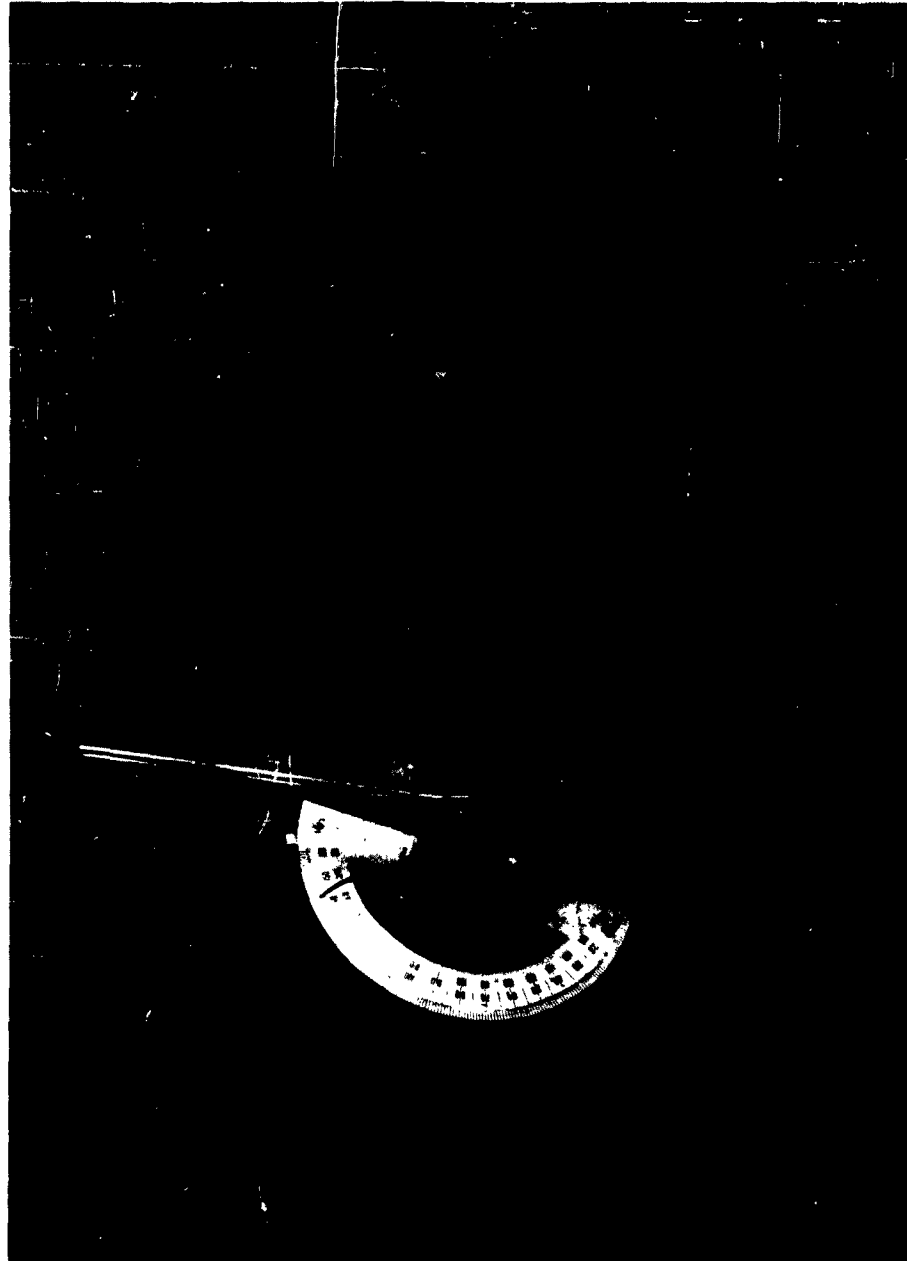


Figure 8. Sighting Scope.

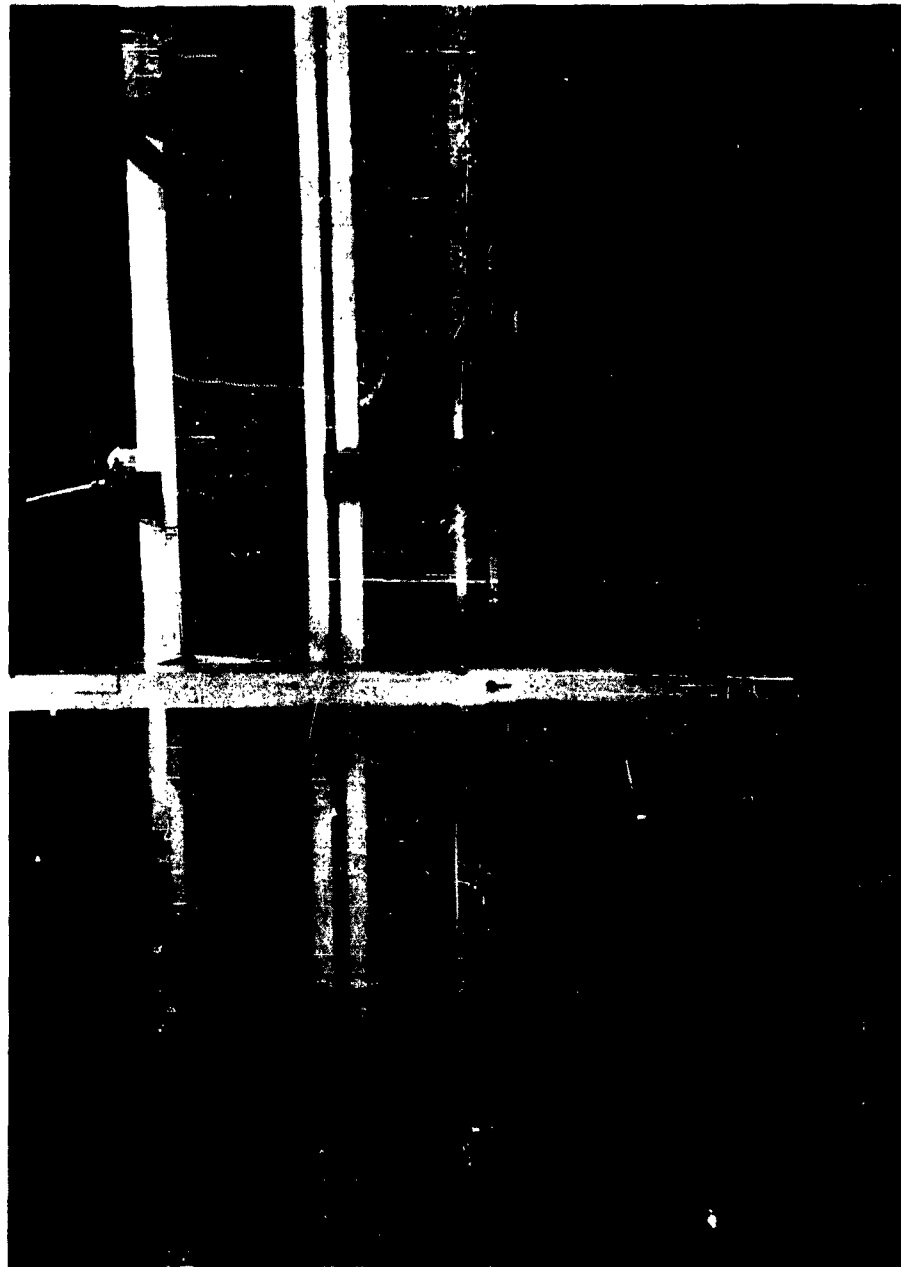
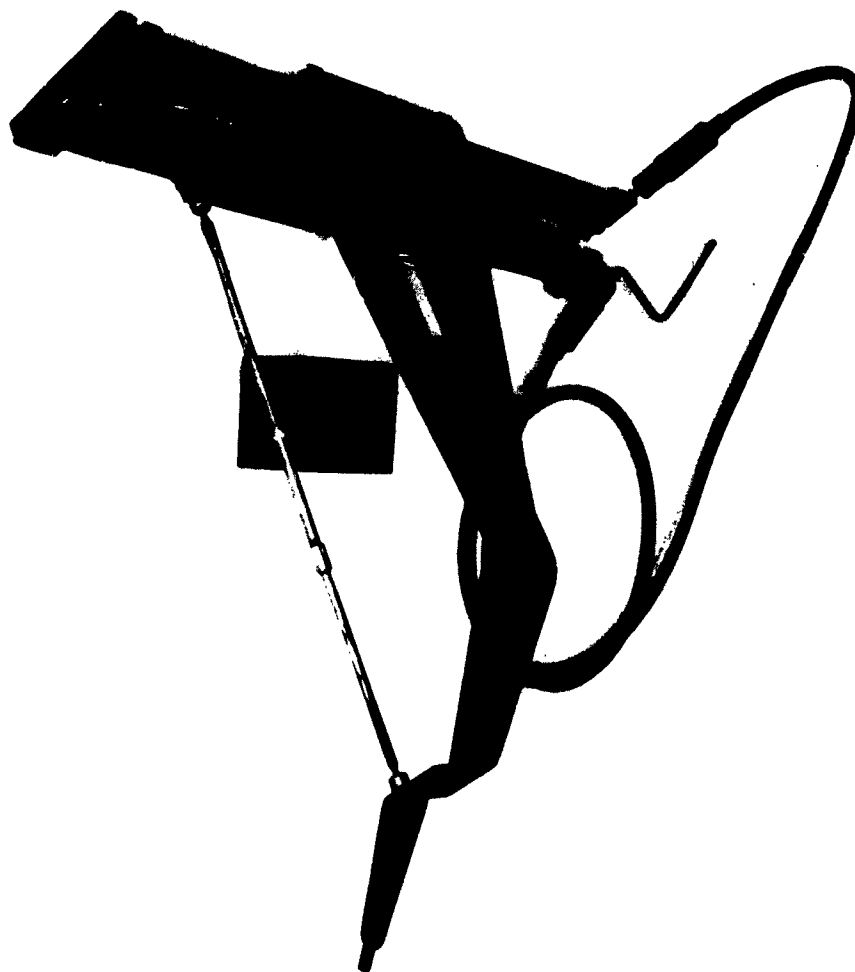


Figure 9. Scope Mounting Brackets and Arrangement on Tunnel.



Figure 10. Tuft Probe.



**Figure 11. Probe Traversing Mechanism.**

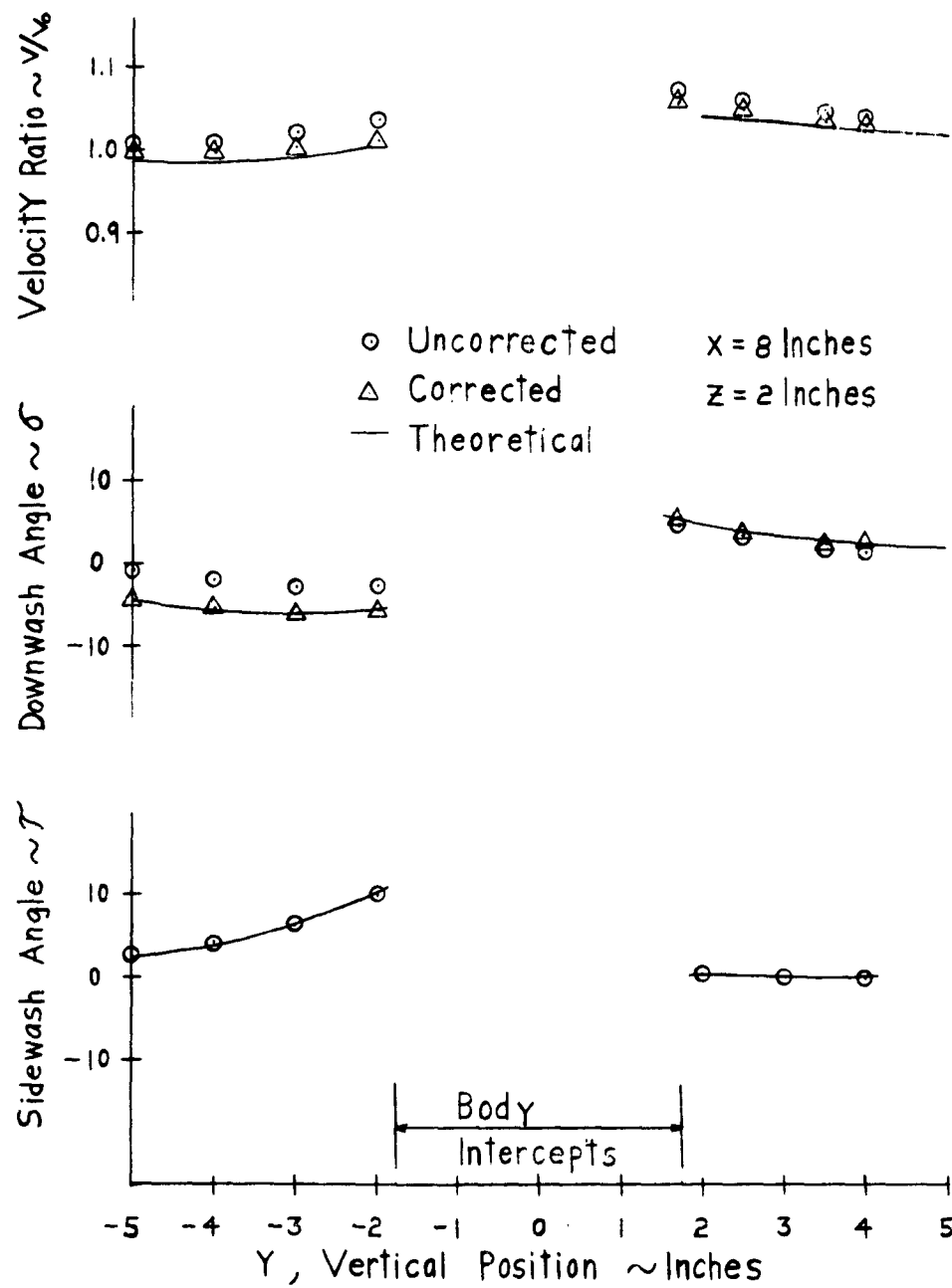


Figure 12. Typical Plots of Velocity Ratio, Downwash Angle, and Sidewash Angle at a Forward Location.

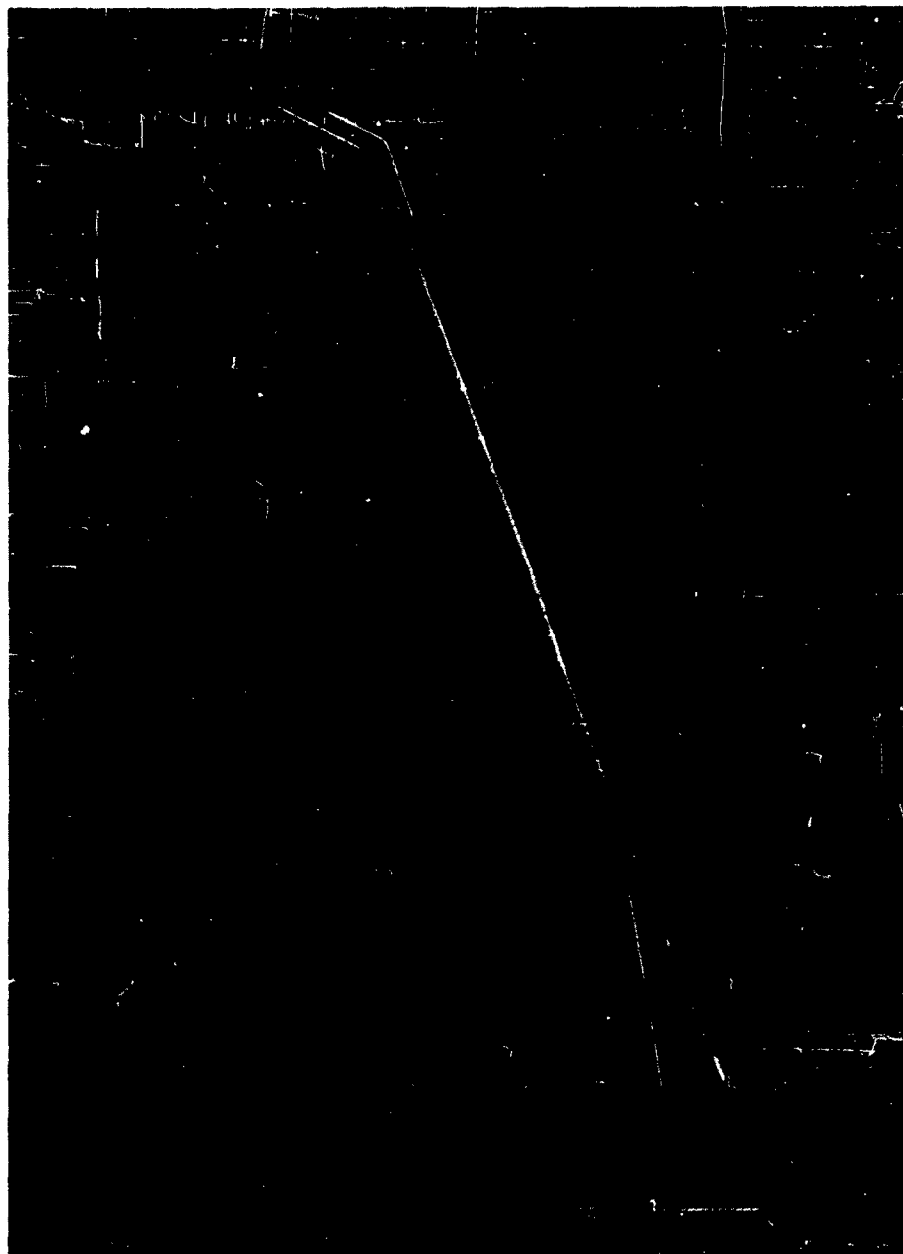


Figure 13. Velocity Rake.



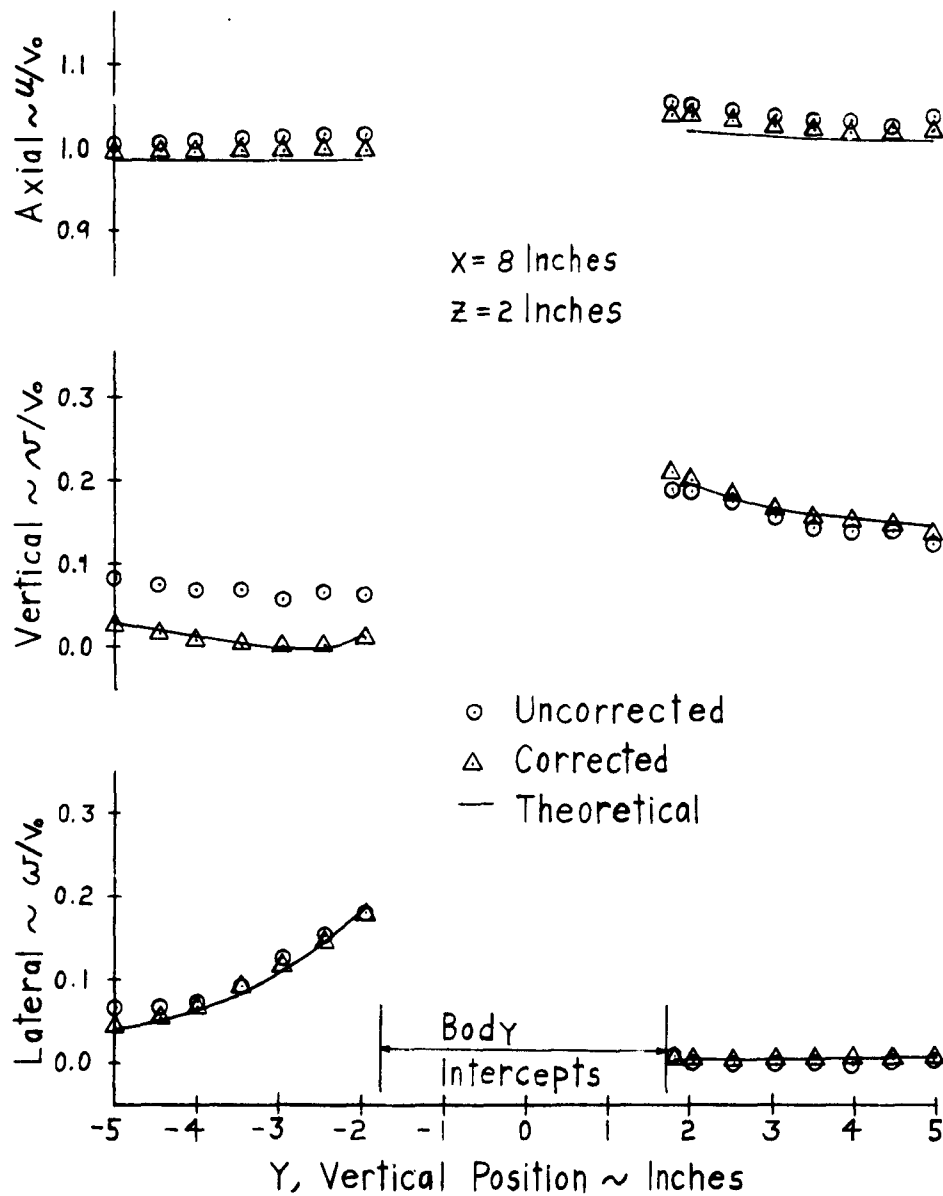


Figure 14. Typical Plots of the Velocity Components at a Forward Location.

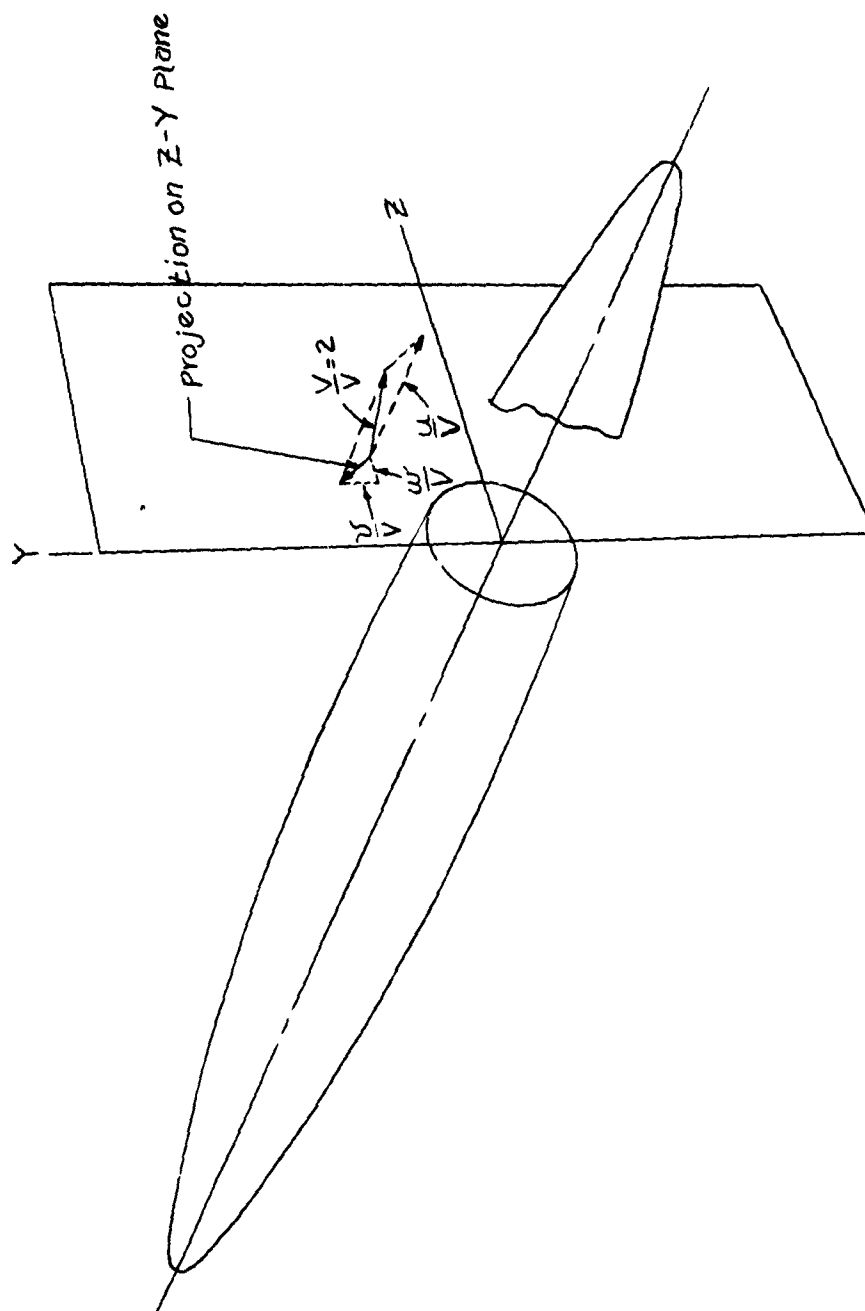


Figure 15. Interpretation of the Equivalent  
Tuft pictures.

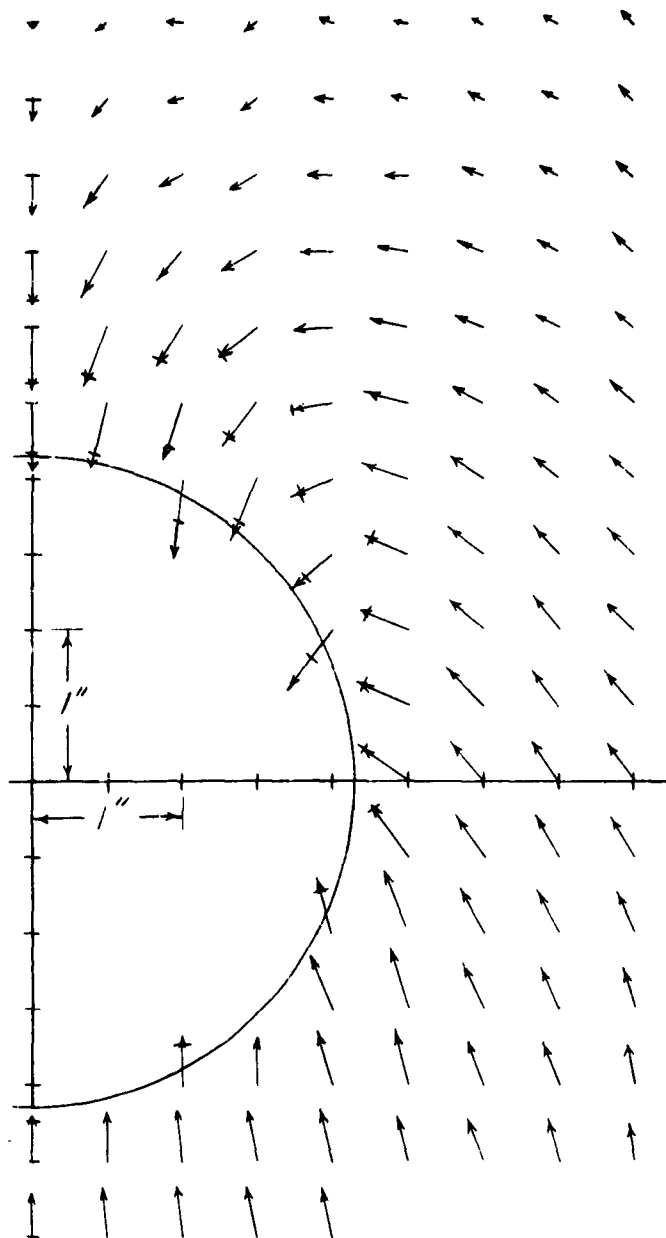


Figure 16. Equivalent Tuft Picture for the Total Flow. 59 Inches From the Nose of the Model.

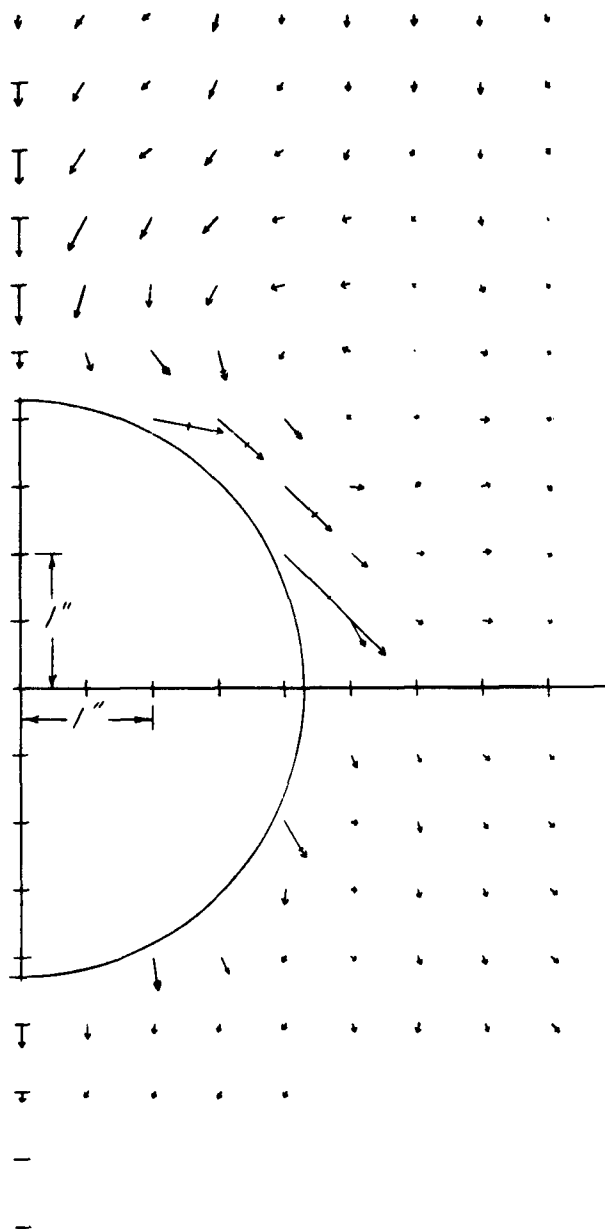


Figure 17. Equivalent Tuft Picture for the Viscous Part of the Flow. 59 Inches From the Nose of the Model.

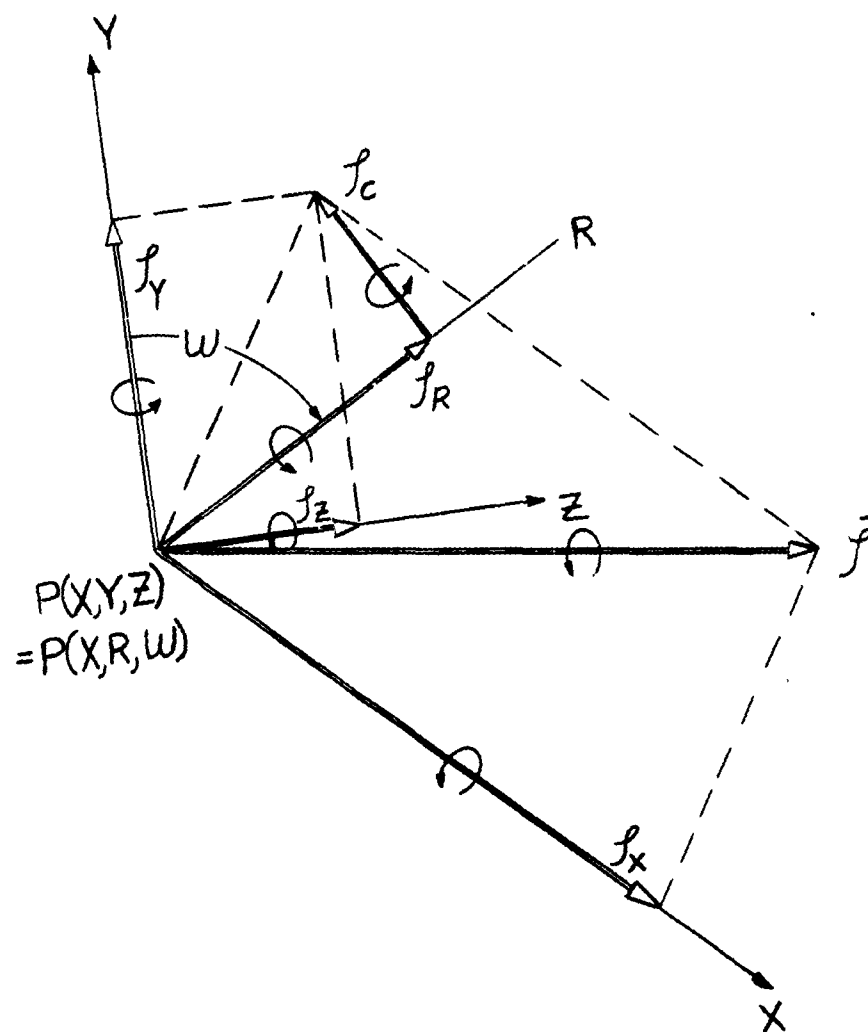


Figure 18. Vorticity Components.

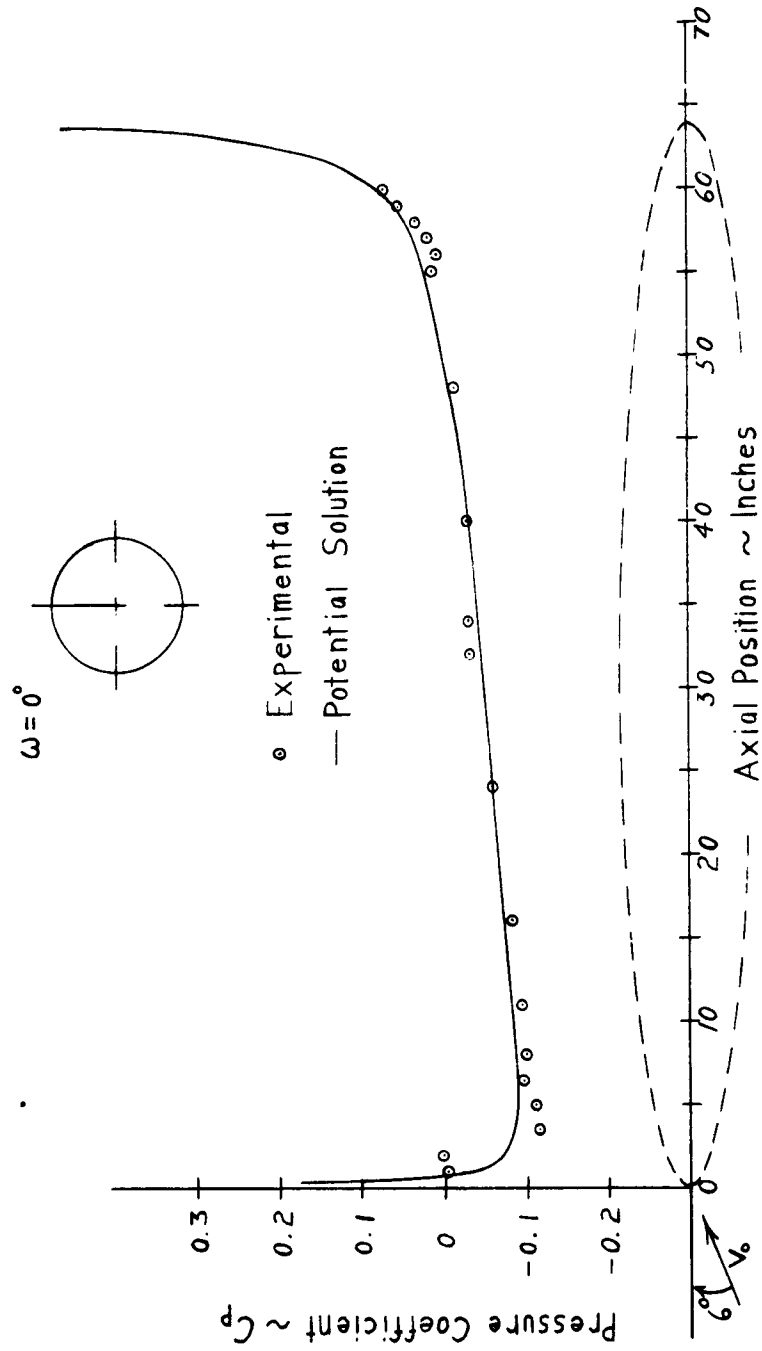


Figure 19a. Pressure Distribution Along the Top Meridian.

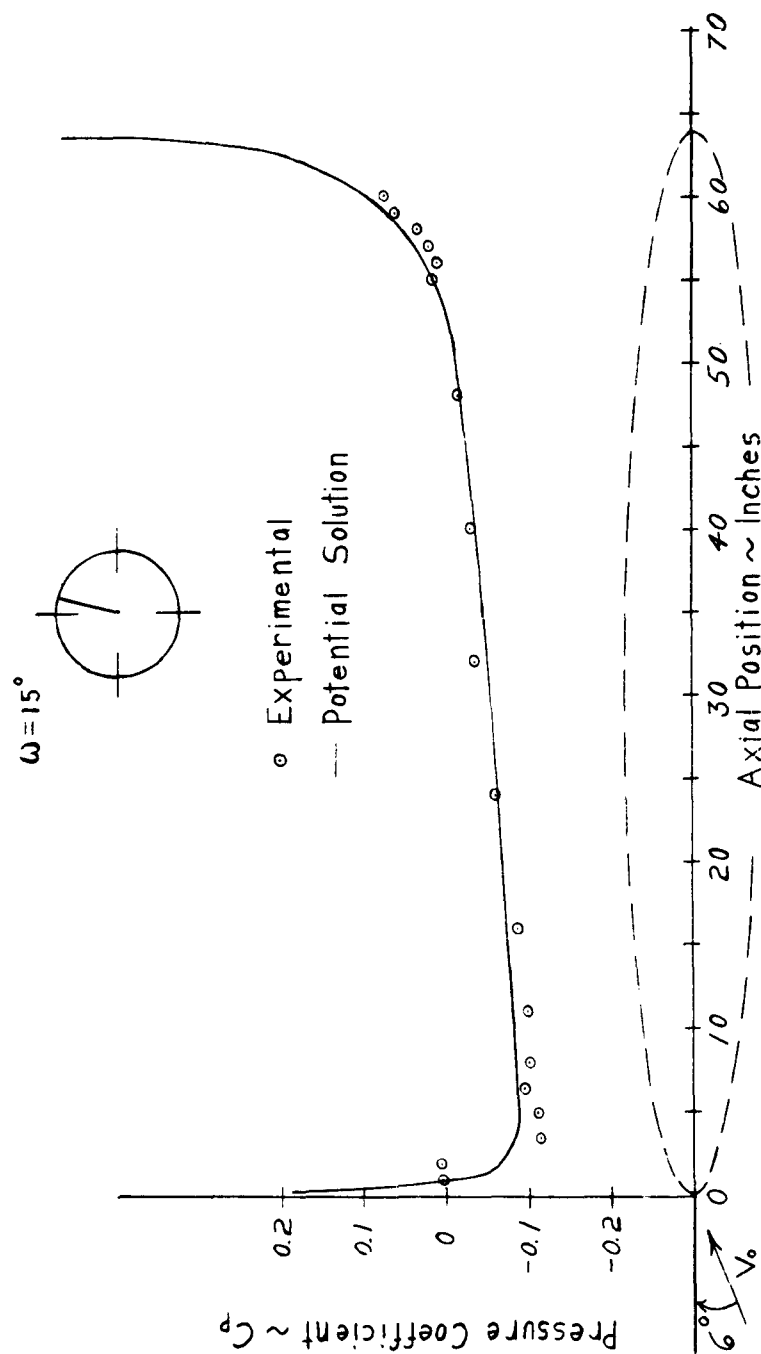


Figure 19b. Pressure Distribution Along the 15 Degree Meridian.

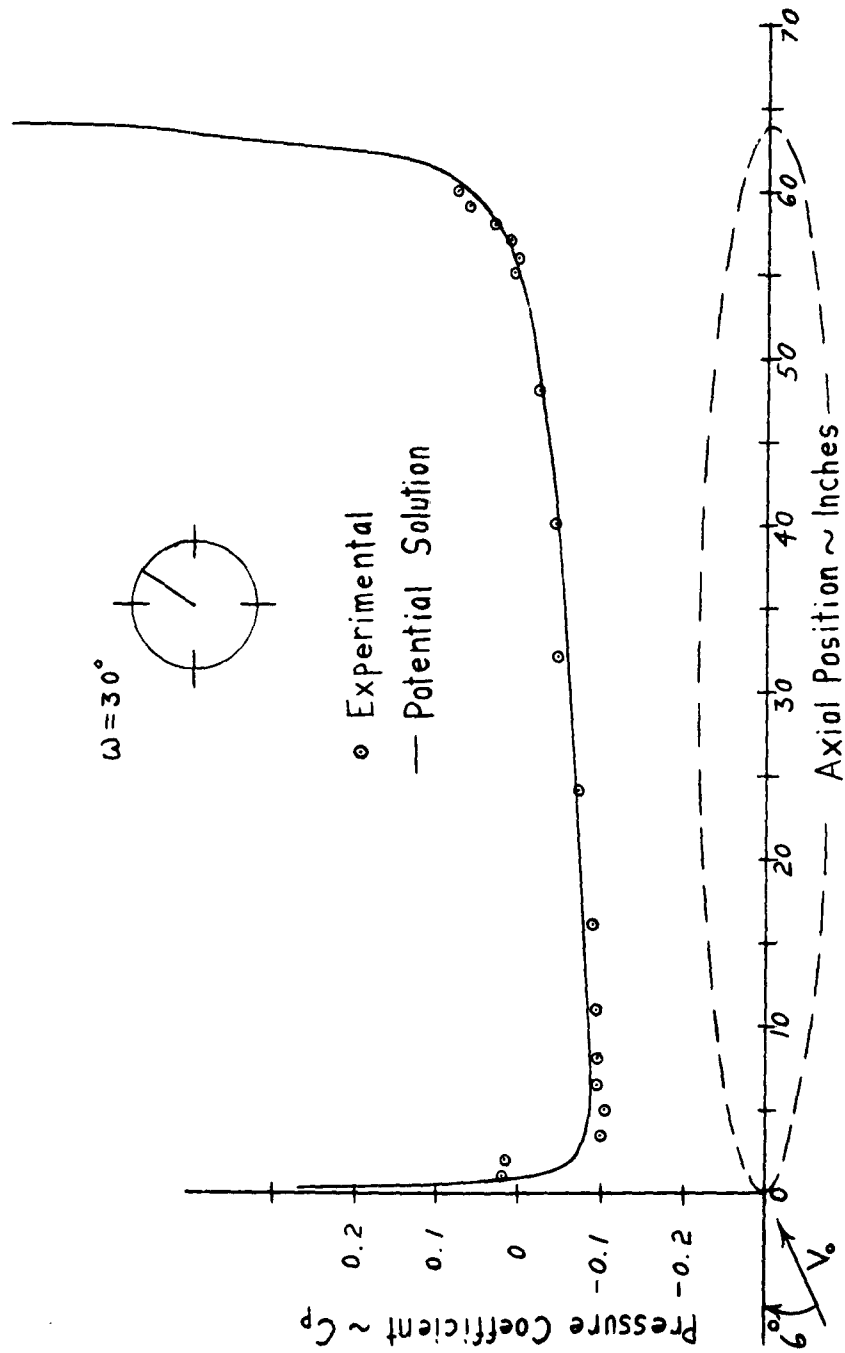


Figure 19c. Pressure Distribution Along the 30 Degree Meridian.



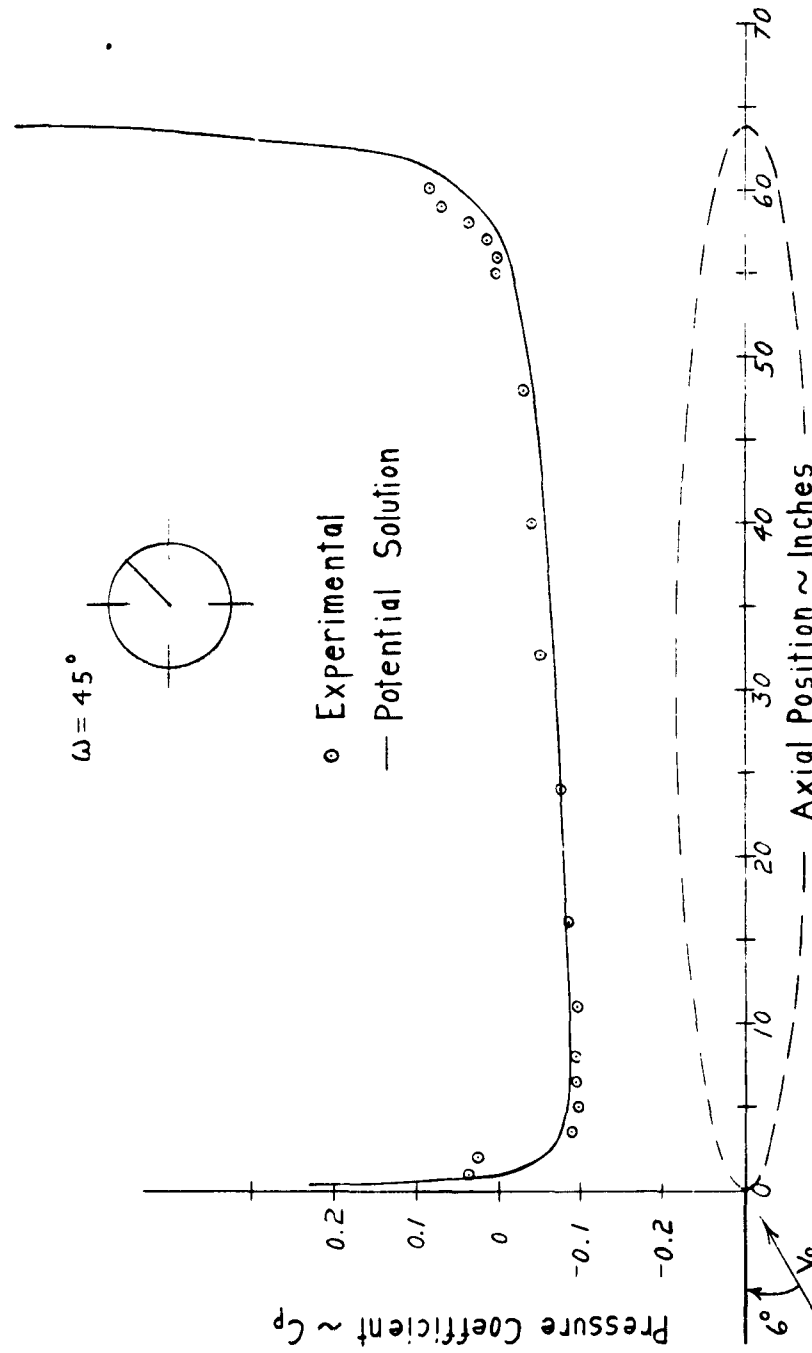


Figure 19d. Pressure Distribution Along the 45 Degree Meridian.

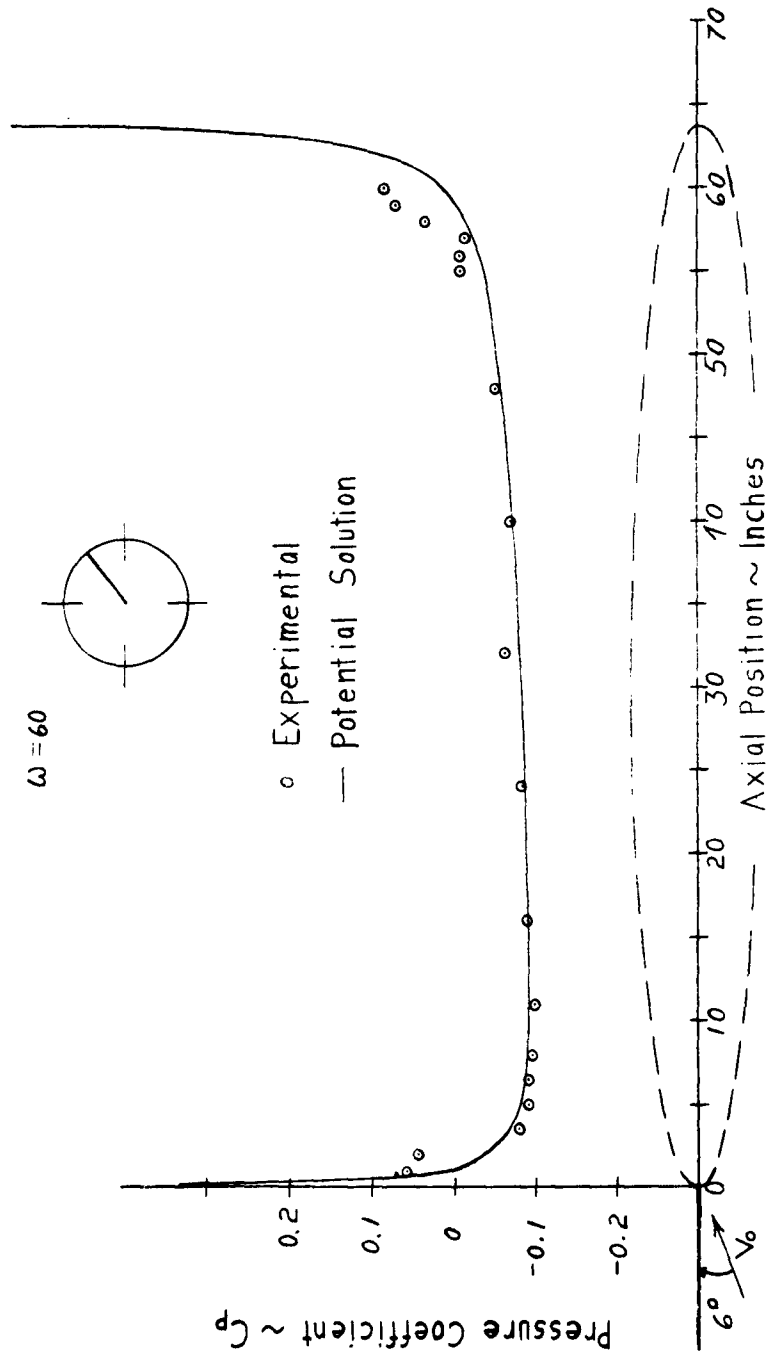


Figure 19e. Pressure Distribution Along the 60 Degree Meridian.

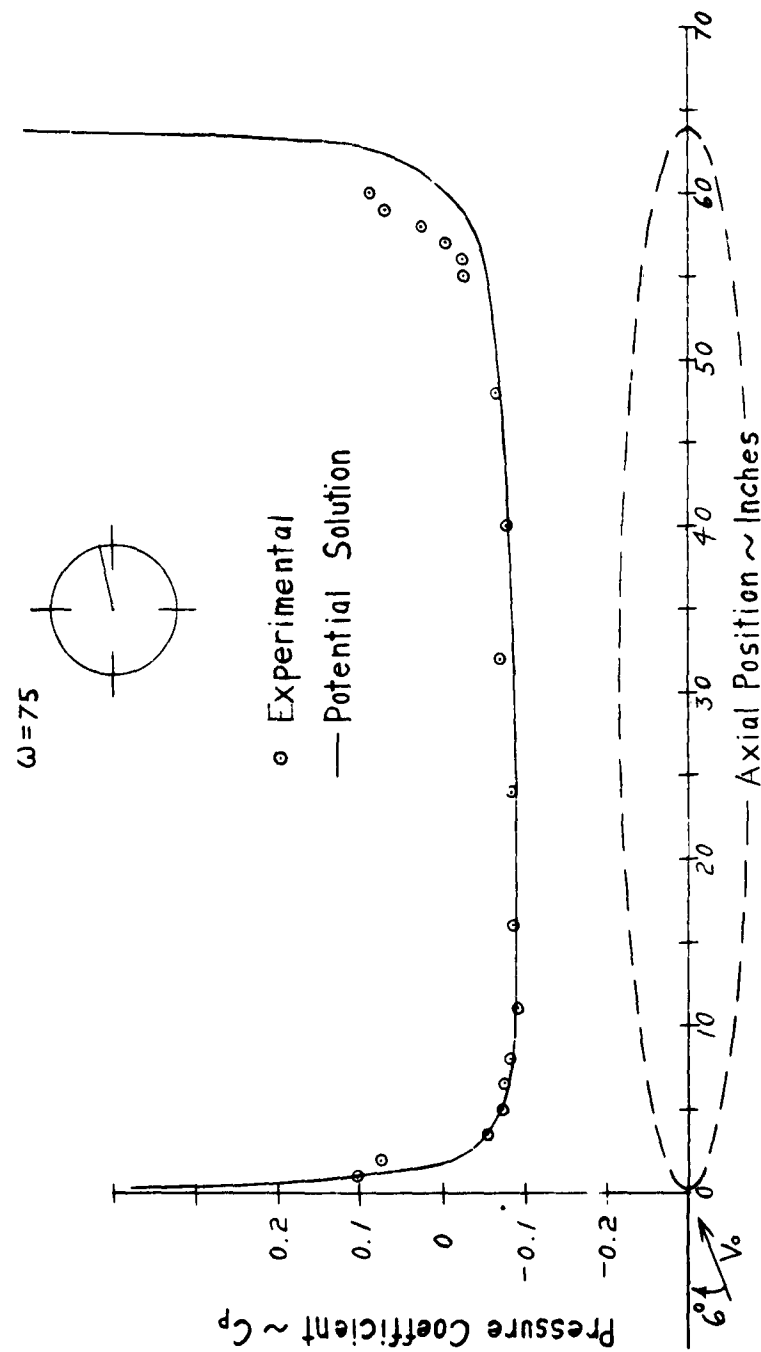


Figure 19f. Pressure Distribution Along the 75 Degree Meridian.

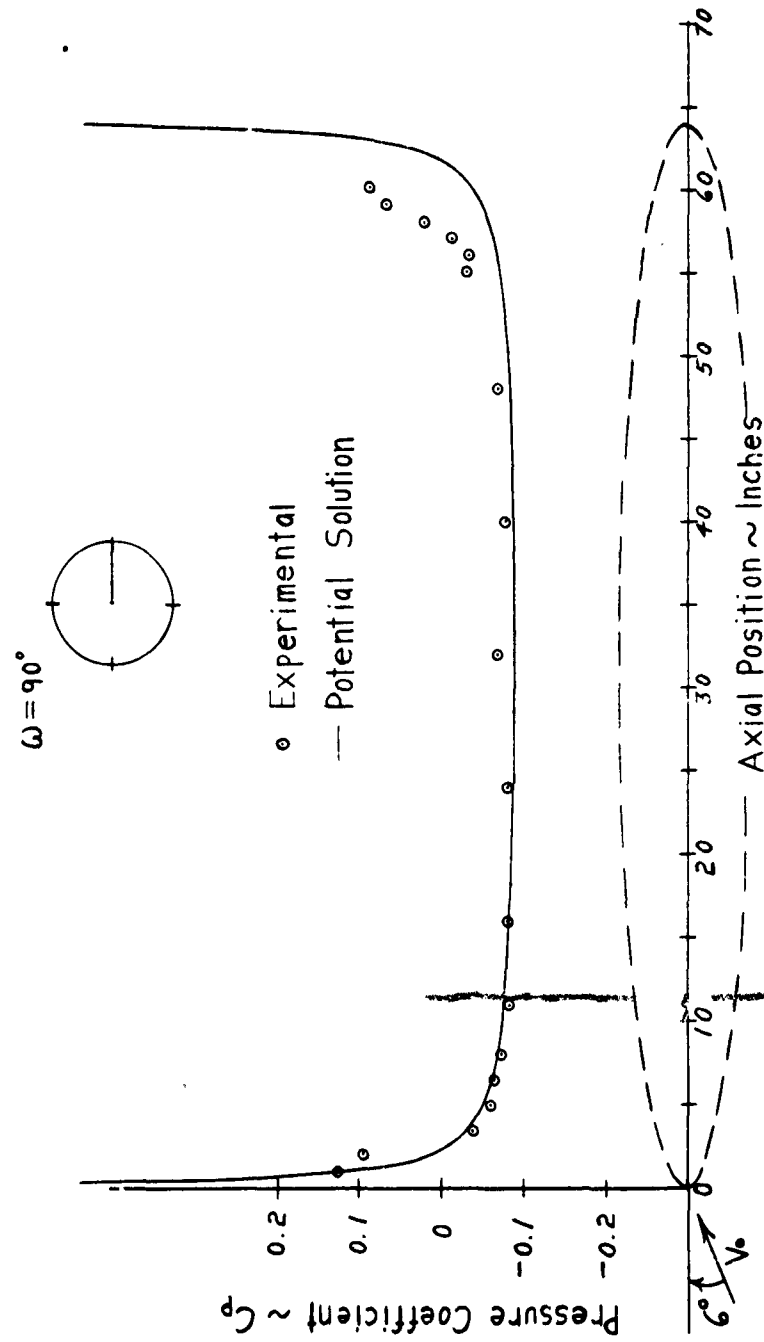


Figure 19g. Pressure Distribution Along the 90 Degree Meridian.

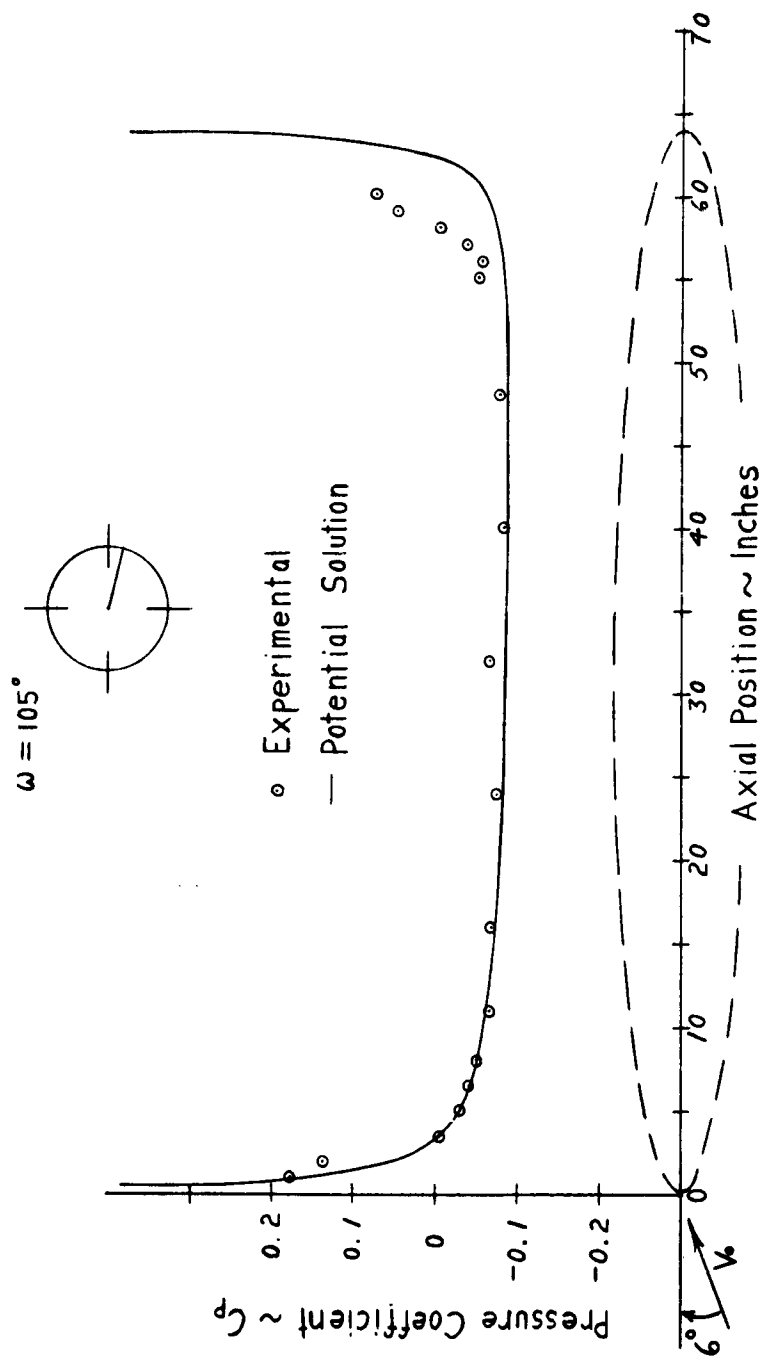


Figure 19h. Pressure Distribution Along the 105 Degree Meridian.

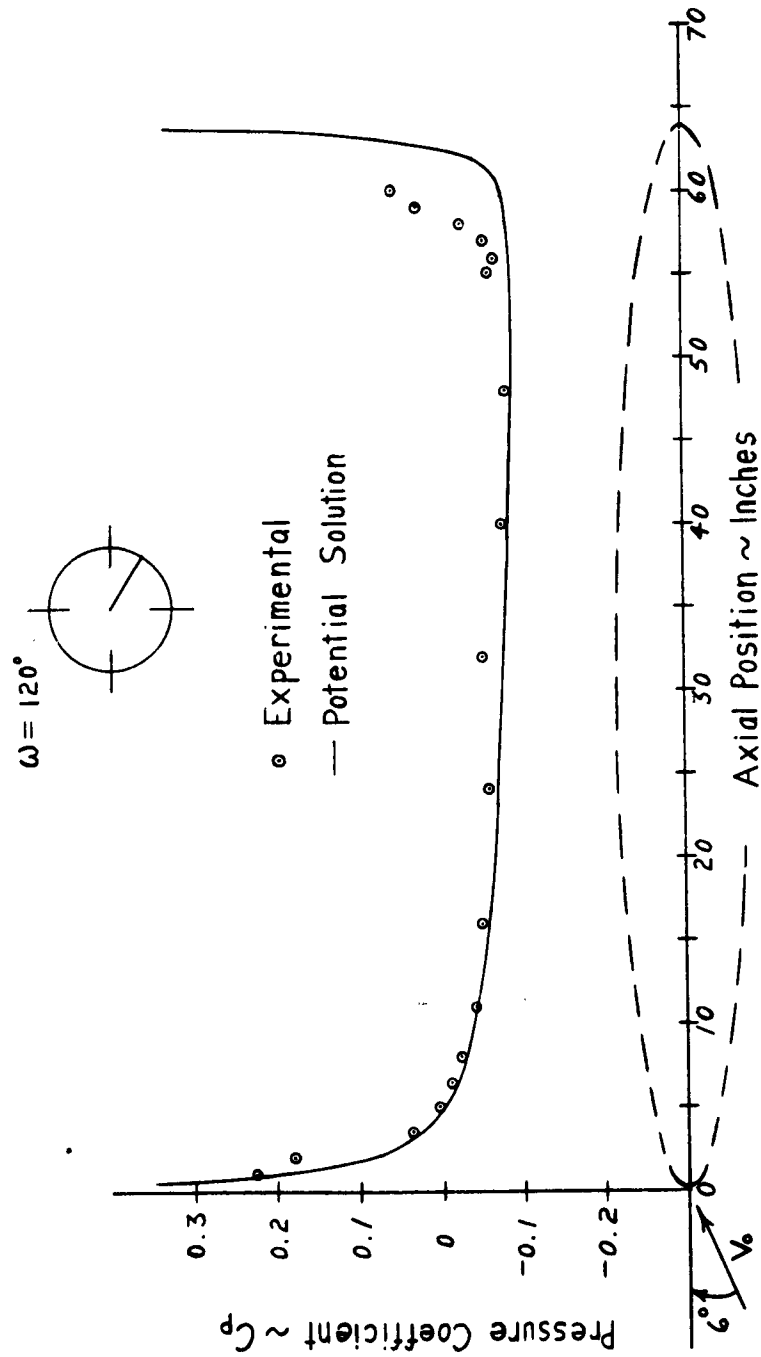


Figure 191. Pressure Distribution Along the 120 Degree Meridian.

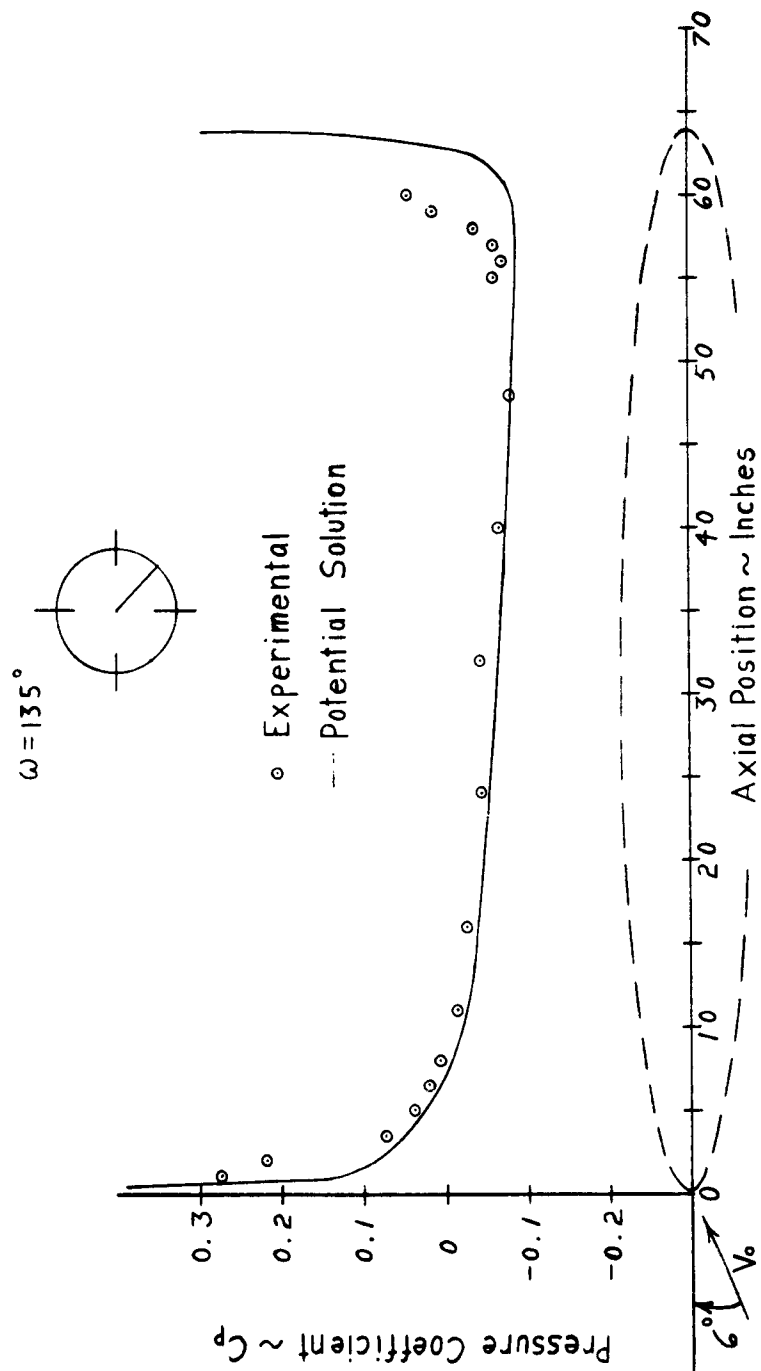


Figure 19j. Pressure Distribution Along the 135 Degree Meridian.

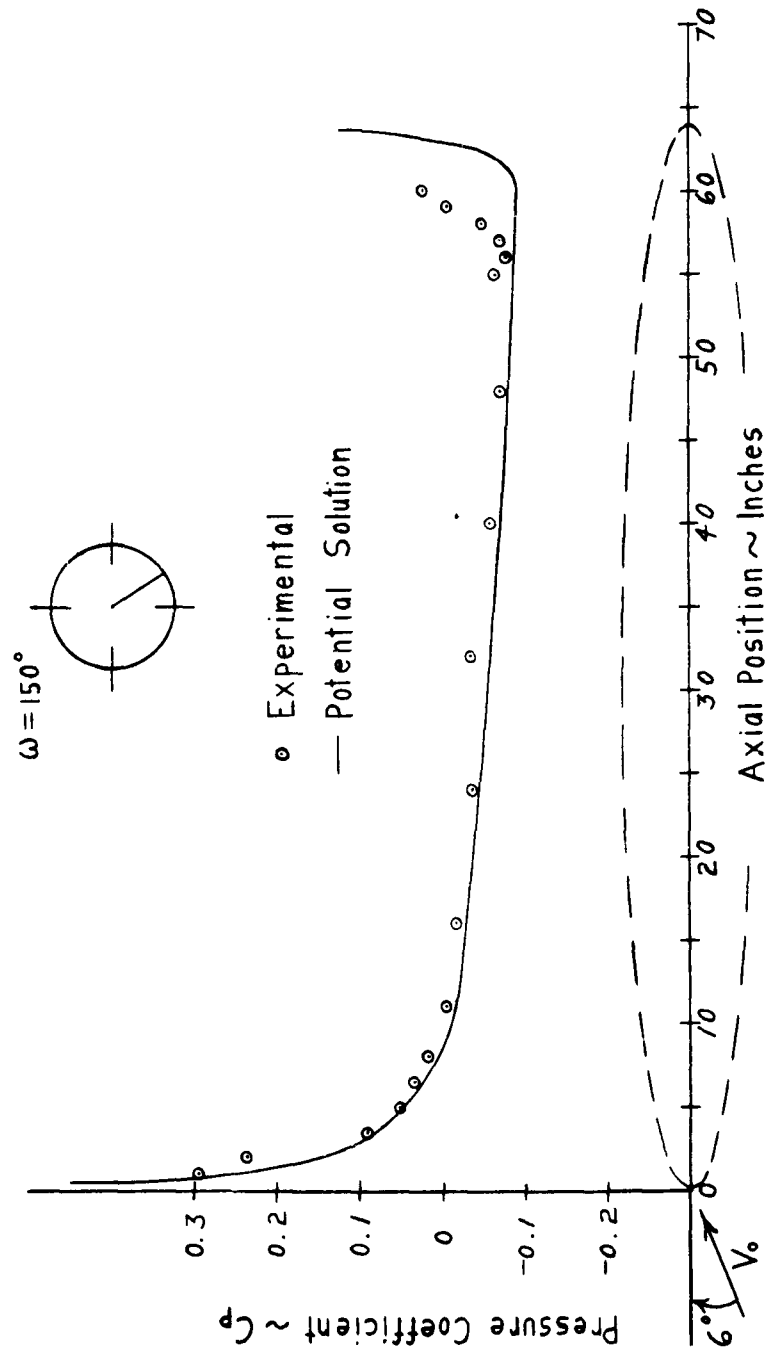


Figure 19k. Pressure Distribution Along the 150 Degree Meridian.



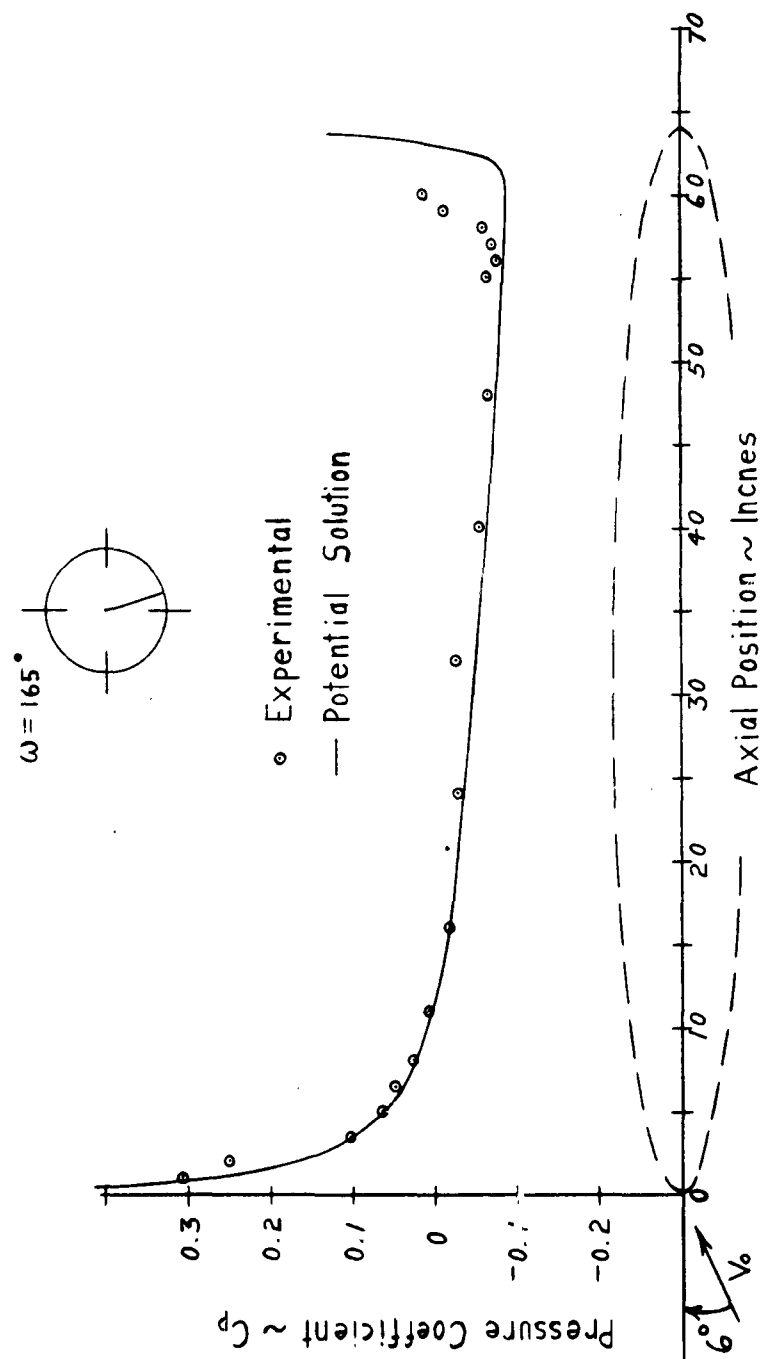


Figure 191. Pressure Distribution Along the 165 Degree Meridian.

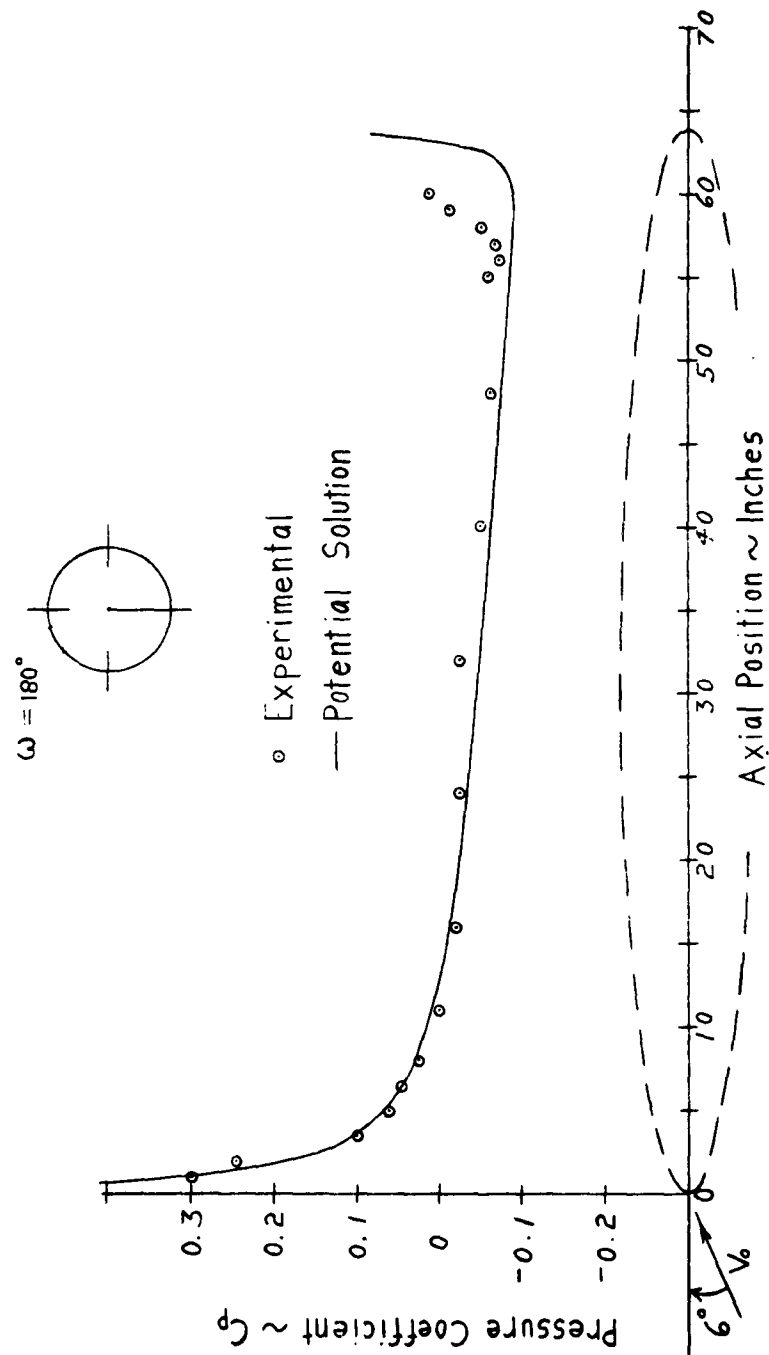


Figure 19m. Pressure Distribution Along the Bottom Meridian.

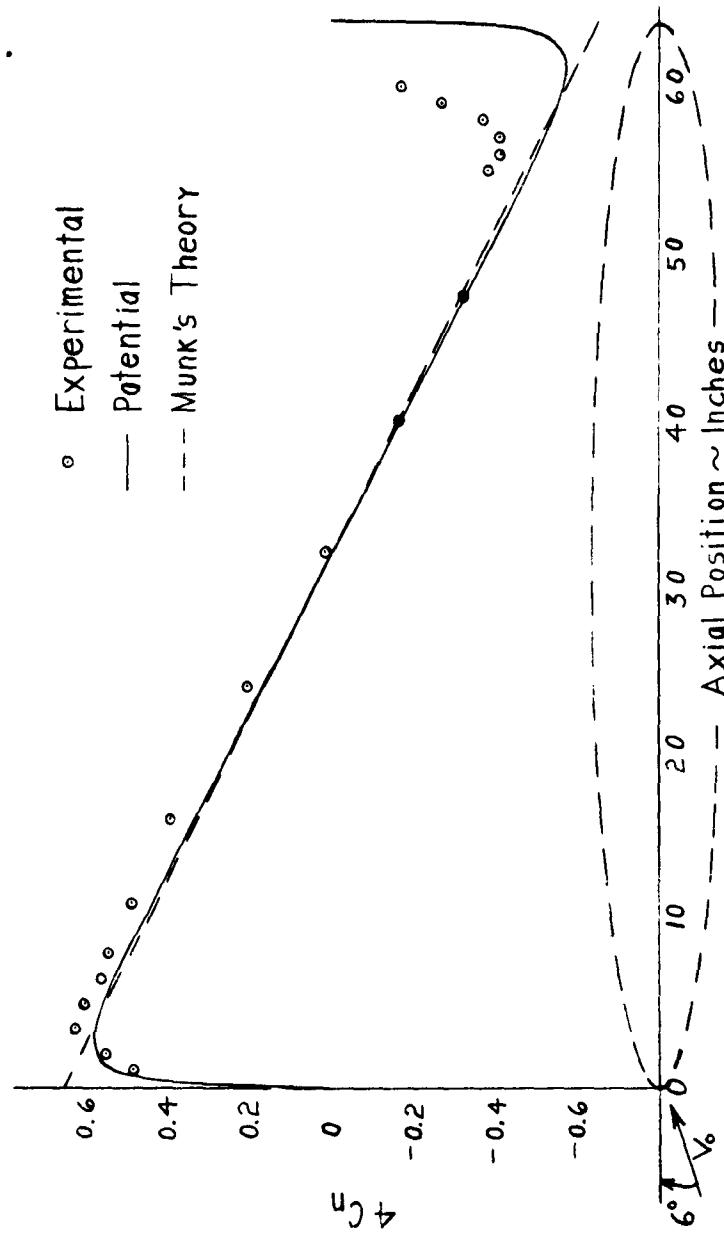


Figure 20. Normal Force Distribution.

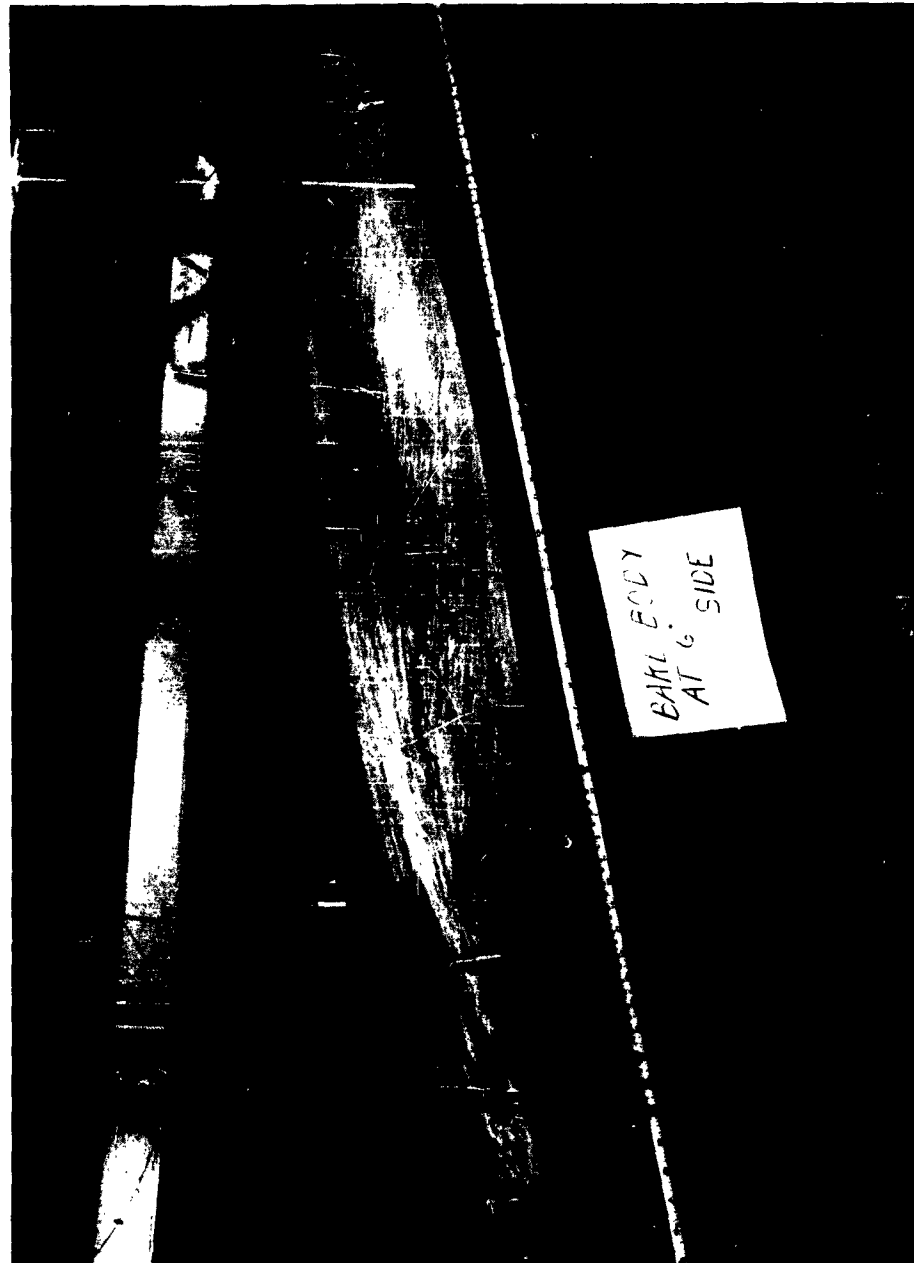


Figure 21a. Surface Flow. Side View.

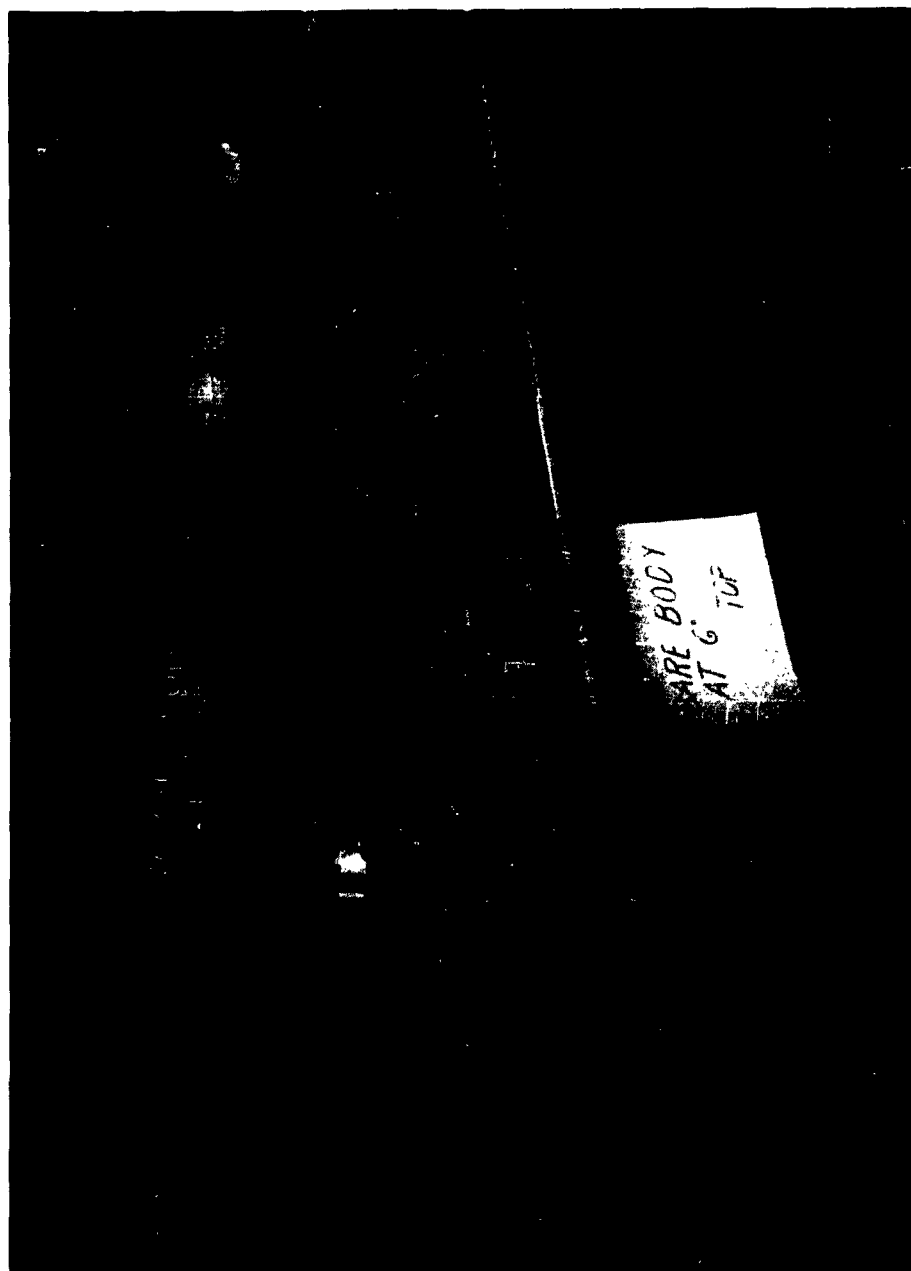
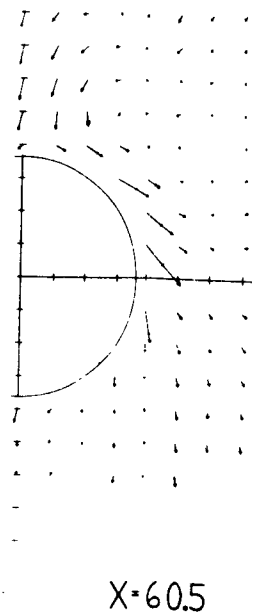
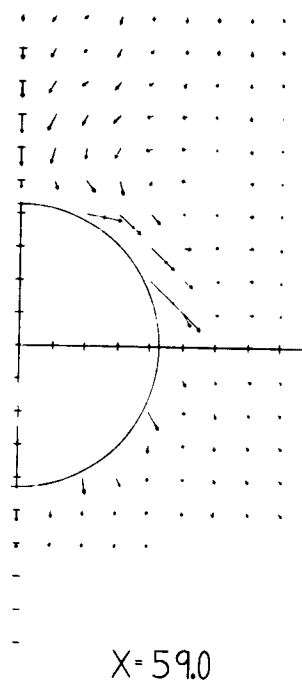
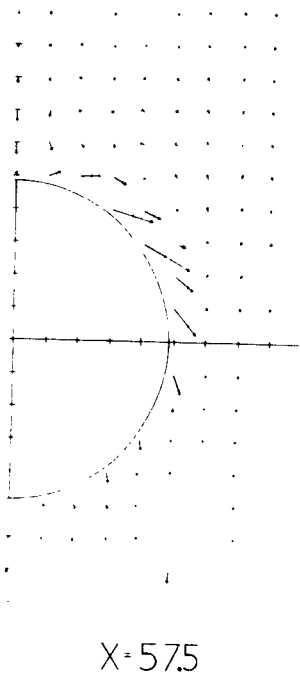
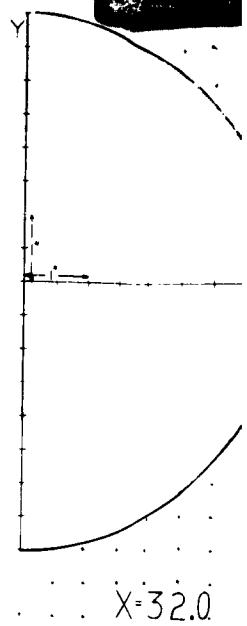
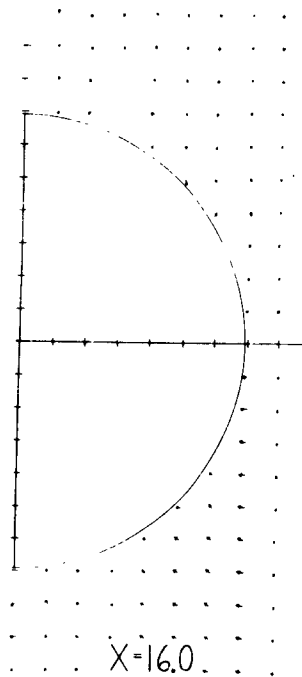
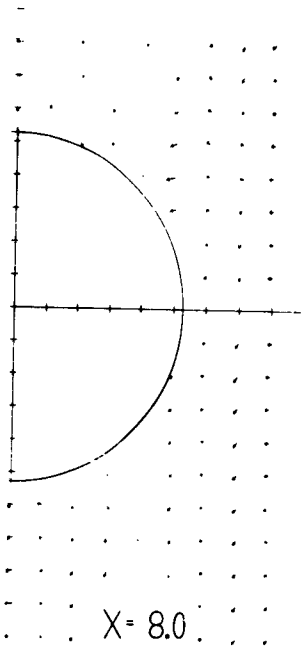


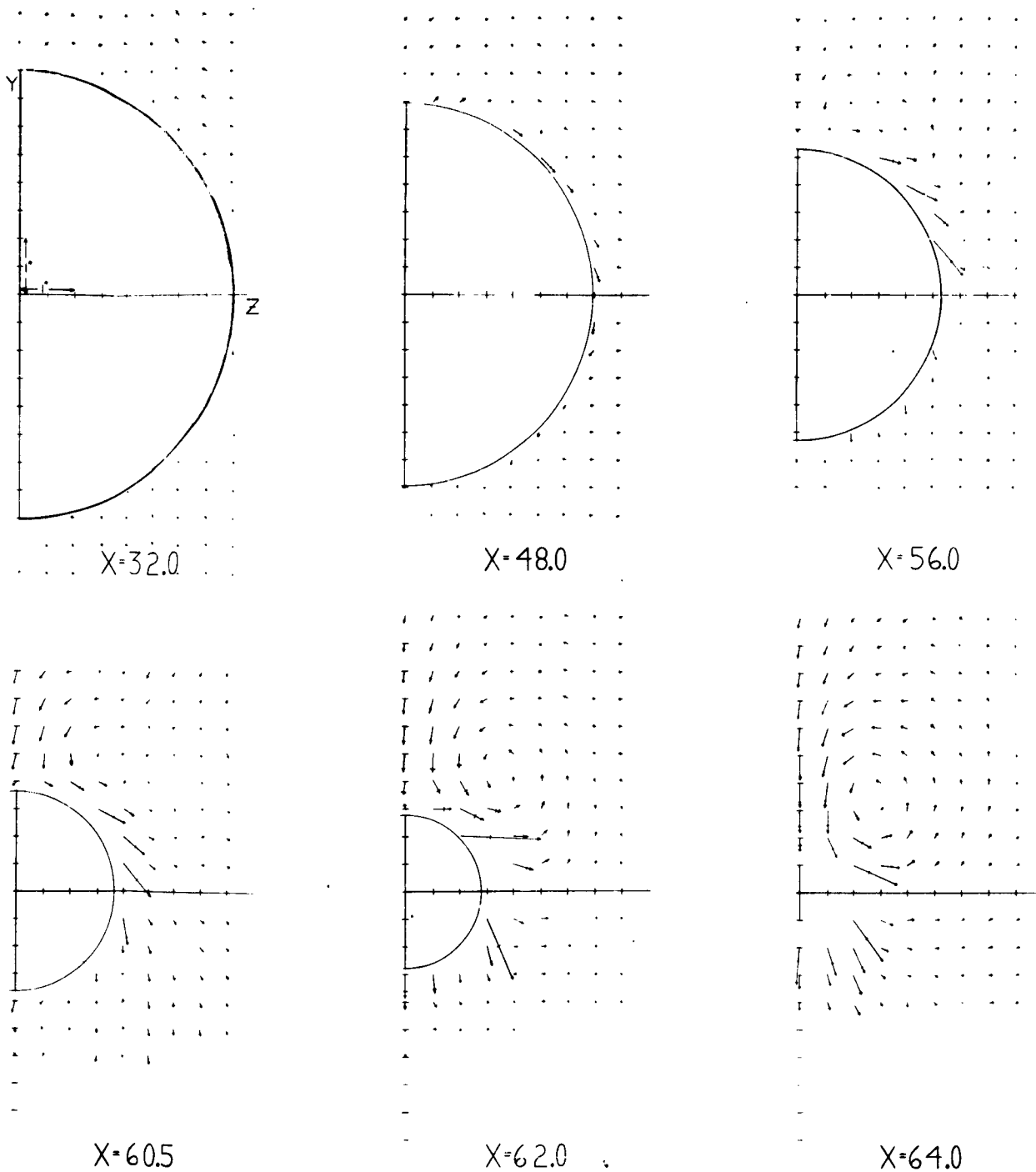
Figure 21b. Surface Flow. Top View.



Figure 21c. Surface Flow. Bottom View.

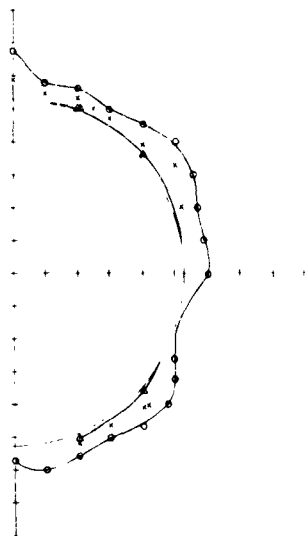


**Figure 22. Equivalent Turbulent Viscous Part of Flow, at Positions.**

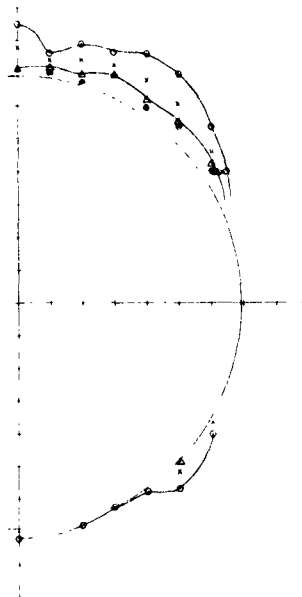


**Figure 22. Equivalent Tuft Pictures, for Viscous Part of Flow, at Various Axial Positions.**

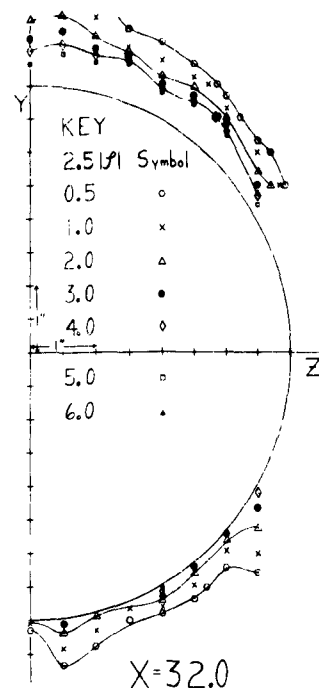




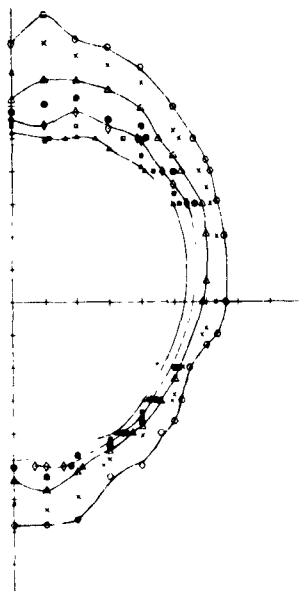
X=8.0



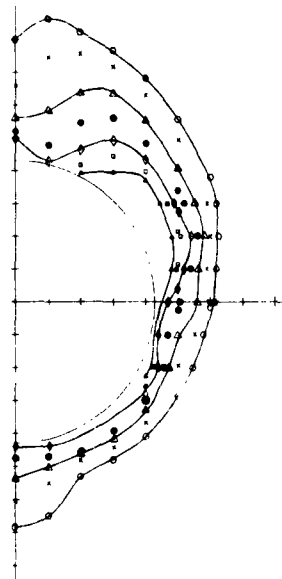
X=16.0



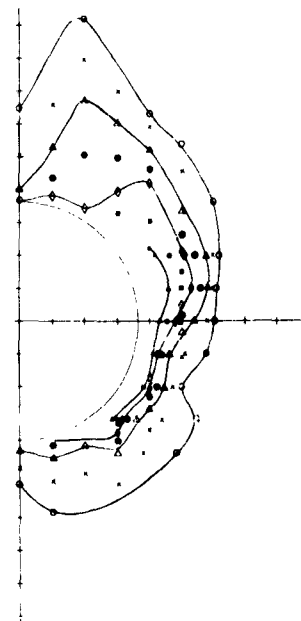
X=32.0



X=57.5

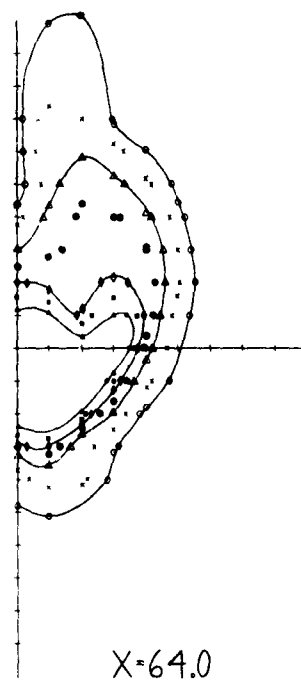
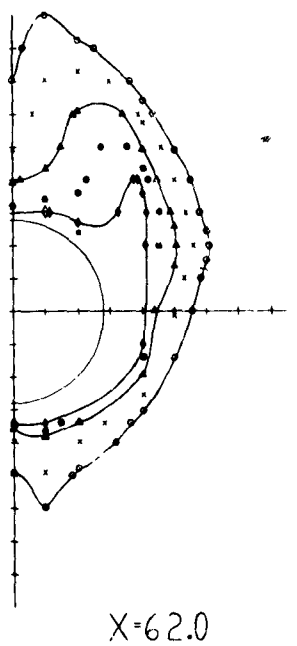
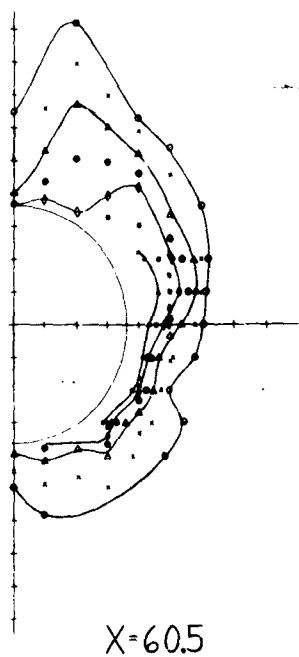
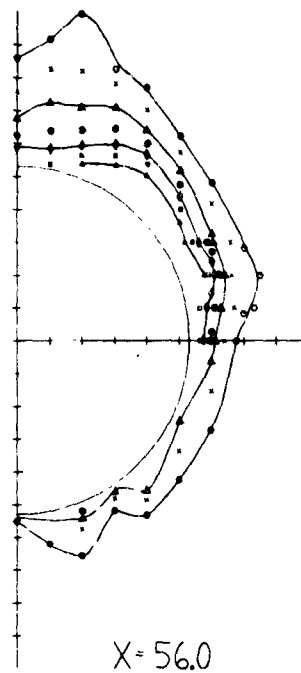
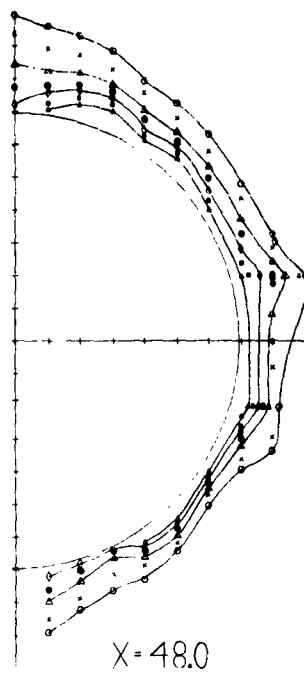
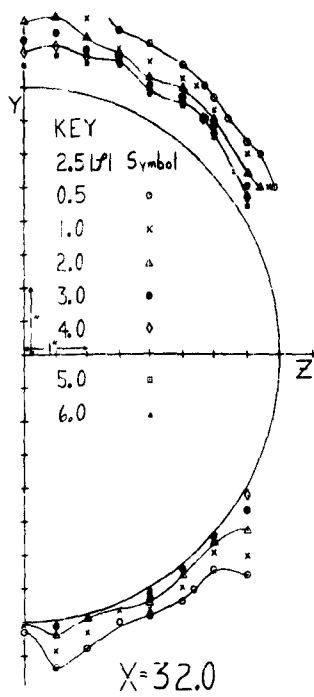


X=59.0

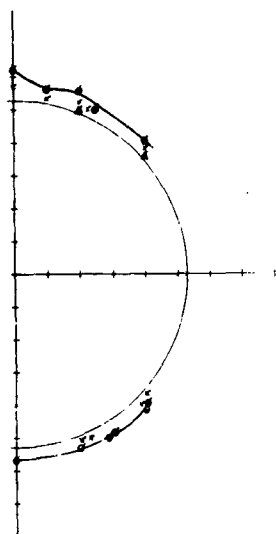


X=60.5

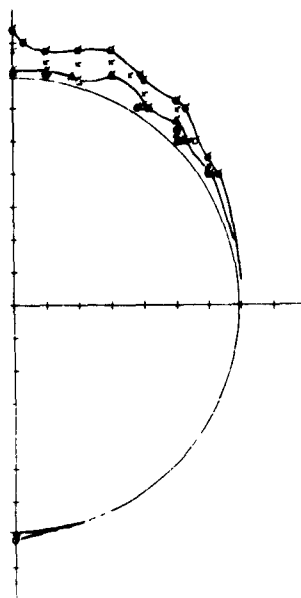
**Figure 23. Total Vorticity at Various Axial Positions.**



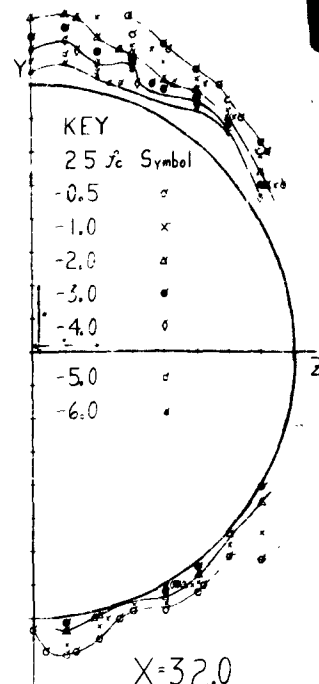
ure 23. Total Vorticity at Various Axial Positions.



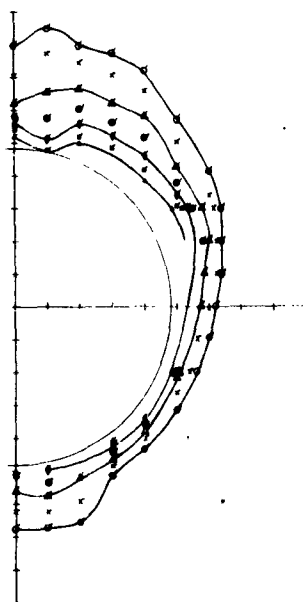
X= 8.0



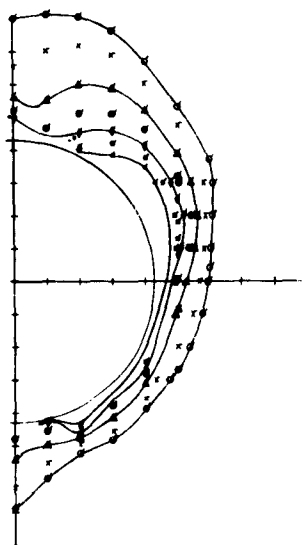
X=16.0



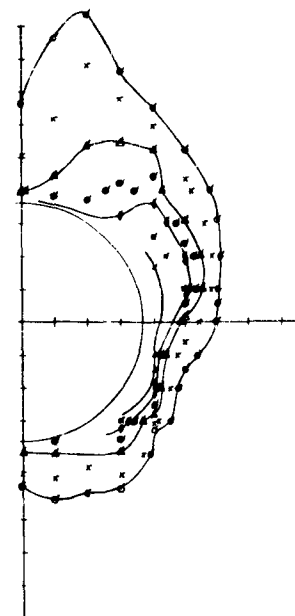
X=32.0



X=57.5



X=59.0



X=60.5

**Figure 24. Circumferential Component of Vorticity at Various Axial Positions**

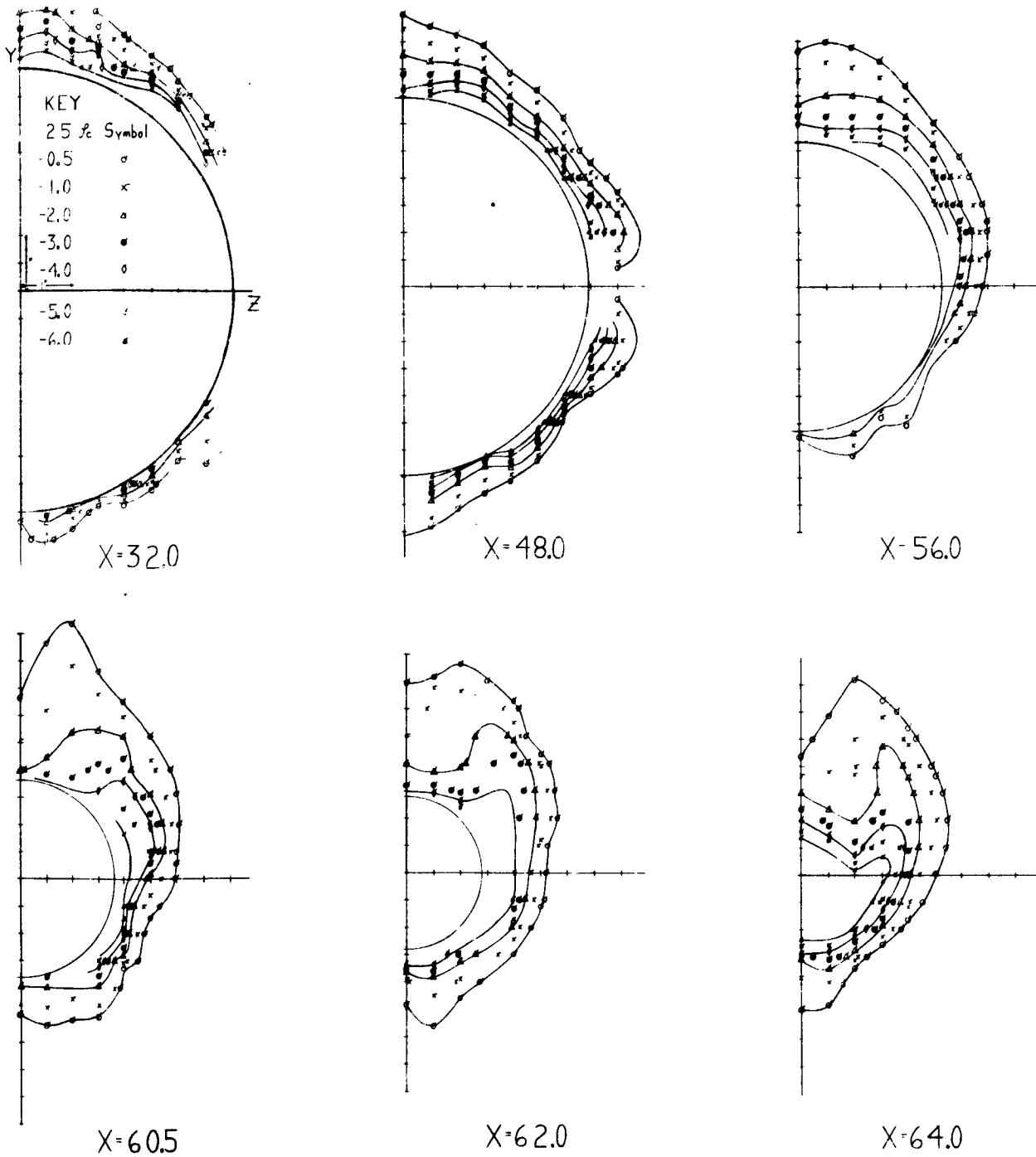
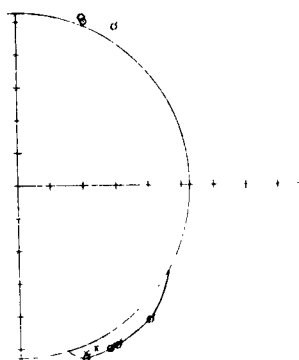
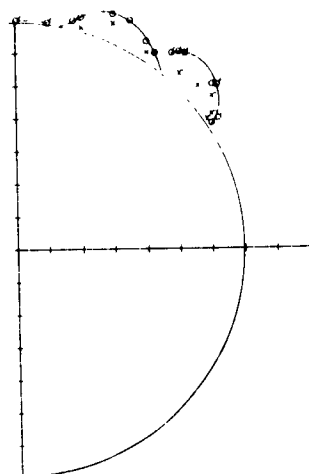


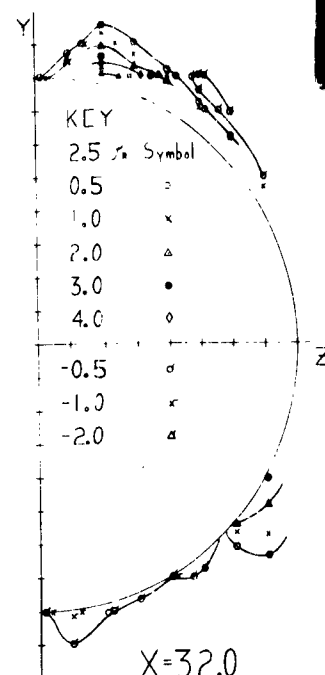
Figure 24. Circumferential Component of Vorticity at Various Axial Positions.



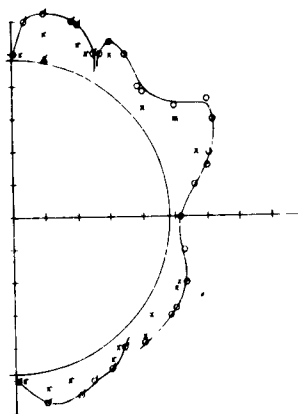
X= 8.0



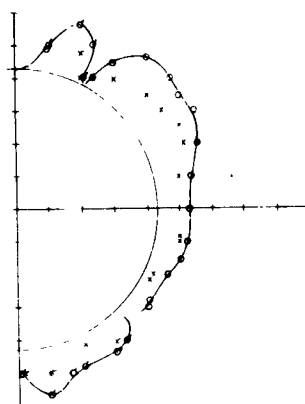
X=16.0



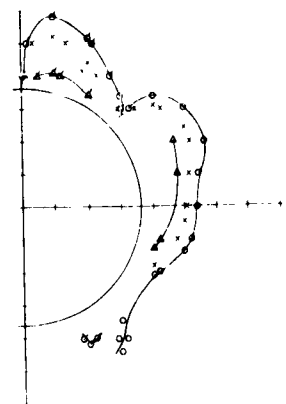
X=32.0



X= 57.5



X= 59.0



X=60.5

**Figure 25. Radial Component of Vorticity at Various Axial Positions.**

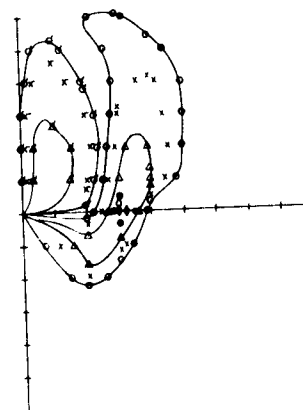
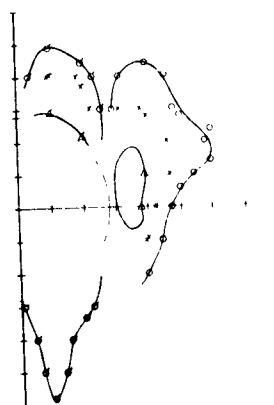
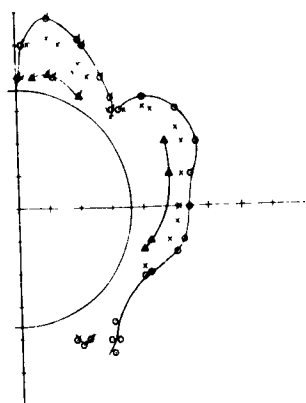
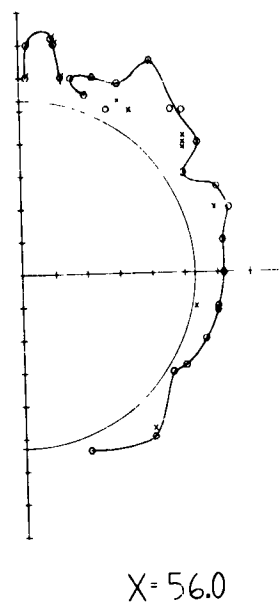
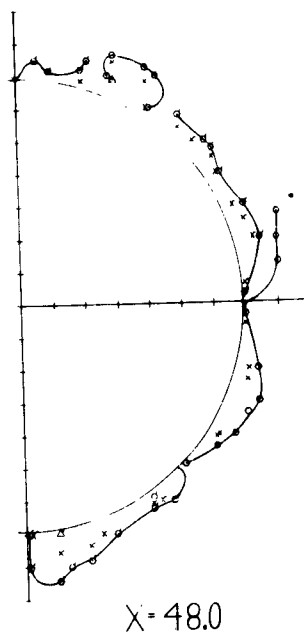
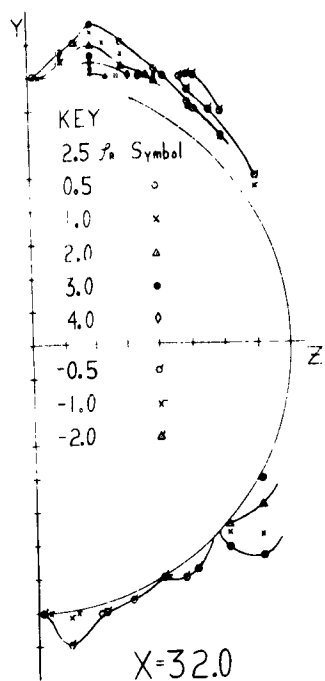
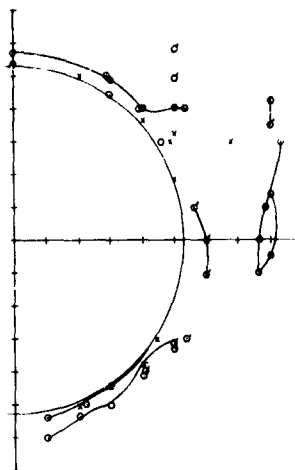
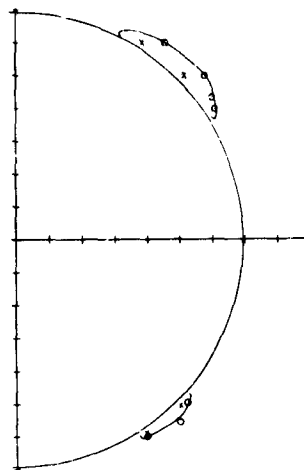


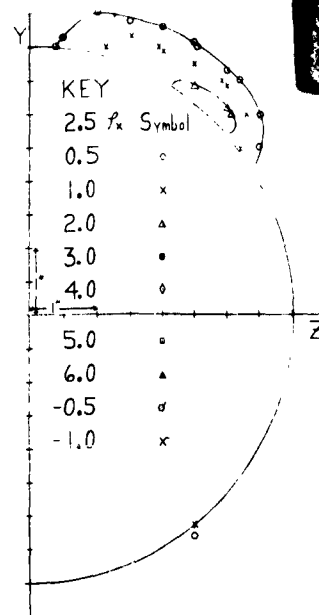
Figure 25. Radial Component of Vorticity at Various Axial Positions.



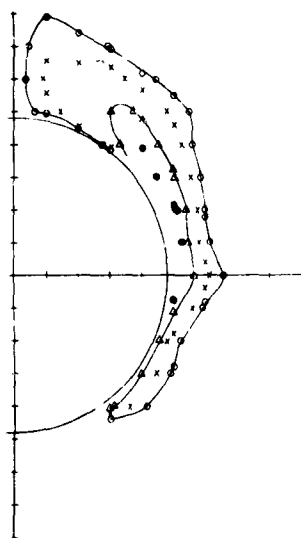
$X=8.0$



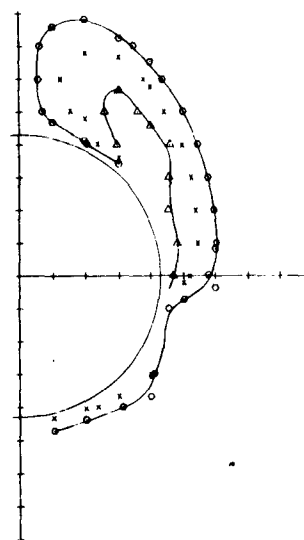
$X=16.0$



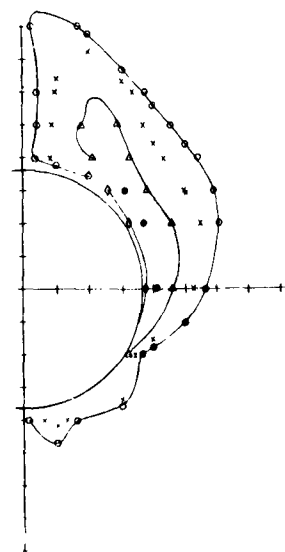
$X=32.0$



$X=57.5$



$X=59.0$



$X=60.5$

**Figure 26. Axial Component of  $V_x$  Various Axial Positions.**

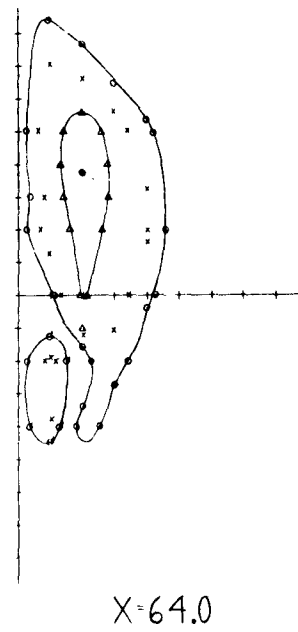
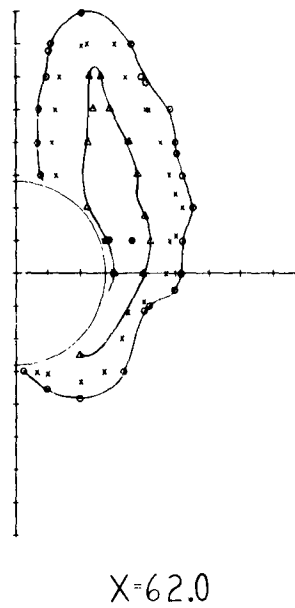
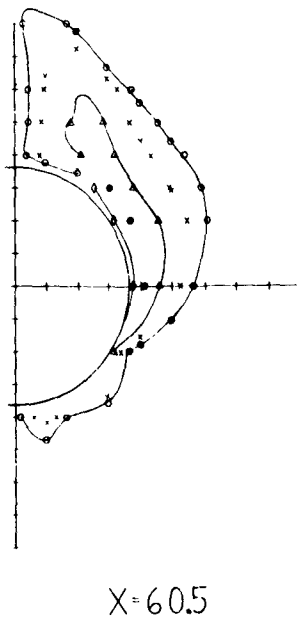
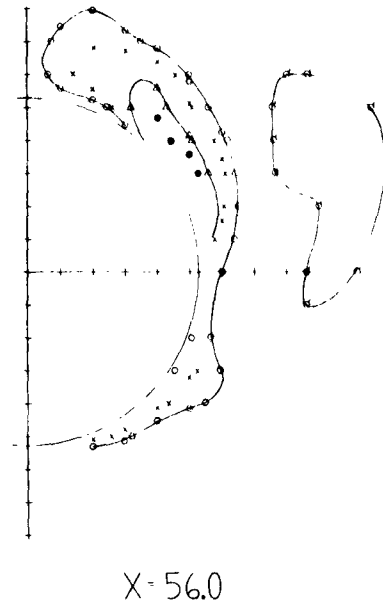
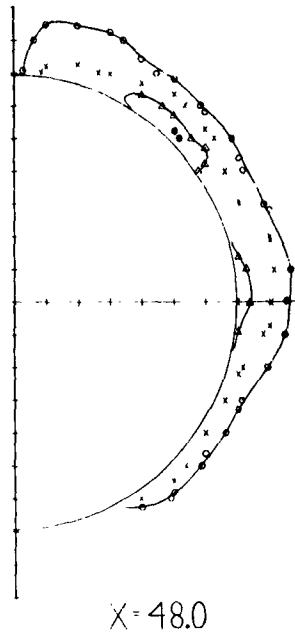
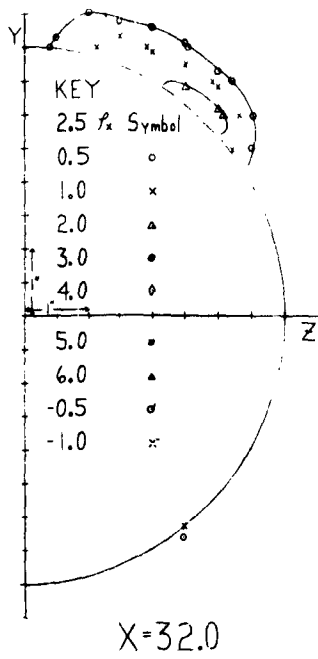
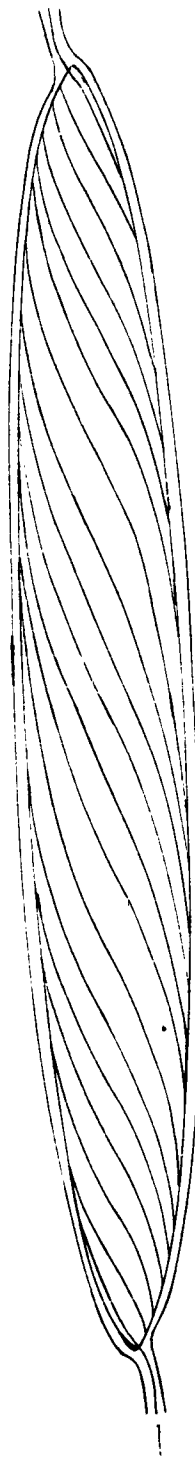


Figure 26. Axial Component of Vorticity at Various Axial Positions.





**Figure 27. Potential Flow Surface Streamlines.**



Figure 28. Actual Surface Streamlines.

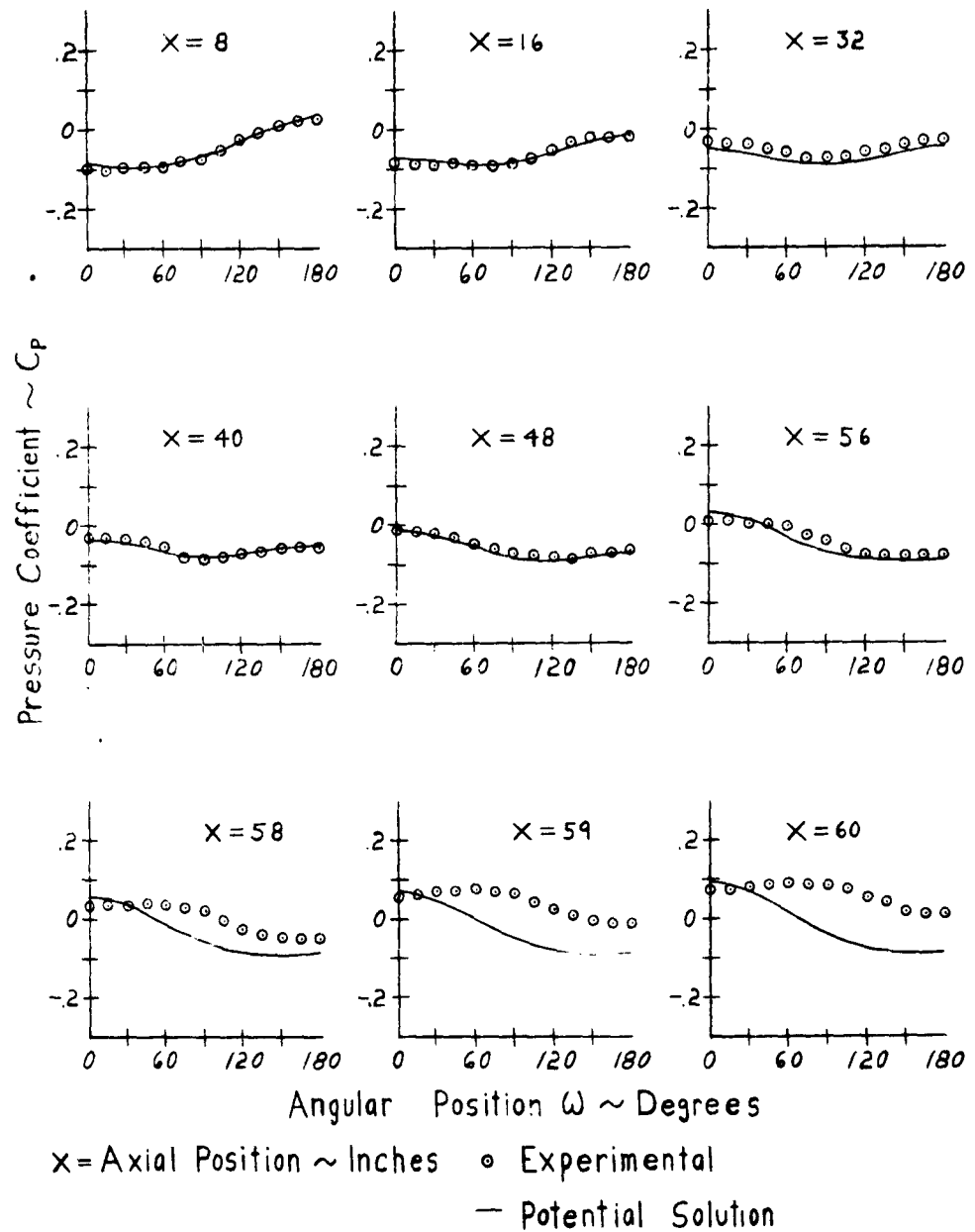


**Figure 29. Circumferential Pressure Distributions at Various Axial Positions.**

--- Theoretical Minimum Pressure  
o Experimental Minimum Pressure  
--- Experimental Separation Line

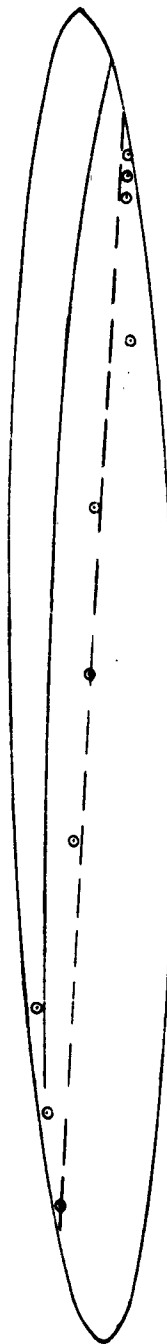
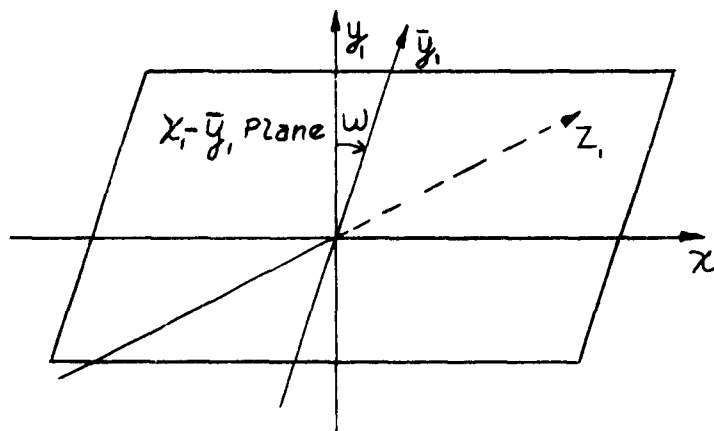
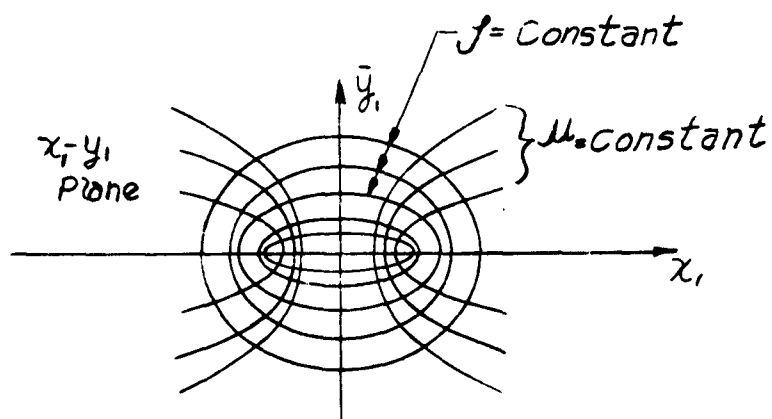


Figure 30. Minimum Pressure Line and Separation Line.



Cylindrical Coordinates



Confocal Ellipsoids and Hyperboloids

Figure 31a. Semi-Elliptic Coordinate System for Potential Flow Calculations.

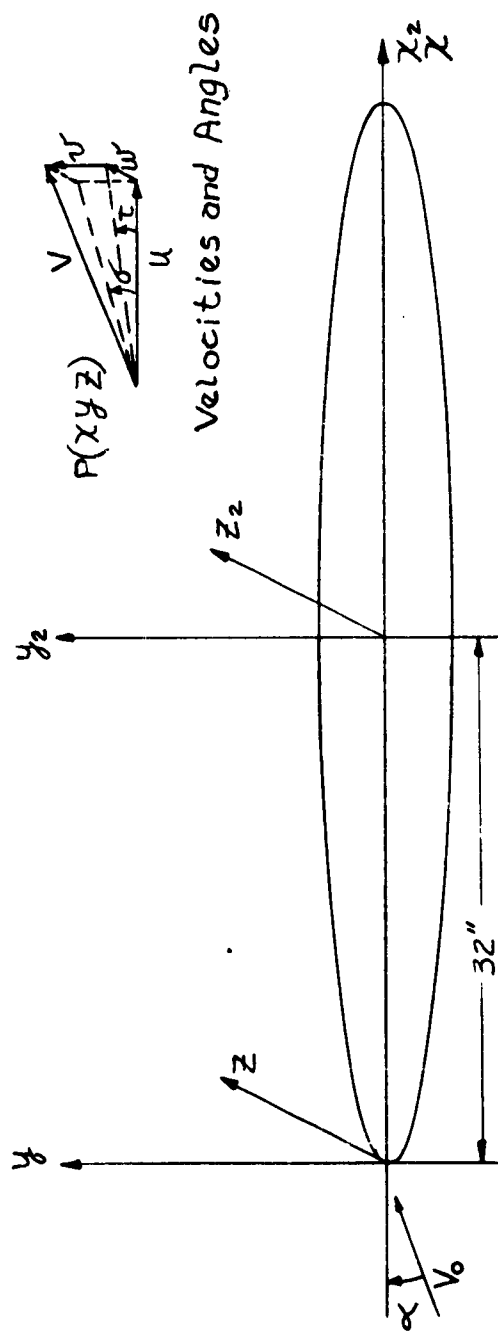


Figure 31b. Rectangular Coordinate System of Tests.

--- Faired Through Experimental Points  
 — Based on Displacement Thickness

$$\Delta C_P = \frac{(P_0)_{x=0} - (P_0)_x}{\frac{1}{2} \rho V_0^2}$$

Tunnel Wall Taps

◇ Rear

□ Bottom

○ Top

▽ Front

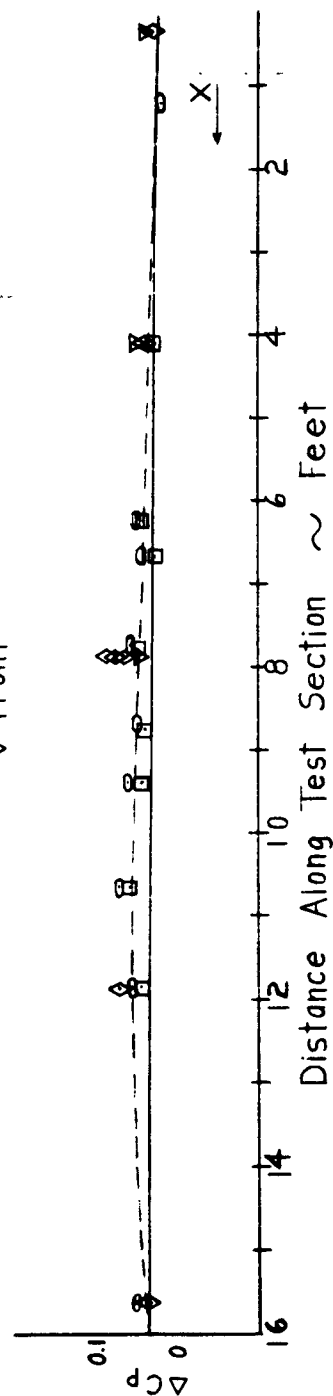
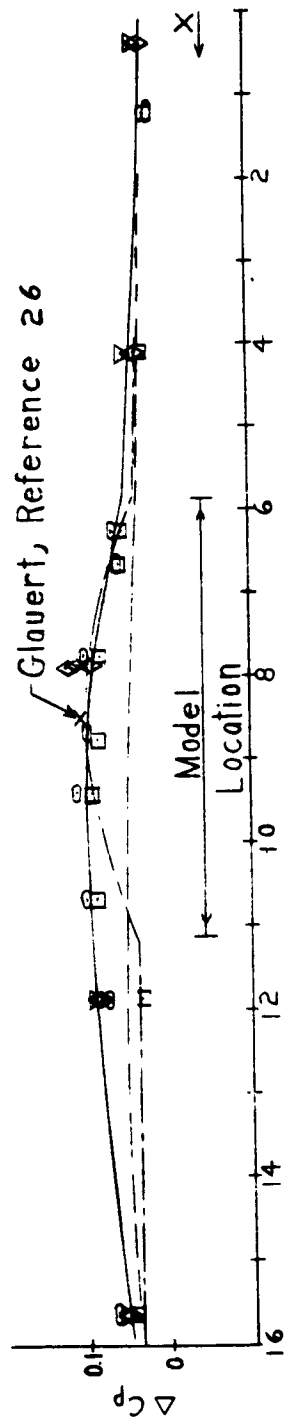


Figure 32. Tunnel Static Pressure Gradient.  
 No Model.

——— Measured: Model at 0°  
 - - - - Measured: No Model  
 - - - - Based on Displacement Thickness and Model Blockage

$$\Delta C_p = \frac{(P)_{x=0} - (P)_x}{\frac{1}{2} \rho V_\infty^2}$$

Tunnel Wall Taps  
 ◇ Rear  
 □ Bottom  
 ○ Top  
 ▽ Front



Distance Along Test Section ~ Feet

Figure 33. Tunnel Static Pressure Gradient, Model at 0 Degrees.



--- Measured: Model at 0°  
 --- Model at 6°

$$\Delta C_p = \frac{(P_0)_{x=0} - (P_0)_x}{\frac{1}{2} \rho V_0^2}$$

Tunnel Wall Taps

◇ Rear

□ Bottom

○ Top

▽ Front

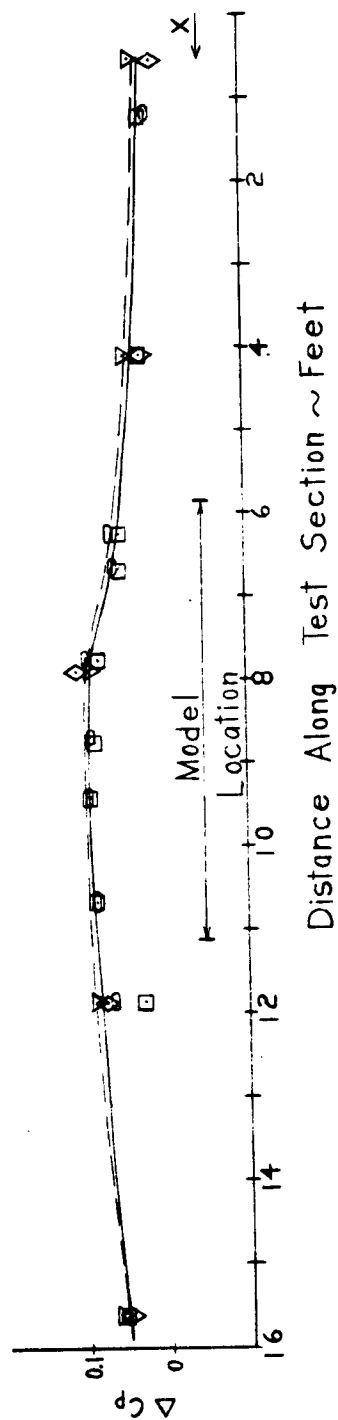


Figure 34. Tunnel Static Pressure Gradient  
 Model at 6 Degrees.

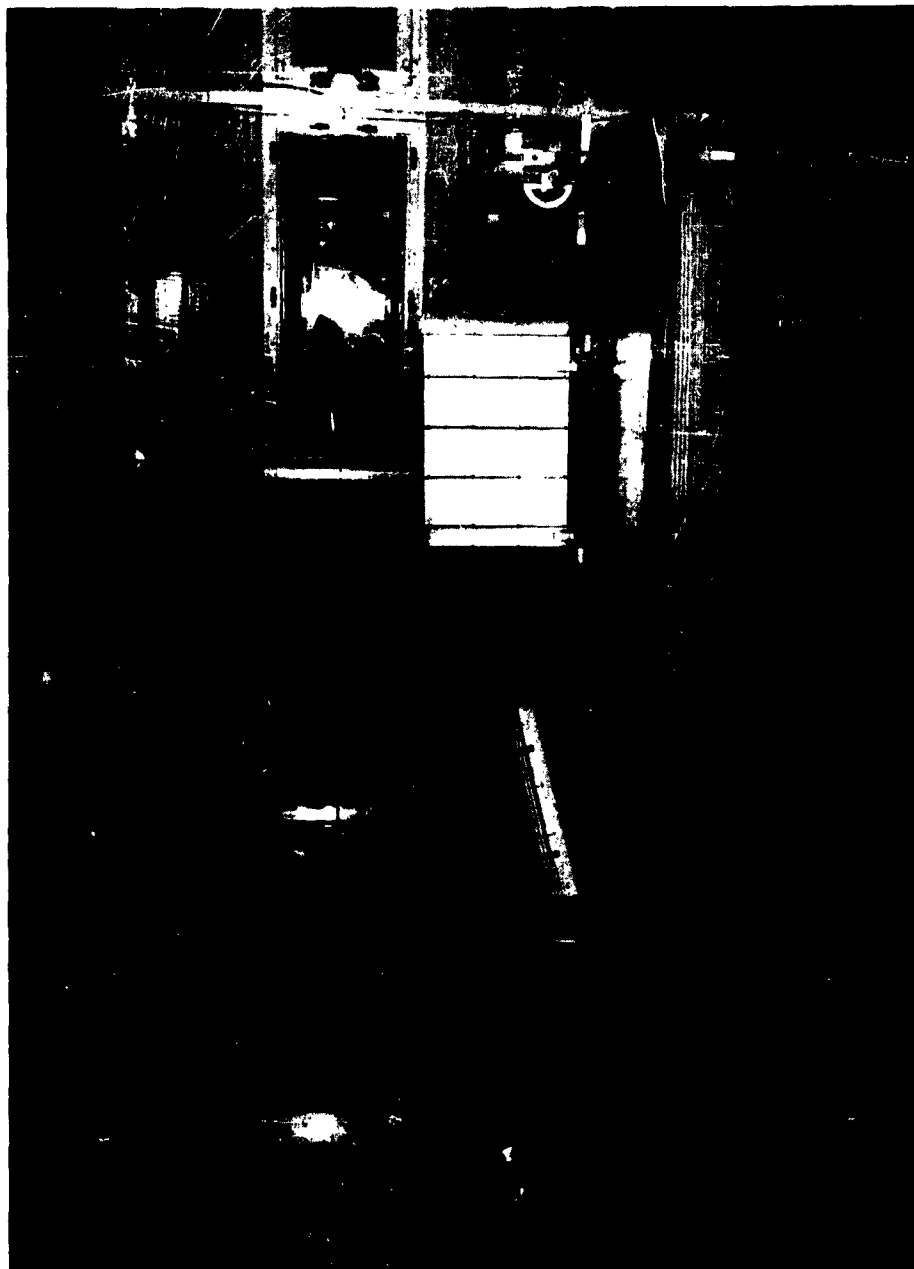


Figure 35. Tuft Calibration Set up.

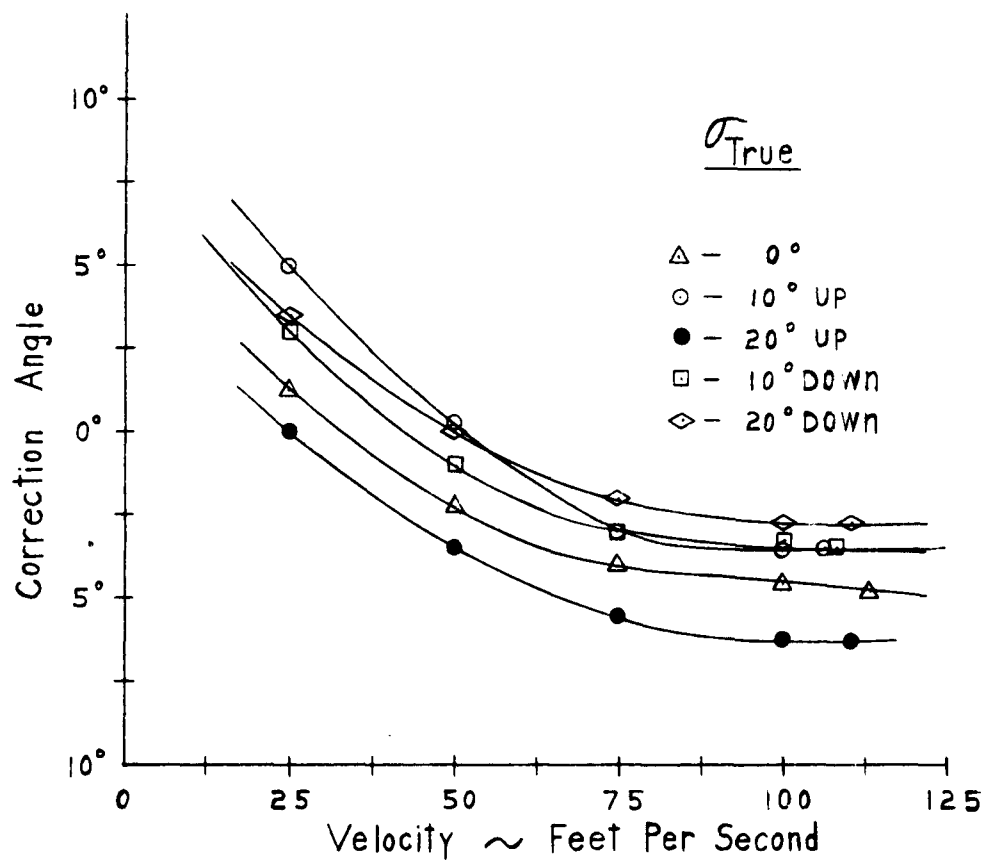
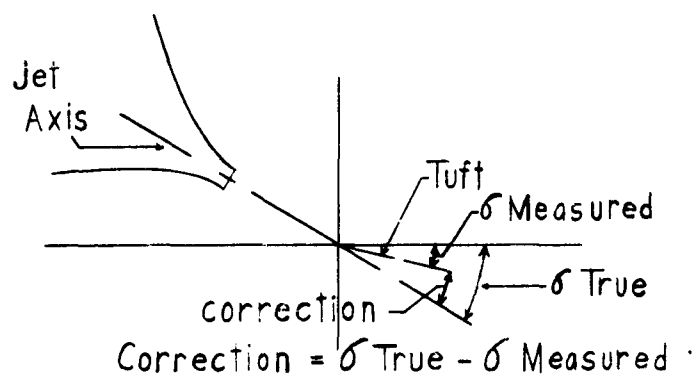


Figure 36. Tuft Calibration Curves.

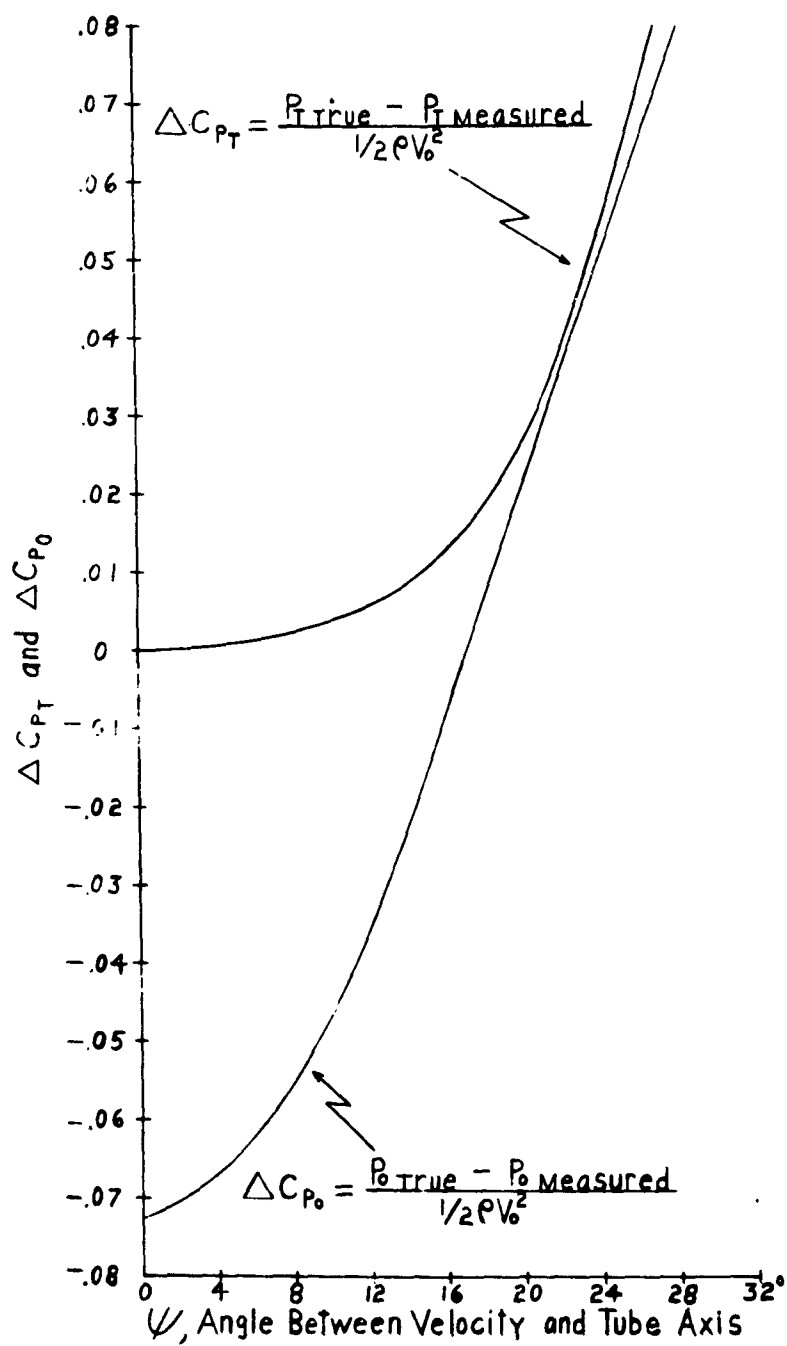


Figure 37. Rake Calibration Curves.